

AD _____

Award Number: DAMD17-98-1-8231

TITLE: A Computational Approach Toward Identification of
Malignant Lesions of the Human Breast: The Dynamics of
Magnetic Resonance Imaging Contrast Agent Uptake

PRINCIPAL INVESTIGATOR: Jonathan H. Kaufman, Ph.D.
John S. Leigh, Ph.D.

CONTRACTING ORGANIZATION: University of Pennsylvania
Philadelphia, Pennsylvania 19104-3246

REPORT DATE: September 2000

TYPE OF REPORT: Annual Summary

PREPARED FOR: U.S. Army Medical Research and Materiel Command
Fort Detrick, Maryland 21702-5012

DISTRIBUTION STATEMENT: Approved for Public Release;
Distribution Unlimited

The views, opinions and/or findings contained in this report are those of the author(s) and should not be construed as an official Department of the Army position, policy or decision unless so designated by other documentation.

20010620 114

REPORT DOCUMENTATION PAGE

Form Approved
OMB No. 074-0188

Public reporting burden for this collection of information is estimated to average 1 hour per response, including the time for reviewing instructions, searching existing data sources, gathering and maintaining the data needed, and completing and reviewing this collection of information. Send comments regarding this burden estimate or any other aspect of this collection of information, including suggestions for reducing this burden to Washington Headquarters Services, Directorate for Information Operations and Reports, 1215 Jefferson Davis Highway, Suite 1204, Arlington, VA 22202-4302, and to the Office of Management and Budget, Paperwork Reduction Project (0704-0188), Washington, DC 20503

1. AGENCY USE ONLY (Leave blank)

2. REPORT DATE

September 2000

3. REPORT TYPE AND DATES COVERED

Annual Summary (1 Sep 99 - 31 Aug 00)

4. TITLE AND SUBTITLE

A Computational Approach Toward Identification of
Malignant Lesions of the Human Breast: The Dynamics of
Magnetic Resonance Imaging Contrast Agent Uptake

5. FUNDING NUMBERS

DAMD17-98-1-8231

6. AUTHOR(S)

Jonathan H. Kaufman, Ph.D.

John S. Leigh, Ph.D.

7. PERFORMING ORGANIZATION NAME(S) AND ADDRESS(ES)

University of Pennsylvania
Philadelphia, Pennsylvania 19104-3246

E-Mail: jonathak@mail.med.upenn.edu

8. PERFORMING ORGANIZATION
REPORT NUMBER

9. SPONSORING / MONITORING AGENCY NAME(S) AND ADDRESS(ES)

U.S. Army Medical Research and Materiel Command
Fort Detrick, Maryland 21702-5012

10. SPONSORING / MONITORING
AGENCY REPORT NUMBER

11. SUPPLEMENTARY NOTES

This report contains colored photos

12a. DISTRIBUTION / AVAILABILITY STATEMENT

Approved for Public Release; Distribution Unlimited

12b. DISTRIBUTION CODE

13. ABSTRACT (Maximum 200 Words)

Breast tumors have a higher sodium content than normal tissue. Thus, sodium magnetic resonance imaging (MRI) could prove to be a valuable non-invasive diagnostic for Breast Cancer. MRI is commonly used in clinical settings to image the interior of the human body. Currently, all clinical MRI protocols are sensitive to water or fat. Adjustments to MRI equipment can enable the technology to be sensitive to sodium. This research presents the results of technical developments within MRI to non-invasively image sodium content in a human breast. This imaging technology, in combination with existing MRI techniques, could lead to a new method for screening and staging the progression of breast cancer.

14. SUBJECT TERMS

Breast Cancer

15. NUMBER OF PAGES

168

16. PRICE CODE

17. SECURITY CLASSIFICATION
OF REPORT

Unclassified

18. SECURITY CLASSIFICATION
OF THIS PAGE

Unclassified

19. SECURITY CLASSIFICATION
OF ABSTRACT

Unclassified

20. LIMITATION OF ABSTRACT

Unlimited

NSN 7540-01-280-5500

Standard Form 298 (Rev. 2-89)
Prescribed by ANSI Std. Z39-18
298-102

Table of Contents

| | |
|-----------------------------------|----|
| Cover..... | 1 |
| SF 298..... | 2 |
| Table of Contents..... | 3 |
| Introduction..... | 4 |
| Body..... | 4 |
| Key Research Accomplishments..... | 10 |
| Reportable Outcomes..... | 11 |
| Appendices..... | 12 |

Introduction

As indicated in the previous annual progress report, limited success was found employing the fuzzy clustering algorithm on the first 43 subjects studied. Clustering temporal pixel image intensity curves based on a series of four to six time points post gadolinium injection presented a limited set of functional variants. A more direct physiological approach toward understanding sodium content in breast lesions, which is one physiological parameter that regulates temporal gadolinium uptake. Special coils and pulse sequences were developed to perform sodium breast imaging on a clinical MRI scanner. The resulting sodium breast images, included in this document were presented at the recent Era of Hope meeting. The factors that influence sodium content in a benign or malignant lesion derive from several sources. Palpable lesions likely derive stiffness (relative to surrounding tissue) through osmotic pressure buildup in the local extracellular matrix. The most studied tissue where sodium concentration is measured in this regard is articular cartilage. Thus, cartilage has been employed as a convenient model tissue for quantifying the osmotic mechanisms associated with elevated sodium content.

Background

Studies have indicated an interstitial fluid pressure of 29 mm Hg in invasive ductal carcinomas, 3.6 mm Hg in benign lesions, and -0.3 mm Hg in normal breast tissue (P. B. Roemer et. al., MRM 16:192,1990). An increase in biological fluid pressure is often osmotically related to an increase in tissue sodium content. To non-invasively explore the notion that high sodium content is present in malignant breast lesions, technology for improving the sensitivity and resolution of sodium breast MR images must be developed. We have developed a transmit coil/ phased array system for sodium to be used at 4 Tesla. By double tuning the transmit coil and building special phased arrays with both proton and sodium coils, we perform breast imaging at both proton and sodium frequencies within the same examination.

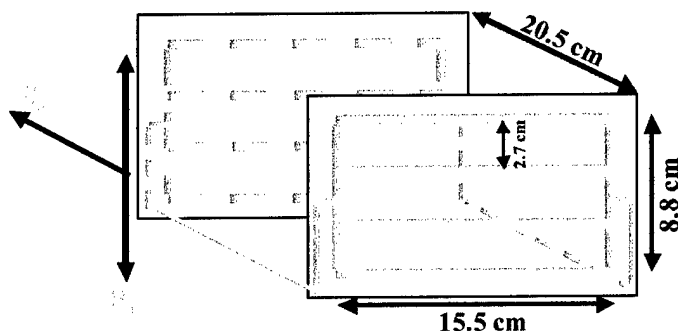
Magnetic resonance imaging of breast lesions has been unable to identify malignant vs. benign lesions using only T1-weighted and T2-weighted imaging sequences. Presently, gadolinium-based contrast agents are being explored as an approach toward distinguishing lesion types. The increased accumulation of contrast agent in malignant tumors is thought to arise from the increased permeability of the blood vessels within the tumor. This increased permeability combined with the lack of a lymphatic system may also contribute to an increase in interstitial fluid pressure and an increase in tissue sodium content.

Coil Design

The transmit coil was made with 0.6 cm wide copper tape in a biplanar design. The geometry is shown in the figure. This coil makes linear B1. The breast falls into the coil from the top and the receiver coils are used to lightly compress the breast from the sides. The capacitance for the transmit coil is distributed to six sites. The coil is driven capacitively. In order to detune the transmit coil during receive conditions, a diode is placed in series with the drive of the coil. This diode is biased on during transmit

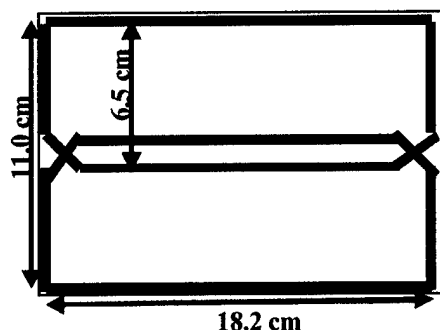
conditions with a 5V dc signal which is delivered by the spectrometer with the rf pulse. It is back biased with -15V dc during all other times.

Transmit Coil Geometry



Two plates each with two receive coils were used to lightly compress the breast during the examination in the four coil array set up. The dimensions are shown in the receiver coil geometry figure. The coils are etched on single side copper clad epoxy circuit board. The capacitance was distributed at 6 locations. A detuning circuit as described by Roemer, et al, was used for decoupling the receiver coils from the transmitter coil during the excitation pulse.

Receiver Coil Geometry



Results and Discussion

Figures 1 and 2 show an axial proton and sodium image of a normal breast. Even though there are no abnormalities in this breast, variation in the sodium signal can be seen. For instance, the regions of lipid signal do not show much sodium signal while the breast parenchyma does. In the sagittal image (figure 3), a gap in the sodium signal representative of the bones in the chest can be seen. In addition, variations in the level of

the sodium signal is evident which is indicative of the variations in the parenchymal thickness.

In normal breast tissue, sodium signal can be seen in parenchymal tissue with variations most likely indicative of parenchymal density. Skin also produces a signal as seen on the axial images. The sodium images need to be acquired at fairly high spatial resolution (1-2mm) to maintain correspondence with the proton images, which have an in-plane resolution of 0.4mm. This correspondence will permit the comparison of sodium content with contrast agent uptake.



Figure 1. Axial proton image of human breast. The proton image is a rf-spoiled gradient echo with a FOV of 24 cm (only part of the FOV shown here), TE/TR = 2.5/100 and 7 mm slice thickness.

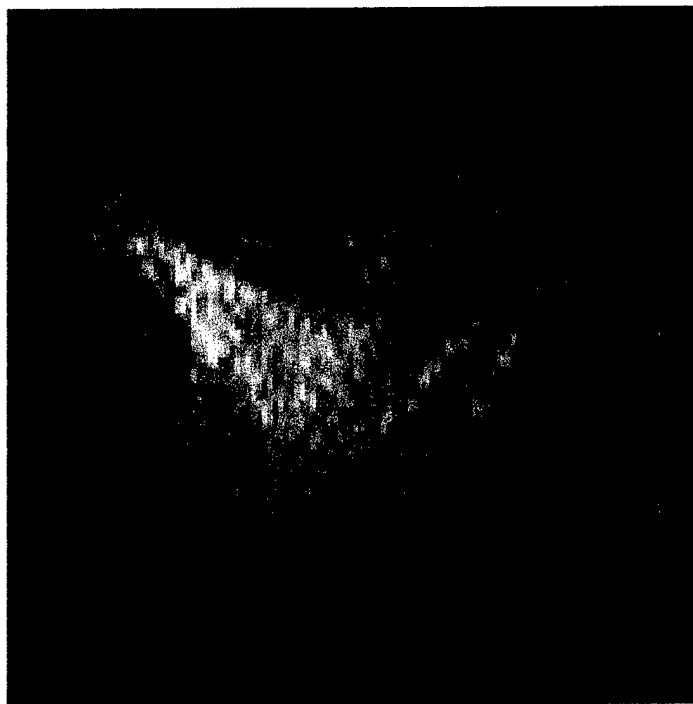


Figure 2. Axial sodium image of human breast. The sodium image was acquired fast, rf-spoiled gradient echo sequence was used with a flip of 90 degrees, $TE/TR = 2.5/150$ ms, 15.6 kHz receiver bandwidth, acquisition matrix of 256×128 , sixteen summations and a FOV of 30 cm and slice thickness of 30 mm.

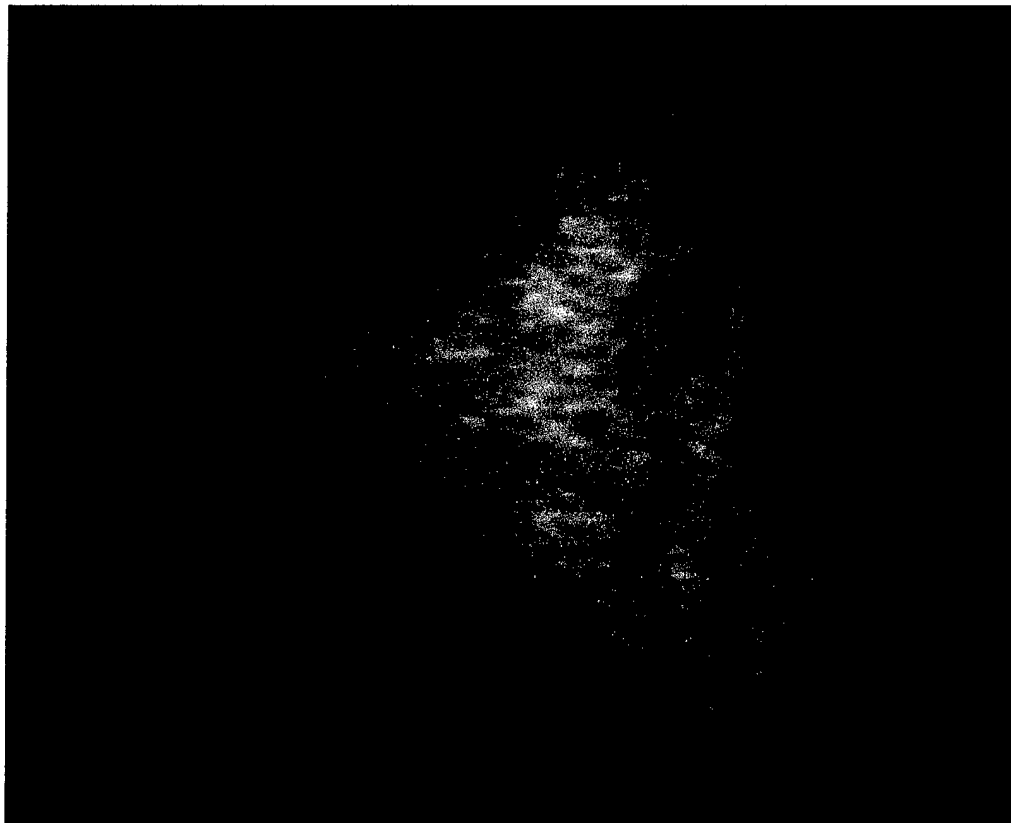


Figure 3. Sagittal sodium image of human breast. This was acquired with a bandwidth of 7.81 kHz and 8 summations resulting in an acquisition time of 2 min. 35 sec. A fast, rf-spoiled gradient echo sequence was used with a flip of 90 degrees, TE/TR = 3.3/150 ms, acquisition matrix of 256x128, a FOV of 30 cm and slice thickness of 30 mm.

KEY RESEARCH ACCOMPLISHMENTS

- Realized sodium MRI of the human breast.
- Modeled the contribution of sodium equilibria to the physical properties of connective tissue.

REPORTABLE OUTCOMES

The study of sodium imaging of the human breast was presented at the Era of Hope Meeting. A study of sodium equilibria in connective tissue was published as a dissertation.

- Sodium MRI of the human breast, Kaufman JH, Bolinger L, Leigh JS, University of Pennsylvania Medical Center, presented at US Army Era of Hope Meeting, Atlanta GA, 2000.
- Kaufman JH, Ph.D. Dissertation, Biochemistry and Molecular Biophysics, University of Pennsylvania School of Medicine. December 2000.

SODIUM MRI OF THE HUMAN BREAST

Kaufman JH, Bolinger L, Leigh JS

University of Pennsylvania Medical Center

jonathak@mail.med.upenn.edu

Breast tumors have a higher sodium content than normal tissue. Thus, sodium MRI could prove to be a valuable non-invasive diagnostic for discriminating malignant lesions. We have developed a technique for generating sodium images of the breast in a clinical setting.

A sodium transmitter with multicoil receive was built of a similar design to the one used for proton breast examinations at 4 Tesla. The transmitter is a biplanar design, which is easily double-tuned to both proton and sodium. Two plates each with two receive coils were used to lightly compress the breast during the examination.

Figure 1 shows an axial proton and sodium image of a normal breast. Even though there are no abnormalities in this breast, variation in the sodium signal can be seen. For instance, the regions of lipid signal do not show much sodium signal while the breast parenchyma does. In the sagittal image (figure 2), a gap in the sodium signal representative of the bones in the chest can be seen. In addition, variations in the level of the sodium signal is evident, which is indicative of the variations in the parenchymal thickness.

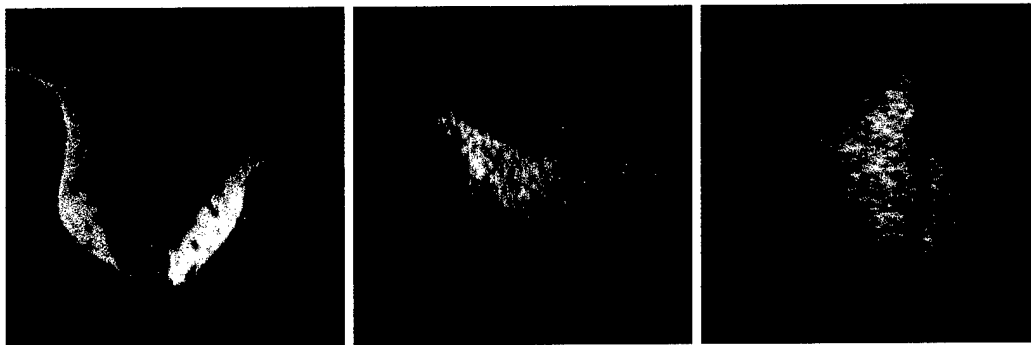


Figure 1(a)

Figure 1(b)

Figure 2

The U.S. Army Medical Research and Materiel Command under DAMD17-98-1-8231 supported this work.

**MAGNETIC RESONANCE STUDIES OF CARTILAGE OSMOTIC AND MECHANICAL
PROPERTIES**

JONATHAN H. KAUFMAN

A DISSERTATION
IN
BIOCHEMISTRY AND MOLECULAR BIOPHYSICS

PRESENTED TO THE FACULTIES OF THE UNIVERSITY OF PENNSYLVANIA IN PARTIAL
FULFILLMENT OF THE REQUIREMENTS FOR THE DEGREE OF DOCTOR OF PHILOSOPHY

2000

Supervisor of Dissertation

Graduate Group Chairperson

ABSTRACT
**MAGNETIC RESONANCE STUDIES OF CARTILAGE OSMOTIC AND MECHANICAL
PROPERTIES**

JONATHAN H. KAUFMAN

JOHN S. LEIGH

Articular cartilage, the tissue that coats the ends of bones in synovial joints, is remarkable in that it is solid while being primarily composed of water. The progressive deterioration of articular cartilage debilitates over 20% of the human population. Most major pharmaceutical companies actively pursue cartilage regenerative therapies; however, it is difficult to test the effectiveness of novel treatments since cartilage condition cannot be monitored non-invasively. Here, we present several new ways to assess cartilage softening via magnetic resonance imaging (MRI). Cartilage softening is one of the earliest manifestations of cartilage degeneration. First, a new quantitative osmotic model of cartilage rheology is developed. Then, the equilibrium of a charged MR contrast agent is used to confirm the osmotic properties that are hypothesized to give cartilage its strong compressive resistance. A novel method for mechanically compressing cartilage specimens in an imaging environment is then demonstrated. Conventional MRI parameters of articular cartilage are presented as a function of compression. One major advantage that this new technique has over purely mechanical studies is that, during compression, positional cartilage water content can be dynamically mapped. Additional techniques are presented: one for dynamically measuring cartilage fluid permeability, and a second for spatially mapping cartilage rheological properties. The osmotic model is then further confirmed by interleaved sodium and proton imaging during compression.

CONTENTS

| | |
|--|-----|
| Chapter 1 A review of articular cartilage structure, function, and imaging | 1 |
| Chapter 2 A magnetic resonance imaging based demonstration of articular cartilage ionic equilibria | 10 |
| Chapter 3 A method for compressing articular cartilage within a magnetic resonance imaging environment | 29 |
| Chapter 4 Spectroscopic magnetic resonance imaging parameters of articular cartilage during compression | 38 |
| Chapter 5 The cartilage uni-axial confined compression experiment within a magnetic resonance imaging environment | 62 |
| Chapter 6 Articular cartilage fluid permeability during compression | 72 |
| Chapter 7 Multinuclear study of the cartilage osmotic model | 79 |
| Appendix A Magnetic resonance imaging of unconfined cartilage compression | 97 |
| Appendix B Magnetic resonance imaging cartilage strain mapping during compression | 108 |
| Bibliography | 139 |

LIST OF TABLES

| | |
|--|----|
| Table 2.1 T_1 measurements of the five cartilage specimens equilibrated in 137 mM PBS without Gd(DTPA). | 22 |
| Table 2.2 T_1 measurements of the five cartilage specimens equilibrated in PBS solutions of various NaCl concentrations with 1.0 mM Gd(DTPA). | 25 |
| Table 4.1 Proton relaxation parameters. Relaxation times are given for proton T_1 , and proton T_2 for cartilage in the normal and mechanically compressed state. | 51 |
| Table 4.2 The statistical significance of the change in relaxation time constants associated with compression. | 52 |
| Table 4.3 Proton MR mean relaxation time constants of normal and proteoglycan depleted cartilage specimens. | 61 |
| Table 5.1 The deformation creep data of figure 6.3 were fit to the biexponential decay function given in equation 6.2. | 70 |
| Table 7.1 Sodium and proton relaxation parameters. | 91 |
| Table 7.2 The statistical significance of the change in relaxation time constants associated with compression. | 92 |

CHAPTER 1

ARTICULAR CARTILAGE STRUCTURE, MECHANICS AND IMAGING

1.1 Overview

This thesis describes several magnetic resonance imaging (MRI) experiments performed on articular cartilage. Each experiment was designed to elucidate articular cartilage rheological mechanisms, especially with regard to changes associated with osteoarthritis. The intention of this work is to propose and test a new theoretical model for cartilage deformation. The primary need for a new model stems from the inadequacy of existing cartilage deformation models, which are either inaccurate or overly complex.

This section begins with a brief description of articular cartilage anatomy and biochemistry in health and disease, specifically with regard to osteoarthritis. Next, a working hypothesis for articular cartilage deformation is presented along with a strategy to explore the theoretical implication of the hypothesis as well as steps toward experimentally testing the consequential model. The new model is presented in light of the most commonly accepted existing model for cartilage deformation. An overview of the thesis progression is then provided.

1.2 Articular Cartilage

The primary function of articular cartilage is to provide a low friction surface between bones in synovial joints. Articular cartilage is composed of water, a network of

collagen fibrils, and proteoglycan aggregates. Compared to most tissues, cartilage is relatively acellular (McCutchin et al. 1972).

Approximately, 80% of cartilage (by weight) is water; the remainder constitutes the solid matrix. The solid matrix is primarily composed of two biopolymers (type-II collagen fibrils, and proteoglycan aggregates) which serve distinct functions. Having a high tensile strength, the collagen fibrils maintain cartilage integrity. The proteoglycan aggregates impart a substantial negative fixed charge density within the cartilage matrix which causes a large osmotic pressure. The counteracting forces of the high osmotic pressure and the collagen fibril tensile strength give cartilage its solid character (Mankin et al. 1994). This concept is discussed in more detail and quantified in chapter 2.

The high water pressure within cartilage presents a resistance to mechanical compression and permits articular cartilage to serve as a mechanical shock absorber when synovial joints undergo brief periods of impact. During cartilage compression, cartilage fluid is released which contributes to synovial joint friction reduction.

Articular cartilage is the form of cartilage that resides at the articulating surfaces of bones in synovial joints. Several other types of cartilage exist. For example one form of cartilage that also exists in certain synovial joints is the cartilage that form the meniscus in the human knee joint. Another form of cartilage involved in joint mobility is the cartilage that forms the discs in a vertebral column. A more structurally distinct type of cartilage that exists outside of synovial joints is structural cartilage. This type of cartilage is a major component of certain solid structures in the human body such as the trachea, nose and external ear.

One unique aspect of articular cartilage is its layered anatomy. Articular cartilage is often described in the histological literature as having three relatively distinct layers. The layer at the articulating surface is usually designated the superficial zone. In this zone, the collagen fibers typically run parallel to the articular surface. The layer adjacent to the subchondral bone is usually designated the radial zone. In this zone, collagen fibers are typically oriented perpendicular to the cartilage-bone interface. The radial zone is usually highly calcified. The region of articular cartilage between the superficial zone and the radial zone is usually referred to as the intermediate zone. In this zone, collagen fibers do not have a distinct orientation. Scanning electron microscopy studies of articular cartilage yield an overall sheet-like structure. In these studies, cartilage structure is in the form of parallel sheets that are oriented parallel to the articular surface in the superficial zone, and aggregately bend in a direction perpendicular to the surface. (Mow et. al. 1990).

The notion of a layered cartilage structure, and the notion that cartilage structure is locally non-isotropic, is important to experiments and discussions described in the present work. Specifically, the present work employs the assumption that cartilage has local lateral (parallel to the articular surface) mechanical homogeneity, but has mechanical non-homogeneity in a direction perpendicular to the articular surface.

1.2 Osteoarthritis

Osteoarthritis is a condition present in most (if not all) species that contain synovial joints (Lawrence et al. 1989). The disease is characterized by a progressive deterioration of articular cartilage. There is evidence that the early onset of osteoarthritis is characterized by the selective loss of the proteoglycan component of the solid matrix. There is

currently no pharmacological treatment for reversing the progression of osteoarthritis (Ghosh et al. 1991). Existing therapies include: pain management (Davis et al. 1993, Todd et al. 1990), joint strengthening exercises (Jan et al. 1993, Kovar et al. 1992), dietary supplements, prosthetic joint replacement (Amendola et al. 1989), and chondrocyte transplantation. One major impediment to pharmaceutical development for therapies that reverse the osteoarthritic process is that the progression or regression of osteoarthritis is currently not measurable non-invasively (March et al. 1996). It is therefore difficult to measure the efficacy of novel therapeutics.

The disease process of osteoarthritis involves the degeneration of articular cartilage. The earliest putative changes in cartilage due to osteoarthritis are softening of cartilage, a decrease in proteoglycan content, and an increase in permeability (Armstrong et al. 1982; Lesperance et al. 1992; Mansour et al. 1976). Each of these changes has been associated with an alteration in the mechanical properties of cartilage (Mow et al. 1984; Bassar et al. 1988; Mow et al. 1980). Therefore, there has been substantial interest in studying the mechanical properties of normal and degenerated articular cartilage.

The impact and motivation of the efforts described in this thesis stem from the substantial prevalence of osteoarthritis. Approximately 40 million people (in the U.S. alone) are affected by osteoarthritis, with a major characteristic being a change in the mechanical properties of articular cartilage. Since there is currently no method for diagnosing osteoarthritis in its early stage, as well as no current method for sensitively measuring the ongoing progression of osteoarthritis in any given individual, a new diagnostic

method is needed. An effective approach may likely include consideration of cartilage mechanical properties.

1.3 Cartilage Mechanical Properties

Early attempts to study the mechanical properties of articular cartilage involved indentation experiments. In these experiments, the dynamics of cartilage response to an indenter was used to evaluate cartilage compressive modulus and cartilage viscosity (Harris et al 1972). The quantitative results of such experiments were difficult to interpret since cartilage is non-isotropic and indentation experiments are inherently multidimensional. The results of these experiments varied when different shaped indenters were used. Also, the shape of an indentation at any given time was difficult to characterize. One would intuitively expect that observing the response of cartilage to indentation would yield information on its mechanical properties. However, in practice, indentation experiments have been unable to yield substantial quantitative information on cartilage mechanics. The primary reason for this lack of effectiveness is the complexity involved with developing a theory to adequately describe cartilage response to indentation, especially given the fact that cartilage response to indentation depends on the shape of the indenter.

This challenge was met by the design of the uniaxial confined compression experiment (Mow et al. 1980). Even though indentation experiments have maintained utility for testing certain cartilage deformation hypotheses (Mow et al. 1989; Jurvelin et al. 1990; Oloyede et al. 1991; Hale et al. 1993; Athanasiou et al. 1994; Obeid et al. 1994; and Haut et al. 1995), the advent of the uniaxial compression experiment yielded experi-

mental results that could be directly related to a theoretical description of cartilage uniaxial compression. It should be noted that the uniaxial compression experiment, of course, did not solve all challenges. For example, it has also been shown that the dynamics of cartilage compression are dependant upon load cycling (Suh et al. 1995; Su et al. 1996). Moreover, the theoretical cartilage mechanical model for the uniaxial compression experiment (as well as other experiments) was still fairly complex.

In addition to compression studies, several other types of mechanical studies have been used to evaluate cartilage mechanical properties. Three common methods are steady state permeation, stress relaxation, and torsional shear (Zahler 1999). In the steady state permeation experiment, the ability of fluid to flow through cartilage is measured for a cartilage specimen in a fixed position (Mansour et al. 1976; Torzilli et al. 1983; Mak 1986; and Gu et al. 1993). The stress relaxation experiment involves a fast cartilage compression (in the form of a step function). The stress that the cartilage specimen imparts on the compressive apparatus is then measured as a function of time (Mow et al. 1980). The shear experiment involves fixing a mechanical platen or indenter to the cartilage surface and measuring the statics and dynamics of cartilage by imparting a torque or lateral force (Parsons and Black 1977; Spirt et al. 1989; and Zhu et al. 1993).

The present work focuses on developing and testing a useful mechanical model of cartilage compression. The most commonly accepted existing model, developed in by V.C. Mow 1980, as applied to the uniaxial compression experiment contains a set of coupled partial differential equations which presents a challenge for many cartilage investigators when interpreting experimental results in light of contemporary theory. Mow's

theoretical model may be appropriate for describing cartilage rheological mechanisms from a continuum mechanics approach. However, from a practical standpoint, the intuition of the model can become lost in its complexity. The model proposed in this thesis is comparatively simple. In brief, cartilage is treated essentially as a dialysis bag (i.e. the mechanical properties of cartilage are derived primarily from osmotic conditions created by the cartilage biochemical composition. The fundamentals of the model, as presented in chapter 2, are relatively easy to interpret. An additional advantage of this new model is that it easily accommodates anisotropy and inhomogeneity as addressed further in appendix B.

An interesting aspect to the model is that water and sodium ion concentrations are fundamental to cartilage mechanical properties. This fact makes magnetic resonance imaging (MRI) of cartilage deformation valuable for several reasons. MRI, in general, is an active research field since MRI is currently the most promising non-invasive modality to stage osteoarthritis progression. Presented here is MRI conducted in a multinuclear fashion to noninvasively map cartilage water and sodium ion content. In this way, MRI provides an excellent means for testing the proposed theoretical model.

1.4 Imaging Cartilage Compression

As mentioned above, magnetic resonance imaging (MRI) shows promise as a non-invasive modality for imaging cartilage changes, since, in general, MRI is able to show soft tissue contrast. However, current attempts at using MRI to measure mild changes in articular cartilage have encountered inconclusive results (Hutton et al. 1995).

It is possible that an understanding of the MR characteristics of articular cartilage during compression will lead to a sensitive non-invasive indicator of disease progression.

The earliest of the cartilage compression studies within an MRI environment was conducted by Lehner et al. (1989). This experiment employed the cylinder and plunger of a common syringe to compress a glass marble against the surface of an articular cartilage specimen. In distinction to this mechanical approach, Lusse et al. (1995) combined MRI with an osmotic compression technique. In this approach, cartilage specimens were enclosed in a dialysis membrane then placed in a polyethylene glycol solution of high osmolarity. This process, in effect, dehydrated the cartilage specimens. Once dehydrated, the cartilage specimens were removed from the polyethylene glycol bath then placed in an MR spectrometer for subsequent measurement of MR parameters.

More recently, Rubenstein et al. (1996) performed mechanical compression of articular cartilage specimens within an MRI environment using a compression device design based on an earlier description at the 1995 annual meeting of the International Society of Magnetic Resonance in Medicine (Kaufman et al. 1995). Further experiments expanded upon this model (Duvvuri et al. 1998, Kaufman et al. 1999, Reddy et al. 1999), several of which constitute the basis of portions of the work presented here.

1.5 Thesis Summary

The central theme of this thesis involves novel methods for using MRI to explore the mechanical properties of articular cartilage in light of the osteoarthritic disease process. In the following chapter, MRI is used as a tool for exploring the osmotic ion balance of articular cartilage, which imparts the majority of cartilage resistance to mechanical

compression. The design and implementation of a novel MRI compatible cartilage compression device is then described. This device is then used for acquiring MR spectroscopic information on cartilage specimens during mechanical compression. An evaluation of the statistical significance of compression induced spectroscopic change is performed with respect to an in-vitro osteoarthritic model. Spatial mapping of the spectroscopic parameters is then performed during compression to investigate the spatial redistribution of MR relaxation characteristics of articular cartilage during compression. A novel method for quantifying the dynamics of cartilage compression within an imaging environment is then described and demonstrated. The results of this method are then used to infer the compression-induced dynamics of cartilage fluid permeability. The mechanical predictions of the osmotic cartilage model are formulated and confirmed by experiments. An example of multidimensional cartilage deformation is then demonstrated and described. Lastly, a technique for articular cartilage strain mapping during compression is described.

1.6 Thesis Hypothesis and Strategy

The basic working hypothesis for the present work is that ionic equilibria can accurately predict cartilage compressive strength. This present work also demonstrates a new technology: the ability to spatially map cartilage mechanical properties. The overall strategy has three components. First, a useful deformation theory of articular cartilage is developed. Next, a device is developed to compress cartilage in an MRI environment and confirm the deformation theory with experimental data. MRI is then used, in a novel way, to characterize the spatial distribution of articular cartilage mechanical properties.

$$(H' + \alpha_0 r_2) \frac{\partial^2 u}{\partial z^2} = (1 + \alpha_0)^2 \frac{\partial u}{\partial t}.$$

$$\begin{aligned} \alpha_\phi &= \alpha_\phi^0 = \text{constant} & 0 \leq z < h_s \\ \alpha_\phi &= \epsilon z + b_\phi & h_s \leq z \leq 1.0 \end{aligned}$$

$$\sigma_{zz}^s = -\alpha_\phi p + H' \frac{\partial u}{\partial z} = -f_\phi H(t), \quad z=0$$

$$\sigma_{zz}^f = -p - r_1 \frac{\partial u}{\partial z} = 0, \quad z=0.$$

Figure 1.1. V.C. Mow model for cartilage deformation in the uniaxial compression experiment. (From Mow et. al. 1980.)

CHAPTER 2

A MAGNETIC RESONANCE IMAGING BASED DEMONSTRATION OF ARTICULAR CARTILAGE IONIC EQUILIBRIA

2.1 Introduction

As mentioned in the previous chapter, ionic equilibria is an important component of articular cartilage functionality. Cartilage is a stiff tissue with strong resistance to compression while being primarily composed of water. Approximately 80% of cartilage by weight is water. The stiffness of cartilage results from the water being contained at high pressure. The high water pressure is an indirect response to the large negative fixed charge density associated with the proteoglycan component of the cartilage matrix. It has recently become popular to exploit the ionic equilibria of cartilage to non-invasively probe cartilage proteoglycan loss via charged MRI contrast agents (Bacic et al. 1997; Bashir et al. 1997; Bashir et al. 1996).

2.2 Theory of cartilage ionic equilibria

Consider a cartilage specimen equilibrated in an infinitely large NaCl bath. To simplify the algebra, all concentrations are normalized to the bathing NaCl concentration. The cartilage specimen proteoglycan content imparts an internal negative fixed charge density in the cartilage fluid volume, f_i , and consequently the cartilage fluid volume must have a sodium ion concentration of at least f_i to maintain electrostatic neutrality. An additional amount of sodium content will equilibrate into the cartilage fluid volume, since NaCl must enter the cartilage to satisfy the chloride ion chemical potential. Thus,

$$n^* = f_i + x, \quad [2.1]$$

where n^* is the sodium ion concentration within the cartilage specimen fluid compartment, f_i is the fixed charge density within the cartilage specimen fluid compartment, and x is the amount of additional NaCl that enters the cartilage fluid compartment. A general thermodynamic condition for ionic equilibria between cartilage and the bath is that the electrochemical potential of every component be equal (Helfferich 1962), i.e.

$$\frac{n^*}{n} = \frac{c}{c^*}, \quad [2.2]$$

where n^* is the cartilage fluid sodium ion concentration, n is the bath sodium ion concentration, c^* is the cartilage fluid chloride ion concentration, and c is the bathing chloride ion concentration. Given the normalization convention,

$$n = c = 1, \quad [2.3]$$

combining equations 2.1 and 2.3 yields

$$n^* c^* = 1. \quad [2.4]$$

As indicated in equation 2.1, x is the amount of NaCl that enters the cartilage from the bath given an initial condition of zero cartilage chloride ion content. Thus,

$$c^* = x. \quad [2.5]$$

Combining equations 2.1, 2.4, and 2.5 yields the quadratic relationship

$$(f_i + x)x = 1, \quad [2.6]$$

which has the solution

$$x = -\frac{f_i}{2} \pm \sqrt{1 + \left(\frac{f_i}{2}\right)^2}. \quad [2.7]$$

Combining equations 2.3, 2.5, and 2.7 yields the chloride ion equilibrium distribution, Φ , between the bath and the cartilage fluid content

$$\Phi = \frac{c^*}{c} = x = -\frac{f_i}{2} + \sqrt{1 + \frac{f_i^2}{4}}, \quad [2.8]$$

which expressed as a function of the excluded volume fraction, e , and the fixed charge density within the total cartilage volume, f , is

$$\Phi = -\frac{f}{2(1-e)} + \sqrt{1 + \left(\frac{f}{2(1-e)}\right)^2}. \quad [2.9]$$

2.3 The Gd(DTPA) method - working hypothesis

Gadolinium Diethylenetriaminepentaacetate, Gd(DTPA), has captured recent interest in cartilage research, since magnetic resonance imaging (MRI) techniques can potentially map its concentration to high spatial resolution. Gd(DTPA) equilibration provides one avenue of investigation toward using the principles of ionic equilibria to non-invasively derive the proteoglycan content of intact articular cartilage, a parameter that may be indicative of osteoarthritic progression (Hardingham et al. 1990). This approach has recently been established in an in-vitro setting (Bashir et al. 1996), and extended to in-vivo investigations (Bashir et al. 1997; Trattnig et al. 1999). To use this method one first employs standard techniques to quantify the change in the proton spin-lattice relaxation time constant, T_1 , associated with Gd(DTPA) equilibration. By using known spin-lattice relaxivities of Gd(DTPA), the Gd(DTPA) equilibrium between the cartilage interior and exterior is then quantified. Classical Donnan theory of compartmental equilibria (Donnan 1924) is then employed to calculate the negative fixed charge density that would

result in the measured Gd(DTPA) equilibrium. The cartilage fixed charge density is then translated into cartilage proteoglycan content by using the commonly accepted anionic content values associated with common cartilage proteoglycan aggregates (Maroudas et al. 1969).

NMR techniques have quantitatively validated the Donnan model with respect to the distribution of Na^+ ions in cartilage (Lesperance et al. 1992). However, several factors can cause osmotic systems to deviate from the ideal Donnan model (Helfferich 1962), and previous experiments suggest that Gd(DTPA) in cartilage may not obey ideal Donnan equilibria when the cartilage fixed charge density is greater than 30 mM (Donahue et al. 1994). The objective of this investigation was to quantify the equilibria of Gd(DTPA) between articular cartilage and a bathing NaCl solution, and thus improve our understanding of the role that ionic equilibria has on cartilage functionality as well as augment the interpretation of Gd(DTPA) related investigations of cartilage proteoglycan content.

2.4 Methods

2.4.1 Overall Protocol

Cartilage specimens were obtained from bovine patellae. All specimens were equilibrated in 137 mM phosphate buffered saline (PBS). After equilibration, one dimensional spin-lattice relaxation time constant (T_1) maps were collected along an arbitrary diameter of each cartilage disk. Each cartilage specimen was then bisected along a diameter. Half of each specimen was equilibrated in 137 mM PBS with 1mM Gd(DTPA), while the other half of each specimen was equilibrated in varying concentrations of PBS with 1 mM Gd(DTPA). The specimen halves were then reunited for a second series of one di-

dimensional T_1 maps, along the diameter perpendicular to specimen bisection. Two-dimensional T_1 maps were also acquired to evaluate the spatial homogeneity of the Gd(DTPA) associated T_1 reduction.

The quantification of glycosaminoglycans in the cartilage was conducted spectrophotometrically via a 1,9-dimethylmethylene blue (DMMB) assay (Farndale et al. 1982).

2.4.2 Cartilage Specimen Preparation

Patellae were obtained from veal calves within 6 hours of sacrifice, then stored on ice. Cylindrical cartilage specimens, 8.0 mm in diameter were cut in the same flat region of each patella. Each specimen was subsequently removed from the underlying cartilage-bone interface. Upon removal, each specimen was placed in 137 mM phosphate buffered saline (PBS) (Sigma P-4417) at 0°C with pH = 7.4. The mass of each cartilage specimen was measured periodically after placement into PBS until an asymptotic mass value was reached. This process took approximately two hours.

2.4.3 Cartilage Specimen Equilibration

All cartilage equilibrations were conducted at 0°C. Buffer solutions were made by making four serial dilutions to an 8X stock of PBS (Sigma P-4417). The resulting solutions were 8.0X, 4.0X, 2.0X, 1.0X, and 0.5X PBS. The contents of the PBS solution at 1X were: 0.01 M phosphate buffer, 0.0027 M potassium chloride 0.137 M sodium chloride, with a pH of 7.4. Gd(DTPA) (Berlex NDC 50419-188-02) was added, to each of the five resulting buffer solutions, to 1.0 mM. After collecting imaging data on the cartilage specimens without Gd(DTPA), the specimens were placed in the respective 50 mL solutions that contained 1.0 mM Gd(DTPA). The cartilage specimens were equilibrated

in these solutions for a period of 420 min. The mass of each cartilage specimen was measured before and after the 1.0 mM Gd(DTPA) equilibrations.

2.4.4 T₁ Projections

The one-dimensional T₁ (proton spin-lattice relaxation time) projection maps were acquired in a 2.0 Tesla field. A local gradient set was used, which was capable of producing 8 Gauss/cm. A solenoidal 8 turn 1 cm rf-coil was used. The direction of the projection images was perpendicular to that of the 2.0 Tesla field.

A series of projection images was collected to generate the T₁ projection maps. Each projection image was generated via a 90°-180° spin echo sequence, with no phase encoding and with frequency encoding in the direction of the projection. To map T₁, steady state repetitive projection images were obtained for various repetition times. For conditions prior to Gd(DTPA) incubation, the repetition times were 0.100 sec, 0.250 sec, 0.500 sec, 1.000 sec, 1.500 sec, 2.000 sec, 4.000 sec, and 6.000 sec. For conditions after the Gd(DTPA) incubation, the repetition times were 0.070 sec, 0.100 sec, 0.250 sec, 0.500 sec, 1.000 sec, 1.500 sec, 2.000 sec, and 3.000 sec. All one dimensional spin-echo projection images employed an echo time of 20 msec.

For each pixel, the image intensity from the one-dimensional images, at steady-state for a given repetition time, was fit via a least squares technique to equation 2.10.

$$I = A(1 - e^{-kT_R}) + C \quad [2.10]$$

where I is the steady-state image intensity, k is $1/T_1$, T_R is the repetition time, A is the equilibrium z-magnetization corrected for T₂ relaxation, and C is an arbitrary constant.

Prior to Gd(DTPA) incubation, the cartilage specimens were in the form of whole discs. After incubation in Gd(DTPA), the cartilage specimens were in the form of half discs. (See the '2.4.1 Overall Protocol' section.) The one-dimensional projection maps prior to Gd(DTPA) incubation were taken along an arbitrary diameter. After Gd(DTPA) incubation, all one-dimensional projections were taken with the two halves of each specimen placed adjacent to each other along their diameter of bisection, and oriented in the gradient set such that each one-dimensional projection image was collected along a direction perpendicular to the diameter of bisection. All cartilage specimens were oriented such that the articular surface was parallel to the direction of the 2.0 Tesla magnetic field.

2.4.5 Two-Dimensional T_1 Maps

Two-dimensional slice selective T_1 maps were collected to detect the possibility of an uneven Gd(DTPA) distribution. Each slice was collected along the same diameter as that of the one-dimensional projection images. Slice thickness was 2.0 mm. The two dimensional maps were generated from a series of two dimensional 90° - 180° spin-echo images. Each two-dimensional image employed a 20 msec echo time. Frequency encoding was in the direction perpendicular to the cartilage articular surface. Phase encoding was in the direction parallel to the cartilage articular surface. Different repetition times were employed to create the individual images with which the T_1 map was generated. The repetition times used were 100 msec, 250 msec, 400 msec, 750 msec, 1500 msec, and 3000 msec. Each pixel of the two-dimensional images was fit to equation 2.10 via a least squares technique.

2.5 Results

2.5.1 T_1 Projections of Cartilage Specimens

The T_1 measurements of the cartilage specimens are shown in table 2.1. For each cartilage specimen, the T_1 maps were homogeneous with random spatial fluctuations to the extent indicated by the standard deviations of the T_1 values. The T_1 spatial fluctuations were confirmed to be random by demonstrating that a given T_1 spatial pattern was not reproducible when repeating the T_1 mapping procedure on a cartilage specimen several times. The histograms of T_1 values within each cartilage specimen were approximately gaussian, as shown by a representative T_1 histogram in figure 2.1. Each T_1 projection contained approximately 230 pixels. The homogeneity of the T_1 maps, in a direction parallel to the articular surface, is demonstrated by the lack of non-random T_1 variations in a typical one-dimensional projection map shown in figure 2.2.

2.5.2 $Gd(DTPA)$ Induced T_1 Depression

The T_1 measurements indicated that the $Gd(DTPA)$ associated T_1 reduction in the cartilage specimens was more pronounced when the specimens were equilibrated in higher PBS concentrations. The means and standard deviations of the T_1 values, calculated from the T_1 projection maps, for each specimen half are shown in table 2.2. $Gd(DTPA)$ concentrations in the cartilage specimen halves were calculated via equation 2.11

$$g = \frac{1}{R} (r_1^* - r_1) \quad [2.11]$$

where g is the total cartilage $Gd(DTPA)$ concentration in mM, R is the relaxivity of $Gd(DTPA)$ in $(\text{mM-sec})^{-1}$, r_1^* is the cartilage proton spin-lattice relaxation rate after

Gd(DTPA) equilibration, and r_l is the cartilage proton spin-lattice relaxation rate prior to Gd(DTPA) equilibration. We employed a previously reported estimate for Gd(DTPA) relaxivity, $4.0 \text{ (mM-sec)}^{-1}$ (Donahue et al. 1994). The results of these calculations are shown in figure 2.3.

Figure 2.4 illustrates the asymptotic limit of Gd(DTPA) equilibria as a function of the ratio of the bathing NaCl concentration and the cartilage fixed charge density. The experimental data has a reasonable fit ($r = 0.99516$) to a Donnan model that incorporates a cartilage volume excluded to Gd(DTPA) penetration. This model is described by equations 2.12 and 2.13,

$$\frac{g^*}{g} = (1 - e)\Phi^Z \quad [2.12]$$

$$\Phi = -\frac{f}{2(1 - e)} + \sqrt{1 + \left(\frac{f}{2(1 - e)}\right)^2} \quad [2.13]$$

where Φ is the cartilage chloride ion equilibrium distribution, g^* is the Gd(DTPA) concentration inside the total cartilage volume, g is the Gd(DTPA) concentration outside the cartilage, f is the total cartilage negative fixed charge density as a fraction of the bathing NaCl concentration, e is the fraction of cartilage volume excluded from Gd(DTPA) penetration, and Z is the apparent charge of Gd(DTPA). Equation 2.12 is an analog of equation 2.2, and equation 2.13 is derived in section 2.2. Least squares fit of the model to the experimental results are shown in the figure for $Z = -2$ and $Z = -1$. An apparent Gd(DTPA) charge of -1 provides a much better fit than the does an apparent charge of -2.

When the apparent Gd(DTPA) charge was used as a fit parameter, the best fit yielded an excluded volume of 20% and Gd(DTPA) effective charge of -0.92 .

2.5.3 Two-dimensional T_1 Mapping

The one dimensional maps of figure 2.3 show a uniform T_1 distribution within each specimen half, which indicates a likelihood that there was enough time for Gd(DTPA) to fully equilibrate. However, a uniform two dimensional T_1 map lends further support to this notion, and reduces the possibility that the Gd(DTPA) diffusion was incomplete in a direction perpendicular to the cartilage specimen's surface. Figure 2.6 shows a slice selective two dimensional T_1 map generated from multiple two dimensional spin echo images of a cartilage specimen after bisection and Gd(DTPA) equilibration. Each half of the cartilage specimen has a uniform T_1 distribution with a similar level of T_1 noise as was seen in the one dimensional T_1 projection images of figure 2.3.

2.6 Discussion

Several MRI techniques to non-invasively measure proteoglycan content have been explored, such as the use of sodium NMR spectroscopy (Lesperance et al. 1992), in-vivo sodium imaging of articular cartilage (Reddy et al. 1998; Shapiro et al. 2000), and the use of contrast agents (Bacic et al. 1997), including Gd(DTPA) (Bashir et al. 1996; Bashir et al. 1997). The present study has used MRI to quantify the equilibrium of Gd(DTPA) between articular cartilage and a bathing saline solution, and tested the hypothesis that the Gd(DTPA) distribution is governed by ideal Donnan equilibria. A quantitative understanding of Gd(DTPA) equilibria in cartilage is essential to a meaningful interpretation of associated derivations of cartilage proteoglycan content.

The expectation that the fixed charge density associated with cartilage proteoglycan content reduces Gd(DTPA) transport into the cartilage interior was experimentally realized. The results were consistent with a Donnan model that included a provision for a cartilage volume inaccessible to Gd(DTPA) entry. The modified Donnan model derived here is different than the commonly accepted model (Bashir et al. 1996) in two respects. First the present model has an explicit incorporation of a cartilage volume inaccessible to Gd(DTPA) equilibration. Second, the present model does not dictate that the effective charge of the Gd(DTPA) complex is -2.

The prediction that the Gd(DTPA) charge is considerably less negative than -2 under physiological conditions is not inconsistent with previous equilibrium investigations of metal chelating agents. DTPA alone has five potentially ionizable groups with a wide range of pK values: 1.79, 2.56, 4.42, 8.76, and 10.42 (Werner and Grunder 1999), and it is common for DTPA metal chelates to be protonated at neutral pH (Durham et al. 1958). It is not clear what the protonation equilibrium properties of Gd(DTPA) are in the cartilage interior, and thus further experimentation would be required to confirm the effective Gd(DTPA) charge in cartilage. The effective charge estimated in figure 5 should be considered a purely empirical result.

The fit to the Donnan model indicates that the cartilage volume fraction available to Gd(DTPA) is approximately 80%. The major cartilage biopolymers, collagen and aggrecan, constitute a substantial cartilage volume fraction: approximately 20% as measured in our laboratory. Thus the accessible cartilage volume fraction unavailable to

Gd(DTPA) penetration is likely to be coincident to the volume occupied by the major cartilage biopolymers.

The results of this investigation indicate that efforts to quantify cartilage proteoglycan content from Gd(DTPA) equilibria should take into account the apparent charge of the Gd(DTPA) complex and the volume effects of the cartilage solid content. Cartilage solid content is an especially important parameter in this consideration since cartilage solid content may vary during pathological conditions.

| <u>specimen</u> | <u>T₁ (sec)</u> |
|-----------------|----------------------------|
| 1 | 1.33 ± 0.12 |
| 2 | 1.44 ± 0.13 |
| 3 | 1.38 ± 0.13 |
| 4 | 1.32 ± 0.12 |
| 5 | 1.73 ± 0.14 |

Table 2.1. T₁ measurements (at 2 Tesla) of the five cartilage specimens equilibrated in 137 mM PBS without Gd(DTPA). Standard deviations were obtained by considering each pixel of the T₁ projection maps to be one element of a population of T₁ measurements.

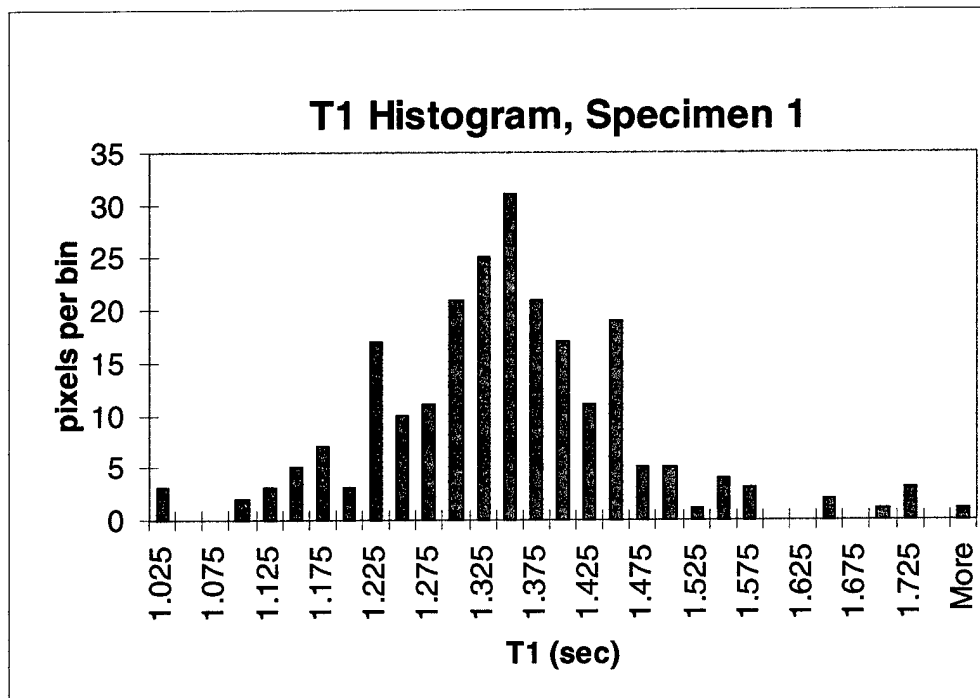


Figure 2.1. Distribution of T_1 values of a representative cartilage specimen equilibrated in 137 mM PBS without Gd(DTPA).

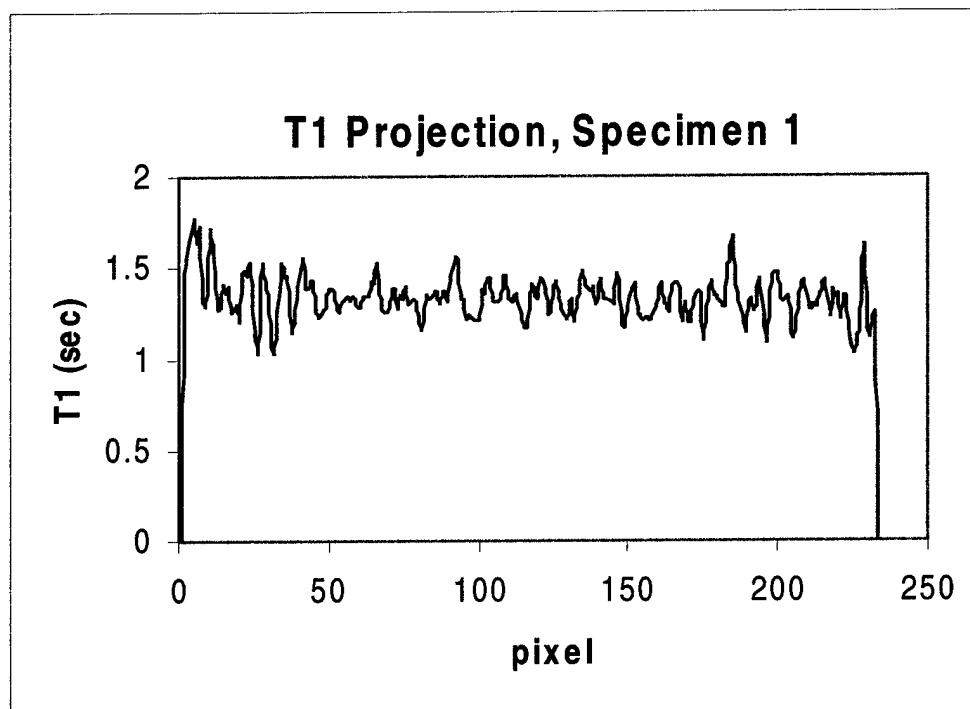


Figure 2.2. One-dimensional T_1 projection map of a representative cartilage specimen equilibrated in 137 mM PBS without Gd(DTPA). The thickness of one pixel is approximately 35 μm .

| <u>specimen</u> | <u>NaCl conc.</u> <u>(mM)</u> | <u>T₁ (sec)</u> | <u>T₁ (sec)</u> (when Nacl = 137) | <u>difference in T₁</u> <u>(%)</u> |
|-----------------|----------------------------------|----------------------------|---|--|
| 1 | 69 | 0.75 ± 0.11 | 0.47 ± 0.13 | -60 |
| 2 | 137 | 0.47 ± 0.06 | 0.43 ± 0.12 | -9 |
| 3 | 274 | 0.36 ± 0.05 | 0.44 ± 0.13 | 18 |
| 4 | 548 | 0.30 ± 0.03 | 0.46 ± 0.12 | 35 |
| 5 | 1096 | 0.30 ± 0.04 | 0.51 ± 0.14 | 41 |

Table 2.2. T₁ measurements of the five cartilage specimens equilibrated in PBS solutions of various NaCl concentrations with 1.0 mM Gd(DTPA). Standard deviations were obtained by considering each pixel of the T₁ projection maps to be one element of a population of T₁ measurements.

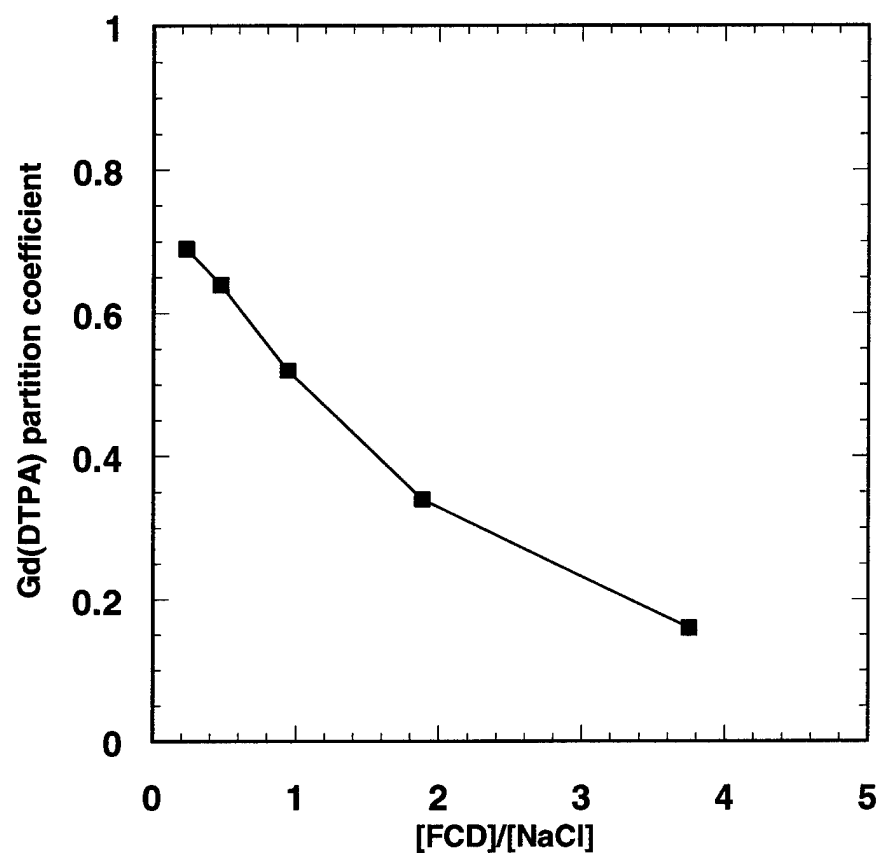


Figure 2.3. Partition coefficient of Gd(DTPA) transport between the cartilage interior and the bathing medium as a function of fixed charge density normalized to the NaCl concentration in the bathing medium.

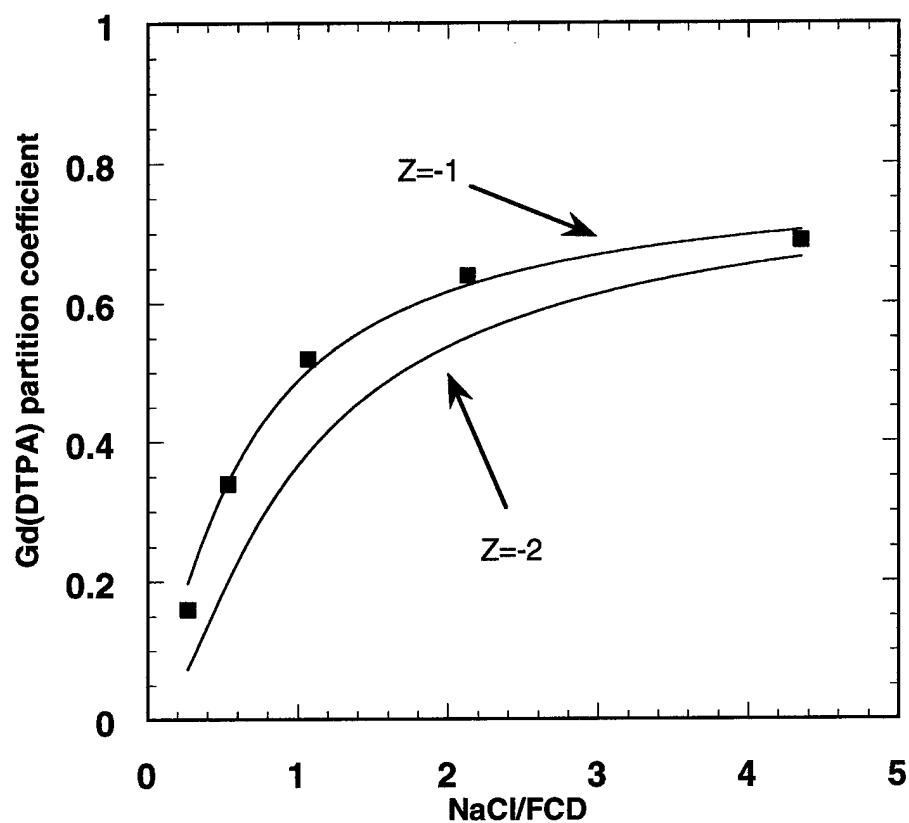


Figure 2.4. Gd(DTPA) transport partition coefficient as defined in figure 2.3 plotted as a function of the multiplicative inverse of the fixed charge density. The solid lines are least squares fits of equation 2.14 to the experimental results. The fits were performed for two apparent charges ($Z = -1$ and $Z = -2$) as indicated. The least squares fit when both the charge and excluded volume were considered parameters yielded an excluded volume of 20% and an effective Gd(DTPA) charge of -0.92 .

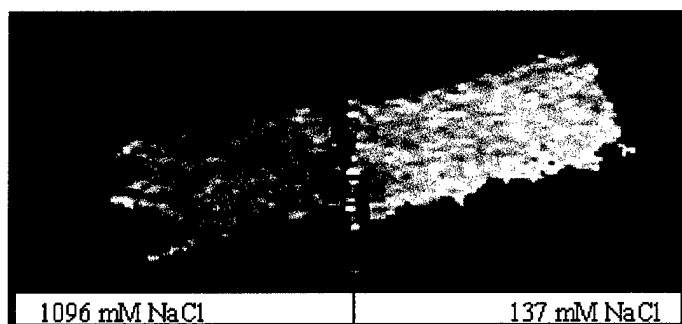


Figure 2.5. Slice selective two-dimensional T_1 maps of a cartilage specimen. The right and left portions of the figure correspond to halves of a cartilage disk after bisection. Each half of the cartilage disc was equilibrated in 1.0 mM Gd(DTPA) and saline concentrations as indicated in the figure.

CHAPTER 3

A METHOD FOR COMPRESSING ARTICULAR CARTILAGE WITHIN A MAGNETIC RESONANCE IMAGING ENVIRONMENT

3.1 Introduction

The normal function of articular cartilage involves compression. As articular cartilage is compressed, the fluid contained within the cartilage matrix is extruded into the joint space. The extruded fluid lubricates the contact points of opposing bone interfaces (McCutchin 1972). It is possible that cartilage that is too soft will compress to an unnatural extent, and provide a mechanical advantage for natural shear forces to disrupt the collagen framework. Additionally, soft cartilage may not be able to recover its original shape quickly enough to continue providing fluid to a bone interface during repeated loading. To test hypotheses about cartilage physiology and pathophysiology, it is useful to develop non-invasive imaging techniques for observing the functional performance of articular cartilage. We have developed a technology which helps explore the magnetic resonance imaging properties of articular cartilage specimens while simultaneously acquiring information regarding deformation. The design of a magnetic resonance imaging compatible cartilage compression device is presented.

3.2 Design

The pressure cell, shown in figure 3.1, consists of a pneumatically activated ceramic piston confined in a cylindrical chamber. The cartilage was positioned in the pres-

sure cell with its articular surface in contact with a porous glass filter (Corning 31001-10F). The filter led to a drain, which allowed extruded cartilage fluid to leave the cell.

The cylinder and cap of the pressure cell were made of Delrin (Dupont). This polymer exhibits no proton NMR signal, is nonmetallic, has an electrical resistivity on the order of $10^{14} \Omega\text{-cm}$ and a dissipation factor of 0.0048 at 10^6 Hz. The piston was made of a machinable ceramic, Macor (Corning). This ceramic has an electrical resistivity on the order of $10^{16} \Omega\text{-cm}$ and a loss tangent of 10^{-3} at 1 kHz and 10^{-4} at 8.5 GHz. The pore size of the glass filter was chosen such that it was impermeable to the solid matrix of the cartilage but freely permeable to the cartilage fluid. The compressed air that pneumatically activated the piston was prevented from traveling around the sides of the piston by a Teflon seal. Pressure was applied via a compressed air tank, and was measured by a digital pressure gauge (Omega DPG-500) on the regulator. A solenoid radio-frequency coil was wrapped around the cylinder of the pressure cell. The pressure cell was placed inside an 11 cm diameter local gradient set capable of generating 8G/cm. The cell and gradient set were then placed in the 1 meter bore of a 2 Tesla Oxford whole-body imaging magnet interfaced to a custom-built NMR spectrometer. The functionality of the compression cell was tested by performing several experiments on cartilage plugs as described below.

3.3 Experimental protocol

Cartilage specimens were obtained from the patella of bovine calves (ages ranged from 6 months to a year) within 10 hours from sacrifice. The cartilage specimens were stored and treated slightly differently than were the specimens used in chapter 2. Each

specimen was stored at -20°C for a period no longer than 20 days. Cartilage specimens were harvested from the flat portion of the articular surface of the patella. With a small spatula, each disc was peeled from the cartilage-bone interface. Prior to insertion into the pressure cell, each specimen was equilibrated in 10 mL of phosphate buffered saline (Sigma P-4417) at room temperature for 30 minutes.

In an effort to simulate articular cartilage in an early arthritic state, we exposed several cartilage specimens to a moderate proteolytic regime. Since it has been hypothesized that early stages of osteoarthritis involve the loss of proteoglycan content selectively, we chose a proteolytic agent that would selectively deplete the proteoglycan content of the cartilage while leaving the collagen network relatively intact. The proteolytic enzyme, trypsin, is known to cleave the core proteins of the proteoglycans while having little effect on the type-II collagen fibers which comprise the collagenous network of articular cartilage. The digested cartilage specimens referred to in this chapter were generated by incubating each cartilage specimen in a 10 mL volume of 1 mg/mL trypsin-(Sigma T-8253)/phosphate-buffered-saline-(Sigma P-4417) solution for 75 minutes at 37°C with slight agitation.

Slice selective images of each cartilage specimen in a plane coincident with a diameter of the cartilage disk and perpendicular to the cartilage surface were acquired. Slice thickness was 2 mm. In each case the cartilage specimen was oriented such that its articular surface was parallel to B_0 , the main magnetic field. All two-dimensional images were acquired with a standard 90° - 180° spin echo rf-pulse sequence. A 10 kHz bandwidth was used. The orientations of frequency and phase encoding are indicated in figure

3.1. Each image employed a 256 x 256 array of pixels. All images were acquired using a 2 Tesla full body imaging magnet integrated with a custom built spectrometer. Local gradients that enclose the pressure cell were constructed that provide up to 8 gauss per cm. All rf pulses were applied via a solenoidal coil tuned to the proton frequency having 6 turns and a diameter of 2.5 cm. Imaging data were analyzed using the Interactive Display Language interpreter on a Silicon Graphics workstation.

Pressure was applied to the cartilage in the form of a step function. Prior to pressure application, a series of two-dimensional 90^0 - 180^0 spin-echo images were acquired. The compression was driven by a pressure of 0.690 MPa (100psi). After the 80 minutes of constant pressure application, the pressure of 0.690 MPa was maintained for a subsequent set of image acquisitions. The cartilage fluid which emanated from the pressure cell drain was assayed for the presence of proteoglycan content via a dimethylmethylene blue spectrophotometric assay (Farndale et al. 1982).

3.4 Results

Figures 3.2 and 3.3 illustrate compression of both normal and proteoglycan depleted cartilage specimens. The signal to noise ratio of these images is approximately 7. On average, the normal cartilage specimens compressed by approximately 38%. The proteoglycan depleted cartilage specimens compressed by approximately 50%. The result that the proteoglycan-depleted specimens were less resistant to mechanical compression is consistent with the notion that a reduction in cartilage fixed charge density leads to a reduced osmotic pressure within the cartilage interior. Although the viscoelastic behavior of articular cartilage is not simple, a description of the equilibrium resistance of articular cartilage as a compressed ideal spring provides a first approximation of cartilage com-

lage as a compressed ideal spring provides a first approximation of cartilage compressive modulus as defined by equation 3.1

$$\sigma = Ee \quad [3.1]$$

where σ is compressive pressure, E is compressive modulus, and e is compressive strain. In this analysis, the compressive modulus of normal articular cartilage is approximately 1.8 MPa, and the compressive modulus of proteoglycan depleted articular cartilage is approximately 1.38 MPa. The proteoglycan depletion, in this case, caused a 23% loss of compressive resistance. The compressive moduli are presented here with the caveat that, according to prior literature (Mow et al., 1980), these compressive events most likely exceeded the compressive elastic limit of articular cartilage, and thus the values of compressive moduli are probably overestimates of what would be found for milder compressive events.

It should be noted that it is difficult to interpret results regarding the cartilage articular surface, since substantial image artifacts exist at the boundary between the cartilage specimen and the porous glass filter. The artifacts present as localized regions of bright signal intensity and a non-smooth articular surface.

The results of the proteoglycan assays of extruded cartilage fluid indicated no measurable proteoglycan content, indicating that cartilage compressive events involve minimal extrusion of solid content.

3.5 Discussion

The functionality of a novel cartilage compression device has been demonstrated. The effective compression of small articular cartilage specimens was shown for both

normal cartilage specimens and cartilage specimens softened by selective enzymatic degradation. The degree of cartilage compression as a response to a pressure of 0.69 MPa is consistent with previous biomechanical results reported in the literature (Mow et. al. 1980). The major challenge with the compression device is that small yet significant imaging artifacts are present at the cartilage to glass filter interface. The size of the artifacts is several orders of magnitude larger than the roughness of the filter surface. One likely source for the imaging artifacts is the possibility of magnetic susceptibility effects resulting from trapped air in the filter. During compression, the presence of image artifacts substantially reduce.

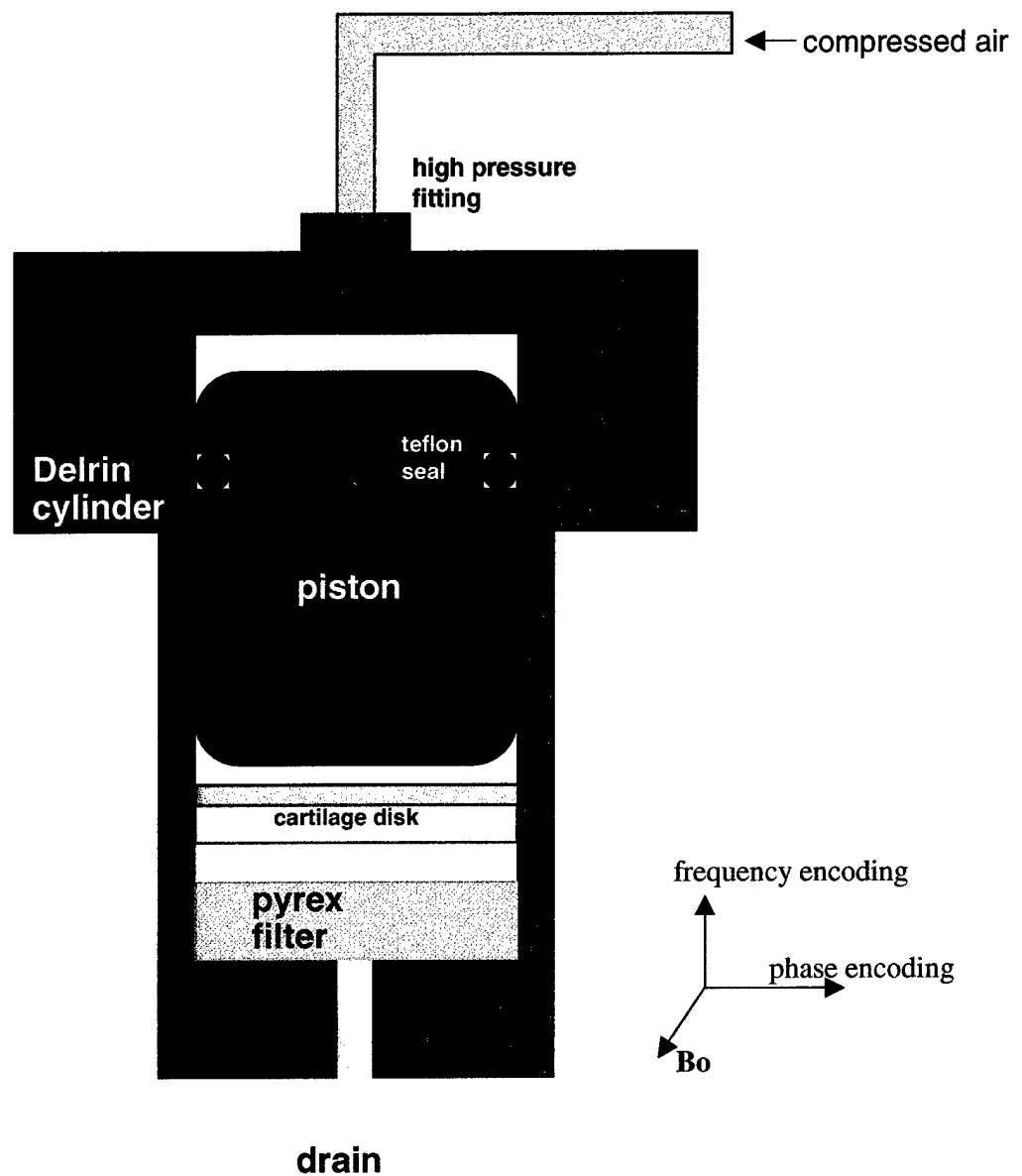


Figure 3.1. Cross sectional diagram of MR compatible pressure cell. Compressed air exerts a pressure on a piston that is confined in a cylindrical shaft. The piston, when responding to the pressure from the compressed air, pushes on the specimen that is positioned between the cylinder and a Pyrex filter, which allows cartilage fluid to extrude from the cell.

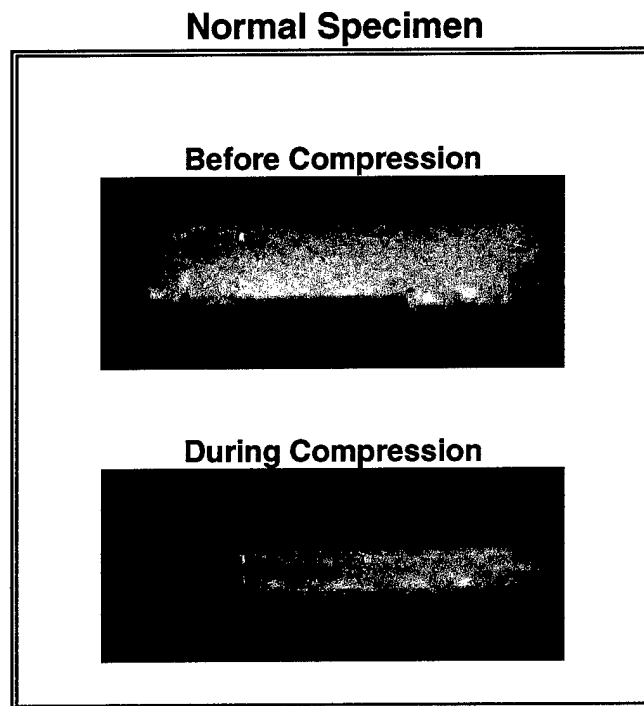


Figure 3.2. Two-dimensional slice selective 90° - 180° spin echo images of a normal articular cartilage specimen prior to and during compression. Cartilage orientation is such that the articular surface is on the bottom. The cartilage specimen is compressed from above by a ceramic piston onto a porous glass filter. Imaging artifacts from the cartilage surface to glass filter interface are visible in both images, and are more apparent in the image prior to compression.

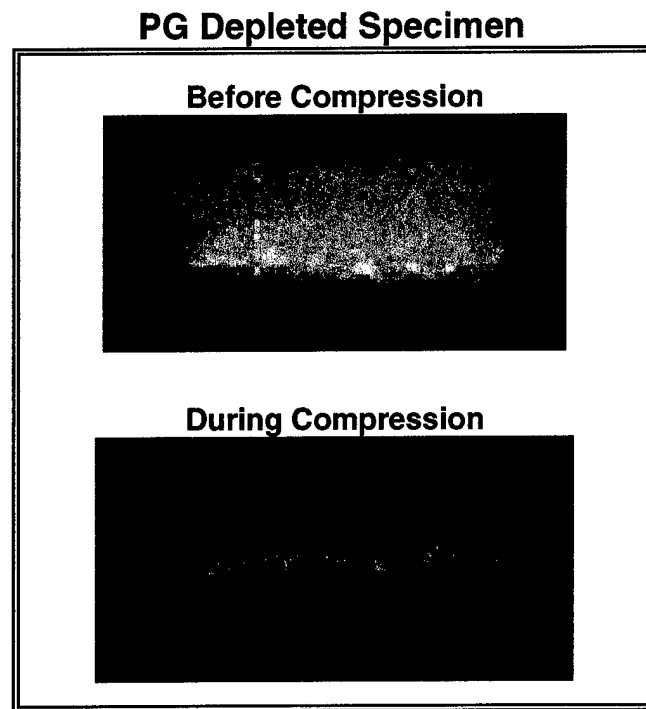


Figure 3.3. Two dimensional slice selective 90° - 180° spin echo images of a proteoglycan depleted articular cartilage specimen prior to and during compression. Cartilage orientation is such that the articular surface is on the bottom. The cartilage specimen is compressed from above by a ceramic piston onto a porous glass filter. Imaging artifacts from the cartilage surface to glass filter interface are visible in both images, and are more apparent in the image prior to compression.

CHAPTER 4

SPECTROSCOPIC MAGNETIC RESONANCE IMAGING PARAMETERS OF ARTICULAR CARTILAGE DURING COMPRESSION

4.1 Purpose and objective

Chapter 1 introduced several investigations that have used proton MRI to observe cartilage image dynamics during compression (Lehner et al. 1989; Rubenstein et al. 1996). These studies could only report qualitative effects because MR relaxation time constants were not measured. In the present experiment we use standard inversion recovery and the standard (90° - 180°) spin-echo technique to obtain proton MR relaxation characteristics of cartilage during mechanical compression. We also examined the effects of enzymatic proteoglycan depletion on the observed compression induced trends in relaxation times.

In addition to spectroscopic measurements, the MR relaxation times of articular cartilage during compression are studied in more detail by constructing two-dimensional maps of cartilage MR proton relaxation time constants. The two-dimensional maps prevent the measurement of cartilage MR relaxation characteristics from being influenced by water signal emanating from within the porous Pyrex filter of the MR compatible compression device. Furthermore, the MR relaxation time constant maps permit the observation of spatial variations in cartilage MR relaxation properties.

4.2 Experimental protocol

4.2.1 Cartilage Specimens

Cylindrical cartilage plugs (1 cm in diameter) were harvested, each from the flat surface of a bovine patella. All patellae were stored at -20°C prior to the experiment. Each cartilage specimen was sectioned with a diamond core drill then peeled from the cartilage-bone interface with a spatula. The specimens were subsequently inspected to ensure that there was no visible damage and that all cartilage layers remained intact. Each specimen was equilibrated in phosphate buffered saline (pH = 7.4) for 30 minutes.

Several cartilage specimens were exposed to enzymatic digestion. Since it has been hypothesized that early stages of osteoarthritis involve the selective loss of proteoglycan content, we chose a proteolytic agent that would deplete the proteoglycan content of the cartilage while leaving the collagen network relatively intact. The digested cartilage specimens were generated by incubating each cartilage specimen in 5ml of 1.0 mg trypsin /ml phosphate -buffered saline solution for 60 minutes. The end stage digestion media was analyzed for proteoglycan content via a spectrophotometric assay (Farndale et al. 1982). In each case, the proteoglycan concentration in the media was approximately 1.3 mg/ml which corresponds to an approximate 30% proteoglycan depletion.

4.2.2. Cartilage Compression

The cartilage compression device and rf-coil design were the same as described in chapter 3. Each cartilage compression event consisted of a constant pressure of 0.69 MPa was employed for a duration of 180 minutes.

4.2.3. NMR Relaxation Time Constant Measurements

The standard inversion recovery technique was employed to obtain proton T_1 measurements. For normal cartilage specimens, the inversion time was varied by step

times of 200 msec before compression and 100 msec during compression. For the proteoglycan depleted cartilage specimens, the inversion time varied by step times of 250 msec before compression and 125 msec during compression. In each case 30 free induction decays (*fids*) were acquired. Each *fid* contained 1024 data points at a sampling rate of 0.1 msec.

To measure proton T_2 , the standard Hahn spin-echo technique (Hahn 1950) was employed, as modified by Carr and Purcell. See "Method A" within (Carr and Purcell, 1954). For normal cartilage, the echo time (*tau*) was varied by 25 msec before compression and 10 msec during compression. For proteoglycan depleted cartilage, *tau* was varied by 20 msec before compression and 8 msec during compression. Spectra at 30 time points were acquired for each T_2 measurement. For each time point, 200 *fids* were averaged to obtain a spectrum.

4.2.4. MR Relaxation Time Constant Mapping

We constructed maps of the spin-lattice, T_1 , and spin-spin, T_2 , relaxation times for each position of the cartilage imaging slice corresponding to an image pixel. In general, the relaxation time maps were constructed from fitting equations 4.1 and 4.2

$$I = A(1 - \exp(-TR/T_1)) + B \quad [4.1]$$

$$I = C \exp(-TE/T_2) \quad [4.2]$$

where I is image intensity, TR is the repetition time, TE is the echo time, and A, B, C are arbitrary constants, to a series of 90° - 180° spin-echo images employing different echo times and different repetition times. Five images were used to construct each T_1 map. All

were acquired with an echo time of 20 msec, and had the following repetition times: 0.5 sec, 1.0 sec, 1.5 sec, 2.0 sec, and 2.5 sec. Six images were used to construct each T_2 map. All were acquired with a repetition time of 2.0 sec, and had the following echo times: 20 msec, 30 msec, 40 msec, 50 msec, 60 msec, and 70 msec. The collected images were fit to equations 4.1 and 4.2 using a gradient expansion algorithm for a non-linear least squares fit. It is important to note that this technique for mapping the T_2 relaxation time constant is not independent of diffusion effects, and thus the T_2 values that we report deviate from true T_2 values since our method has not incorporated a diffusion-weighting factor (Neeman et al. 1990; Brandl et al. 1994). As early as 1954, Carr and Purcell have demonstrated the contribution of diffusion when observing T_2 decay with a series of individual spin echo events to be

$$My_d = -M_0 \exp[\gamma^2 D t^3 / 12 n^2], \quad [4.3]$$

where My_d is the contribution of diffusion, γ is the gyromagnetic ratio, D is the diffusion-constant, t is duration that a spin ensemble experiences a gradient, and n is the number of echoes (Carr et al. 1954). Considering our experimental parameters of gradients no larger than 8 gauss/cm, and using a diffusion constant of 10^{-5} cm²/sec, we estimate that diffusion can influence our T_2 measurements by a factor of approximately 10%.

In addition, given the fixed set of repetition times, our method for mapping T_1 has an inherent limitation on the range of T_1 values. This limitation is especially important when considering T_1 values near the lowest repetition time of 0.5 sec. A calibration of our T_1 mapping technique with copper sulfate doped agarose phantoms of known T_1 and cartilage specimens (where we measured bulk T_1 with an inversion recovery technique)

indicated that our T_1 mapping procedure yielded T_1 values accurate to within an approximate 50% range.

4.3 Results

4.3.1 Spectroscopic Measurements

Figures 4.1-4.3 show typical curve fits when calculating relaxation time constants. Table 4.1 presents a summary of the data obtained regarding the effects of compression and proteoglycan depletion on cartilage proton and sodium MR relaxation times. The inherent parameters: proton- T_1 , proton- T_2 are delineated for the four physio-mechanical cartilage states: normal-uncompressed, normal-compressed, proteoglycan-depleted-uncompressed, and proteoglycan-depleted-compressed.

Each parameter was evaluated, using a two-tailed t-test, to determine if proteoglycan depletion had a significant effect on any of the MR time constants. The resulting P values are given in the last column of table 4.1.

Since the relaxation time constants throughout the imaging slice of the cartilage specimens were not uniform prior to compression, we have calculated T_1 and T_2 histograms of the normal and degraded cartilage specimens prior to and after compression. T_1 histograms for both specimens before and after compression are shown in figures 4.8-4.9. We should note that experimental factors could have contributed to the relaxation time distributions. For example, the width of the T_1 histogram could represent noise in the T_1 map rather than represent an actual T_1 distribution, especially since T_1 in cartilage has been shown to be relatively homogeneous (Xia et al. 1998). When testing this notion by evaluating the pixel by pixel reproducibility of T_1 maps of cartilage specimens and

There is no evidence that proton- T_1 changes with proteoglycan-depletion, and scarce evidence, if any, that proton- T_2 changes.

Compressing cartilage provided a means for introducing a proteoglycan-depletion induced change in proton- T_2 . In the compressed state (using the same pressure), the proton- T_2 of the proteoglycan-depleted cartilage is shorter than that of normal cartilage. Furthermore, the change in proton- T_2 associated with compression is substantially more pronounced for proteoglycan-depleted cartilage than it is for normal cartilage.

The data also affords an evaluation of the changes in proton relaxation time constants associated with compression. To compliment the values displayed in table 4.1, we report the statistical significance of the compression associated changes in relaxation time in table 4.2.

4.3.2 Relaxation Maps

Spin-lattice (T_1) and spin-spin (T_2) magnetic resonance relaxation time constant maps were generated from a series of slice selective spin-echo images acquired both before and after compression of the cartilage. These maps are shown in figures 4.4-4.7 for representative normal and trypsin degraded cartilage specimens. In contrast to the proton density weighted images shown in chapter 3, the relaxation time maps had a uniform intensity only after compression. Prior to compression, T_1 was fairly heterogeneous throughout the imaging slice, and high values of T_2 were predominantly located in the region of the articular surface in both the normal and trypsin degraded cases. agarose phantoms, we found relatively little consistency. However, the fact that the T_1 distribution narrows upon compression could implicate the existence of T_1 heterogeneity. Although there was a re-

duction in T_1 for both specimens upon compression, the change in T_1 for the degraded specimen, upon compression, was substantially more dramatic than that corresponding to the normal specimen.

T_2 histograms for both specimens before and after compression are shown in figure 4.10-4.11. Unlike the case for T_1 , The reduction in T_2 for both the normal and degraded specimens were similar. However, T_2 measurements for the degraded specimen both before and after compression were slightly higher than those for the normal specimen. As is indicated in the images of figures 4.5 and 4.7, the histograms of figures 4.10-4.11 likewise indicate that both relaxation time constants become more uniform upon compression for normal and degraded cartilage.

From the T_1 and T_2 histograms, we have calculated average values of T_1 and T_2 prior to and post compression for both the normal and degraded specimens. These values are given in Table 4.3. Notice that the values in table 4.3 differ substantially from the corresponding values of table 4.1. The methods for measuring relaxation times are different in each case. Also, the values in table 4.1 include contributions from the fluid contained within the Pyrex filter.

4.4 Discussion

The central theme of this experiment was to identify proteoglycan depletion induced trends in proton MR relaxation times. These trends could serve as potential contrast mechanisms that indicate early cartilage degeneration and thus early signs of osteoarthritis. Since the normal functionality of articular cartilage involves compression, we have measured the MR relaxation times of articular cartilage in both uncompressed and

mechanically compressed states. One motivation for the introduction of mechanical compression is that it has been hypothesized that cartilage softening may be the earliest known indicator of osteoarthritis. The establishment of cartilage compression and proteoglycan depletion permitted an evaluation of proteoglycan depletion induced changes in proton and sodium MR characteristics of cartilage in the normal state and during mechanical compression.

The results of the present study have implications for clinical research in cartilage imaging. Standard clinical proton imaging that employs basic T_1 and T_2 contrast mechanisms is unlikely to distinguish proteoglycan depletion in articular cartilage since we have demonstrated that proton T_1 and T_2 do not vary significantly with proteoglycan depletion. However, we have demonstrated that, when cartilage is in a mechanically compressed state, a significant change in proton T_2 does occur with proteoglycan depletion. This result indicates that it may be possible to identify regions of articular cartilage that have a low proteoglycan content with T_2 weighted proton imaging, if the cartilage of interest is in a compressed state. A limitation worth mentioning is that compressed state proton T_2 changes associated with proteoglycan depletion are on the order of magnitude of their standard deviation among samples. Therefore, relaxation time constant, alone, may provide information on relative proteoglycan depletion (i.e. a measure of cartilage degradation over time), but will require additional information to make an absolute prediction of proteoglycan depletion. In-vivo, mechanical compression of articular cartilage can be induced physiologically by having subjects perform certain exercises prior to imaging. Experimental evidence supports the notion that the rate of cartilage recovery is

slow enough to permit MRI measurements of cartilage thickness dynamics during recovery (Eckstein et al. 1998).

In addition to clinical implications, the results reported in this study are relevant to understanding the physiological mechanisms of cartilage deformation and NMR relaxation mechanisms in cartilage. For example, the proton relaxation time constants reported here are consistent with those of previous work where cartilage compression was performed via an osmotic technique prior to MR evaluation at atmospheric pressure (Lusse et al. 1995). The consistency of the present results with those cited indicates that changes in compression-induced proton MR characteristics can be generated by both mechanical or osmotic pressure gradients. This conclusion has implications for in-vitro proton MR cartilage studies in that investigators should be careful to match the osmolarity of cartilage tissue culture media with that of synovial fluid. A further implication is that it is possible that baseline measurements of cartilage proton relaxation times in vivo can be influenced on the osmolarity by a subject's synovial fluid.

With the assumption that proteoglycan-depletion is the primary cause of cartilage softening, these results indicate that it may be possible to infer cartilage softening via an indirect measurement of proteoglycan content, by measuring cartilage proton MR relaxation time constants during mechanical compression.

The experiments described in this chapter also expand upon earlier progress to identify early manifestations of osteoarthritis using magnetic resonance imaging such as observations of MR signal intensity changes across the depth of the cartilage (Paul et al. 1993), and measurements of MR relaxation time constants of normal and degraded carti-

lage (Lehner et al. 1989). MR relaxation times have also previously been observed to change in a depth dependent fashion in normal articular cartilage specimens during compression (Rubenstein et al. 1996). Our present observations of the MR properties of bovine specimens of articular cartilage are consistent with these previous studies. However, we were unable to observe consistent depth dependent results with all specimens. This inconsistency could result from the likelihood that juvenile cartilage specimens (which we used) are likely to be structurally distinct from adult cartilage (Torzilli et al. 1988). In addition, with our technique, it was difficult to assess the MR characteristics of the cartilage at the articular surface since some imaging artifacts did arise from the interface of the cartilage with the glass filter.

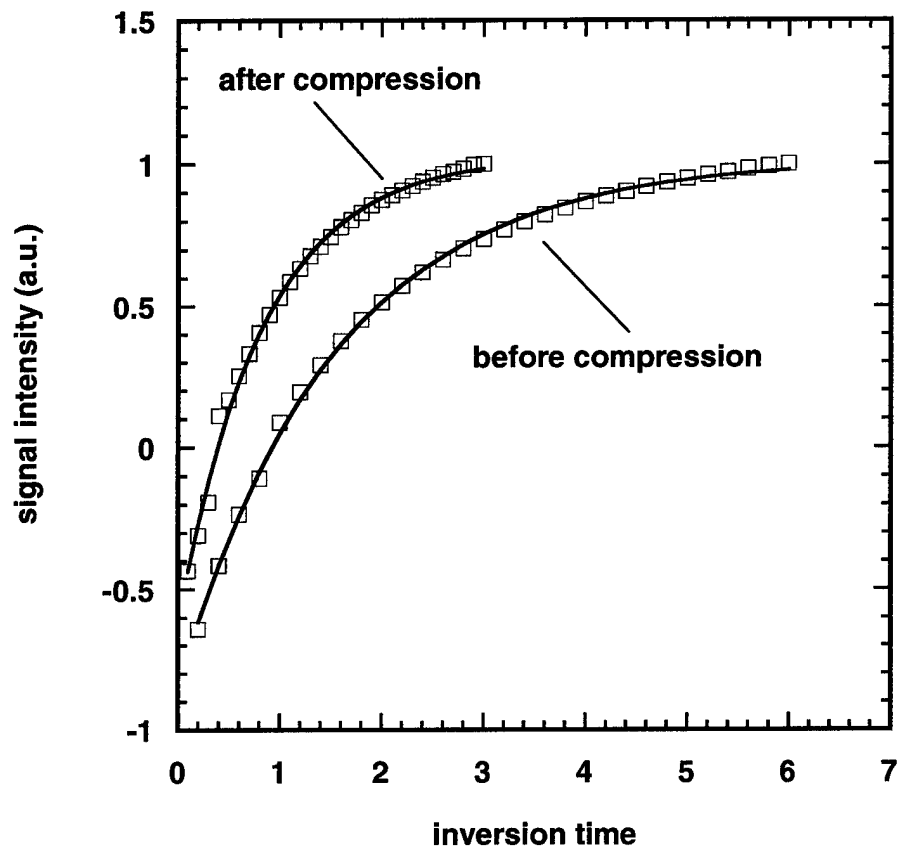


Figure 4.1. Typical proton spin-lattice relaxation time constant data fit to exponential functions.

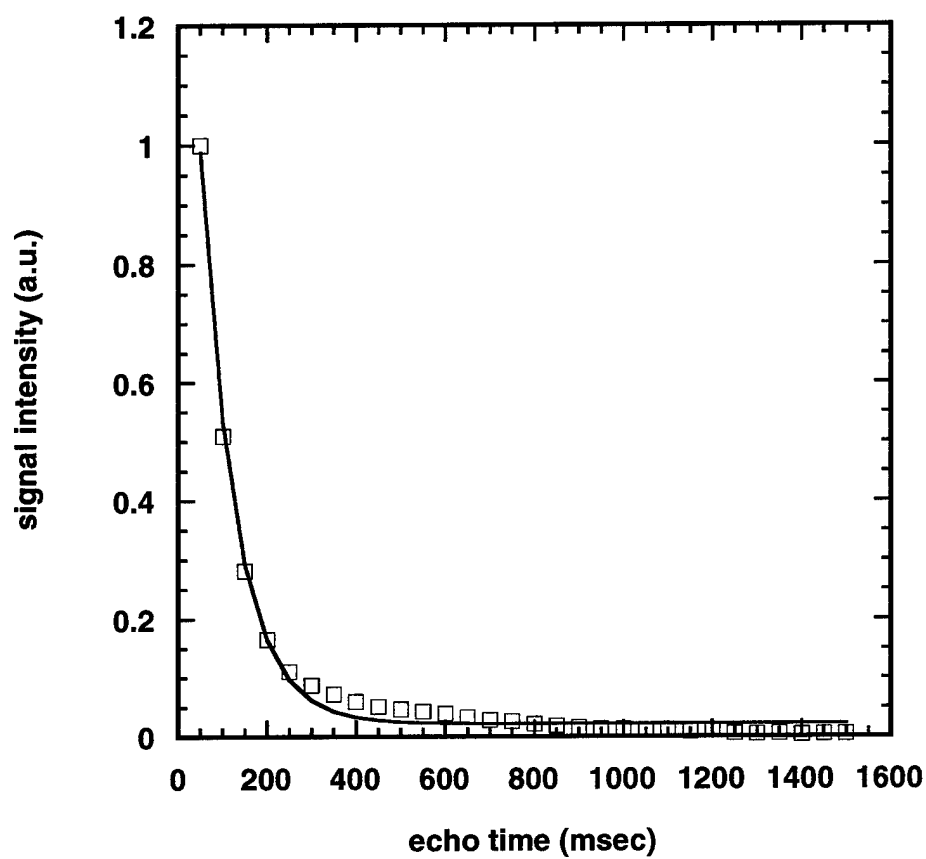


Figure 4.2. Typical spin-spin relaxation time constant data, prior to compression, fit to an exponential function.

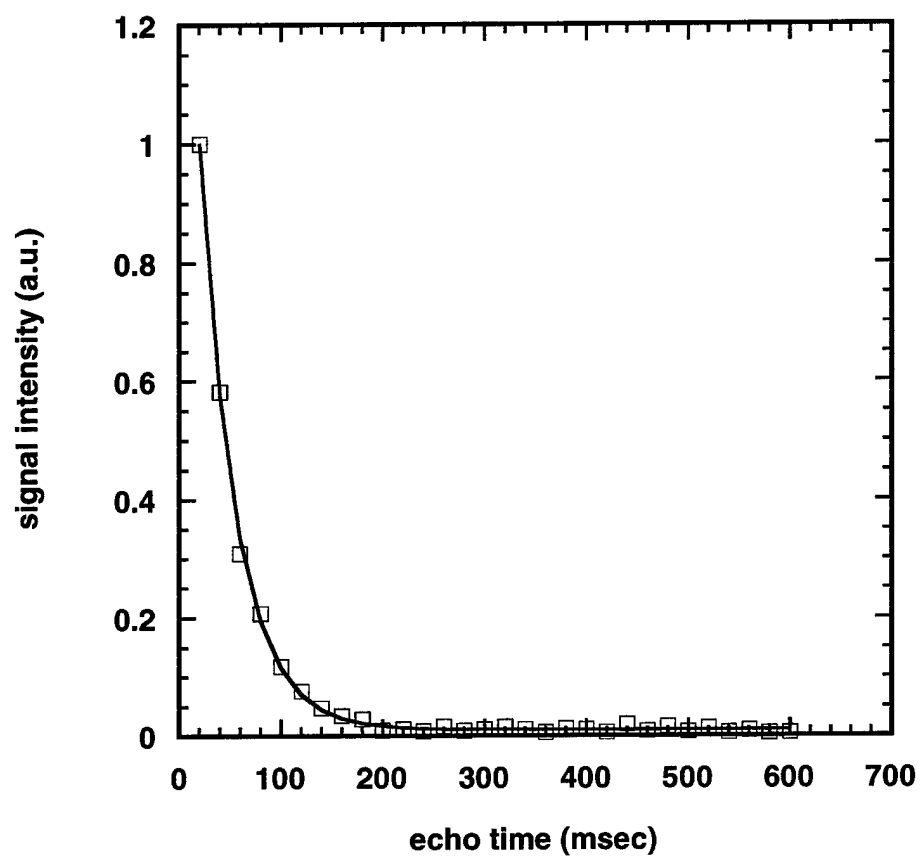


Figure 4.3. Typical spin-spin relaxation time constant data, post-compression, fit to an exponential function.

| | Full Compression | Normal | PG depleted | P |
|------------------------------|------------------|-------------|-------------|-------|
| proton T ₁ (sec) | N | 1.54 ± 0.06 | 1.52 ± 0.09 | 0.658 |
| proton T ₁ (sec) | Y | 0.99 ± 0.10 | 1.07 ± 0.09 | 0.217 |
| %change | | -35.6 ± 7.9 | -29.5 ± 5.8 | 0.205 |
| proton T ₂ (msec) | N | 82.4 ± 2.7 | 90.6 ± 10.6 | 0.155 |
| proton T ₂ (msec) | Y | 38.8 ± 2.6 | 29.6 ± 6.2 | 0.028 |
| %change | | -52.9 ± 2.5 | -67.1 ± 6.8 | 0.007 |

Table 4.1. Proton relaxation parameters. Relaxation times are given for proton T₁, and proton T₂ for cartilage in the normal and mechanically compressed state. A comparison is drawn between these parameters for normal cartilage and cartilage that has been enzymatically treated to induce proteoglycan depletion. In each case, five cartilage specimens were used. The relaxation times reported are the corresponding means. In addition to relaxation times, the per-cent change between the normal and compressed state is given. For each normal vs. proteoglycan-depleted comparison, the results of a two-tailed t-test is given in the rightmost column labeled "P"; the value in this column represents the probability that the normal and proteoglycan-depleted values could have arisen from sampling a single population.

| Normal/Degraded | Relaxation Time Constant | P value |
|-----------------|--------------------------|----------|
| Normal | T1 | 1.60E-05 |
| Normal | T2 | 5.00E-09 |
| Degraded | T1 | 4.00E-05 |
| Degraded | T2 | 3.20E-05 |

Table 4.2. The statistical significance of the change in relaxation time constants associated with compression.

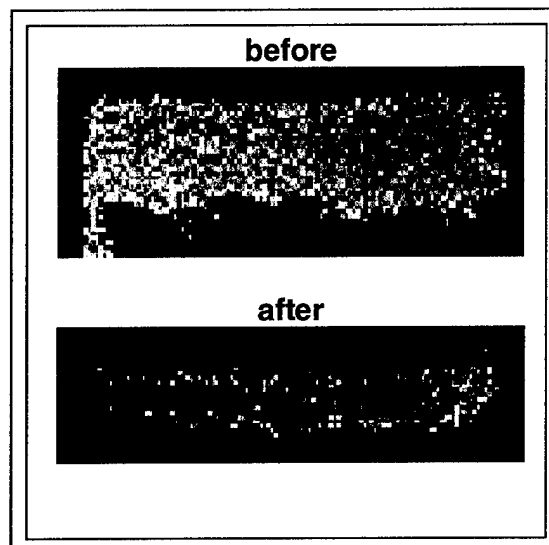


Figure 4.4 Two-dimensional slice selective T_1 maps of cartilage specimen before and after compression.

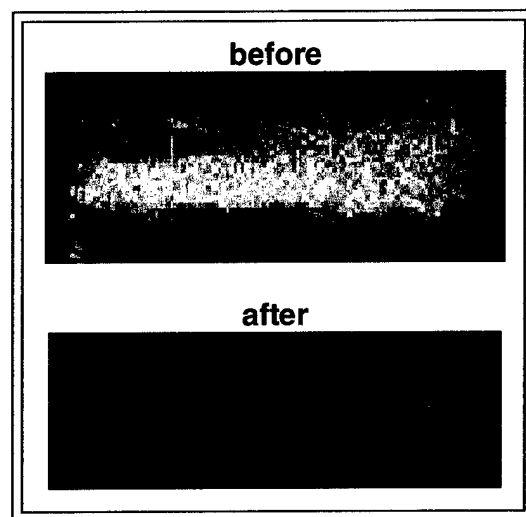


Figure 4.5 Two dimensional slice selective T_2 maps of cartilage specimen before and after compression.

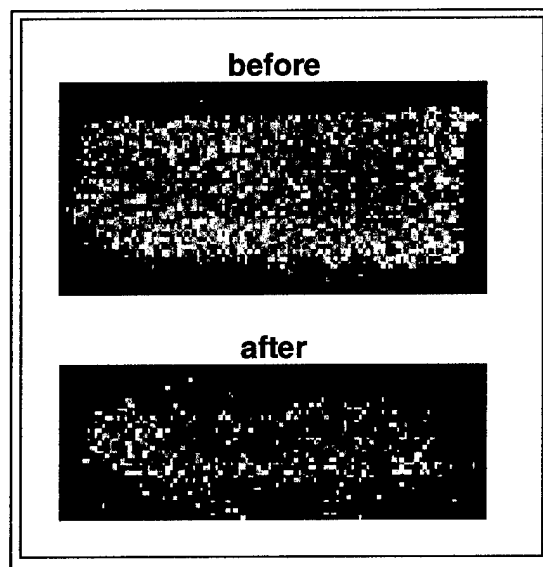


Figure 4.6 Two-dimensional slice selective T_1 maps of proteoglycan depleted cartilage specimen before and after compression.

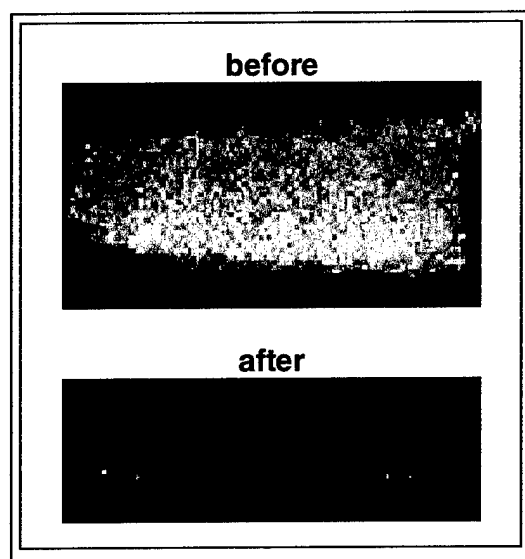


Figure 4.7 Two-dimensional slice selective T_2 maps of proteoglycan depleted cartilage specimens before and after compression.

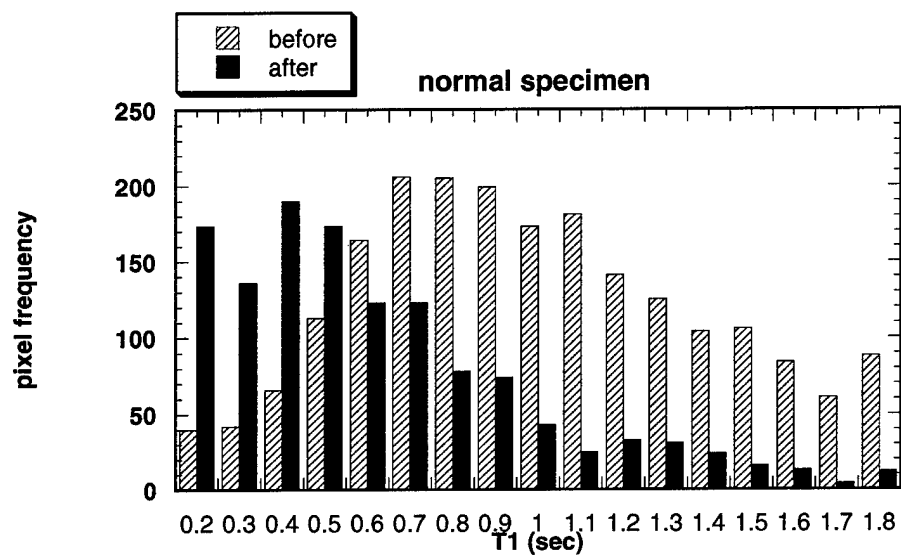


Figure 4.8 T₁ histogram of normal cartilage specimen.

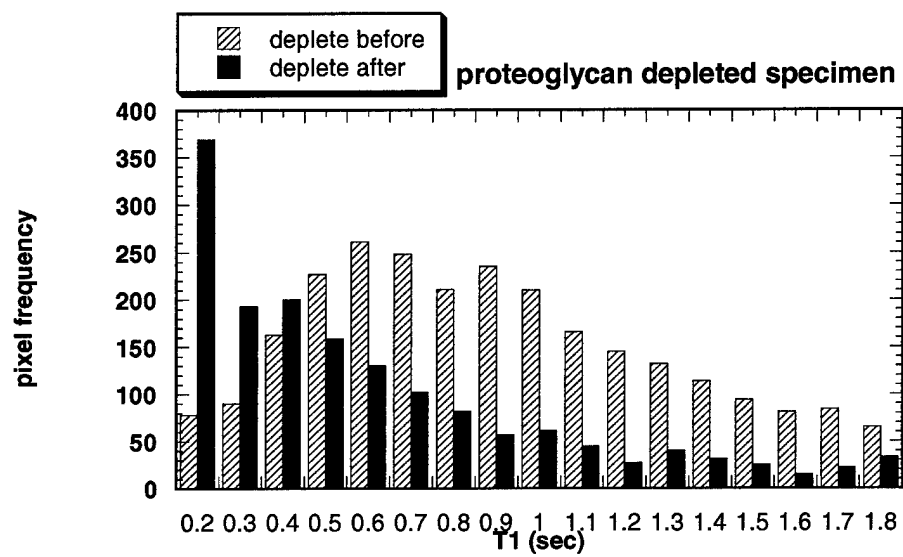


Figure 4.9 T_1 histogram of proteoglycan depleted cartilage specimen.

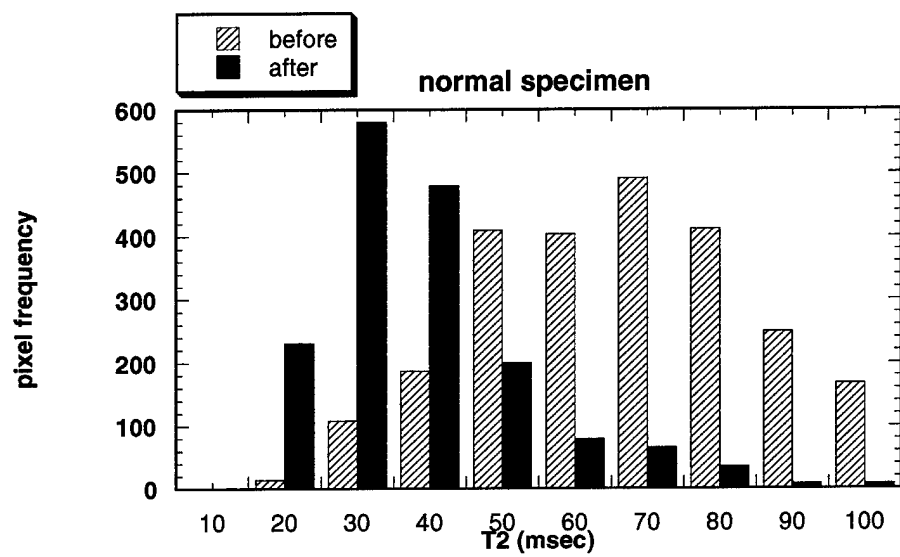


Figure 4.10 T₂ histogram of normal cartilage specimen.

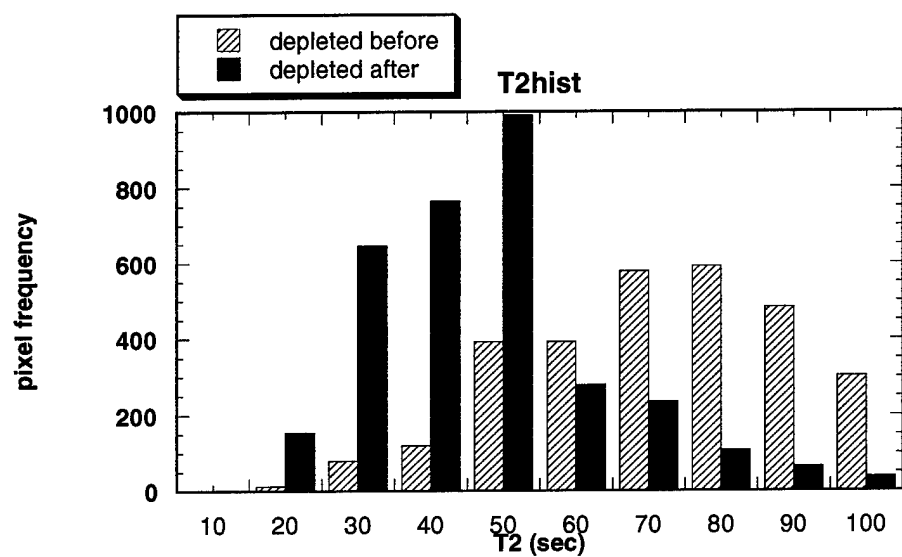


Figure 4.11 T₂ histogram of proteoglycan depleted cartilage specimen.

| | T1(sec) | T2(msec) |
|-----------------|---------|----------|
| Normal Before | 0.99 | 66.4 |
| Normal After | 0.62 | 38.4 |
| Degraded Before | 0.91 | 71.9 |
| Degraded After | 0.60 | 46.9 |

Table 4.3 Proton MR mean relaxation time constants of normal and proteoglycan depleted cartilage specimens. Degradation was conducted via a proteolytic regime discussed in the experimental protocol section.

CHAPTER 5

THE CARTILAGE UNI-AXIAL CONFINED COMPRESSION EXPERIMENT WITHIN A MAGNETIC RESONANCE IMAGING ENVIRONMENT

5.1 Introduction

The cartilage compressions demonstrated in chapter 3 indicated static conformations of a cartilage specimen before and after a continuous compressive event. The dynamics of cartilage conformation during the deformation process would lend insight into cartilage rheological mechanisms. This chapter describes a technique that employs MRI to monitor cartilage compression with a temporal resolution on the order of seconds.

5.2 Methods

One method of measuring the mechanical properties of a viscoelastic material is with the uniaxial confined deformation creep experiment. In this method, a constant pressure is applied to the viscoelastic material as the deformation of the material is measured as a function of time (Fung 1965). In the context of the experiment with cartilage, a first step is to keep the experimental parameters one dimensional such that the analytical aspects are manageable (Mow et al. 1990). This is primarily possible with cartilage as a consequence of the tissue's natural deformation mechanism. Cartilage can be thought of as a substance that, in bulk, is incompressible unless fluid extrusion is permitted. We thus confined the cartilage discs laterally, while allowing fluid to extrude from the articular surface. In this way, both the pressure and the response is contained in one dimension, the direction perpendicular to the articular surface.

The uniaxial confined deformation creep experiment was chosen as a method to measure the viscoelastic properties of the cartilage specimens. This kind of experiment was first employed on cartilage specimens by Mow and coworkers (Mow et al. 1984). In this experiment, a pressure is applied to the cartilage in the form of a step function. Prior to pressure application, a series of two-dimensional 90^0 - 180^0 spin-echo images were acquired. Upon compression, one dimensional 90^0 - 180^0 spin-echo image projections were acquired every 5 seconds for a period of 80 minutes. The compression was driven by a pressure of 0.690 MPa (100psi) which was established within the first 20 seconds of the one-dimensional-projection-image acquisition period, and was maintained for the duration of the creep experiment.

5.3 Results

To measure the compressive response of the cartilage disc to the applied pressure, we derived the thickness of the cartilage specimen from the one-dimensional 90^0 - 180^0 spin-echo image projections that were acquired every 5 seconds over a period of 80 minutes. Six of these projections are shown in figure 5.1 as examples. The presence of signal intensity in these projections indicates the presence of protons, and for the most part indicates the presence of the cartilage. Toward the left hand side of the peak is a low intensity plateau that corresponds to the water within the pores of the permeable glass filter. The representation of this projection does not have sharp edges. Two experimental factors contribute to this lack of sharpness. First, the cartilage specimen was not exactly perpendicular to the phase encoding direction. The tilt was slightly less than 3 degrees. Second,

a susceptibility artifact existed at the interface between the cartilage specimen and the ceramic piston as well as between that cartilage specimen and the glass filter.

The thickness of the cartilage was thus estimated as the full width of the projection at half its maximal value. The thickness calculation entailed a linear interpolation of signal intensity for regions between those represented by pixels. The thickness calculation was performed independently for each one-dimensional projection. The one-dimensional projection images were not collected beyond the 80-minute data acquisition period; it is likely, based on the trend of the creep curves, that the cartilage specimens would have compressed further given more time.

We arrived at using the full width at half maximum for the cartilage thickness by starting with the assumption that our signal acquisition is independent of position within the field of view. We therefore convoluted a hypothetical rectangular object in frequency space with various passive filter functions putatively representing the effect of our measurement system (including rotations of the rectangular object that correspond to the cartilage tilt) and found that the signal intensity at the positions corresponded to the edges of the initial box function always contained the value of half the maximum height of the resulting curve.

Given that we have deduced the cartilage thickness at 5 second intervals during the deformation creep experiment, we calculated strain at each of these time points, defined as the fractional change in thickness of the cartilage from its initial non-compressed state as described by equation 5.1

$$e_i = \frac{L_i - L_0}{L_0} \quad [5.1]$$

where e_i is strain at time i , L_i is cartilage thickness at time i , and L_0 is the initial cartilage thickness.

In doing so, we obtained the deformation creep curves shown in figure 5.2, which are similar to those found in previous purely mechanical studies (Mansour et al. 1976; Mow et al. 1980). Most notably, Mow et al. observed a 15% strain for an applied pressure of 0.1 MPa. The shape of the creep curve generated in Mow's experiment is similar to the shape we obtain, and has a similar time constant. We have fit these curves to a general exponential decay function given by equation 5.2,

$$e = m_1 \left(1 - \exp \left(-\frac{t}{m_2} \right) \right) + m_4 \left(1 - \exp \left(-\frac{t}{m_5} \right) \right) + m_3 \quad [5.2]$$

where e is strain, t is time, and $(m_1, m_2, m_3, m_4, m_5)$ are fit parameters. Two time constants were required for an adequate fit. The least squares fit results are given in table 5.1.

5.4 Discussion

There are a multitude of theories describing the mechanical properties of articular cartilage that include the electrostatic interactions among negatively charged proteoglycans (Buschmann et al. 1995), the viscous interaction between the cartilage fluid and its solid matrix (Mow et al. 1984), and the microstructural organization of cartilage (Schwartz et al. 1994). It has been proposed that purely viscoelastic models of articular cartilage may not be adequate for a comprehensive treatment of the mechanical properties of cartilage (McCutchen et al. 1982). However, the distinction between poroelastic and

viscoelastic deformations could be a matter of semantics. Viscoelastic models are found to be consistent with numerous experimental observations (Kovach et al. 1996).

We chose to apply a simple rheological model to our data and expand it as necessary. Since the data from our deformation creep experiment at first glance approximates a function that exponentially rises to a fixed value, we chose the Voigt (Fung et al. 1965) viscoelastic model shown in figure 5.3 which is described by equation 5.3.

$$e = \frac{P}{E} \left(1 - \exp \left(-\frac{E}{v} t \right) \right) + c \quad [5.3]$$

where e is strain, P is pressure, E is the elastic modulus, v is the viscosity, and c is an arbitrary constant. However, we found that two time constants were necessary for an adequate fit to our observations. Thus, the mathematical description of two Voigt solids in series adequately fit the data as shown in figure 5.2.

Our experiment was designed to mimic physiological pressures which are well beyond the elastic limit, which does place limits on the present physical interpretation of a viscoelastic model. However, we can state that the deformation creep observations are consistent with the notion that the cartilage rheology can be described by a linked deformation of two components.

In general the observed changes in permeability and elastic moduli resulting from degradation are consistent with mechanical studies involving alternative arthritic models, such as a canine surgically induced arthritic model (Setton et al. 1994), as well as other enzymatic degradation models (Bader et al. 1994). Furthermore, our observations that permeability increases with trypsin digestion is consistent with the notion that a reduction

in fixed charge density within the cartilage matrix induces an increase in permeability (Gu et al. 1993).

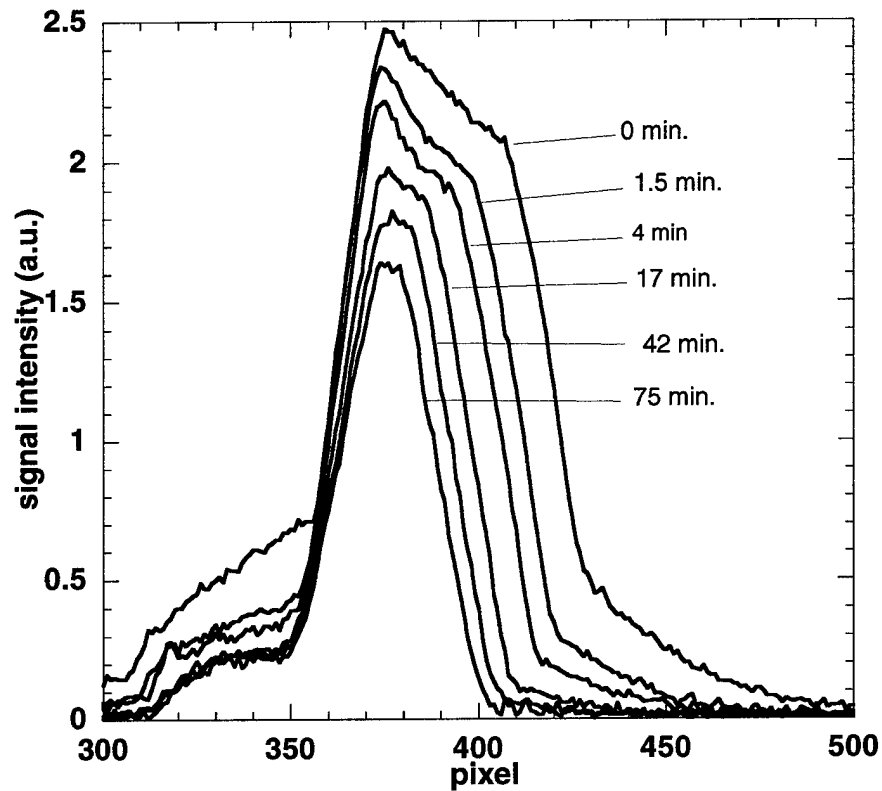


Figure 5.1 One dimensional 90^0 - 180^0 spin-echo projection images of the cartilage specimen. Six projections are shown at various times after onset of pressure application as indicated in the figure. The plateau on the left corresponds to water held within the glass filter shown in figure 1. The left hand slope of the projection corresponds to the articular surface of the cartilage specimen. The right hand side of the projection corresponds to the cartilage-bone boundary. The compressive force is from right to left against the stationary glass filter.

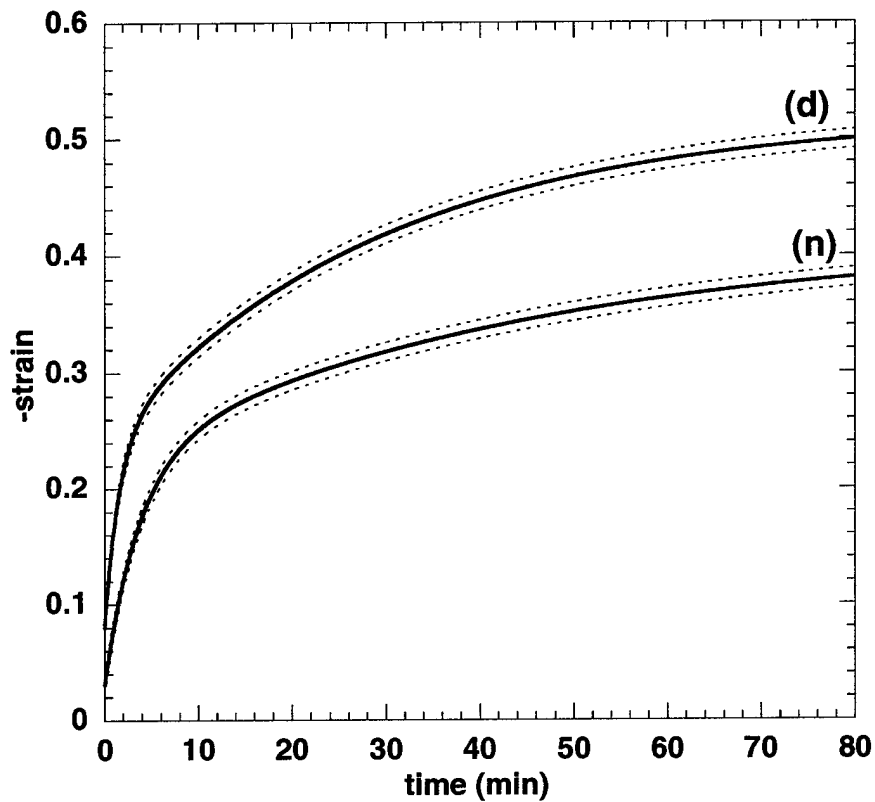


Figure 5.2 Deformation creep curve of normal and degraded cartilage specimens. Strain, defined as the fractional change in cartilage thickness resulting from a constant pressure application of 0.690 MPa, is shown as a function of time. the solid lines represent biexponential least squares fit to the cartilage thickness calculations, represented as circles. The curve for the normal cartilage specimen is labeled (n), and the curve corresponding to the trypsin degraded cartilage specimen is labeled (d). The standard deviations of strain measurements are shown as dotted lines.

| parameter | normal | degraded |
|-----------|--------|----------|
| m1 | 0.183 | 0.275 |
| m2 | 43.3 | 29.2 |
| m3 | 0.031 | 0.080 |
| m4 | 0.195 | 0.162 |
| m5 | 3.71 | 1.57 |

Table 5.1 The deformation creep data of figure 5.3 were fit to the biexponential decay function given in equation 5.2.

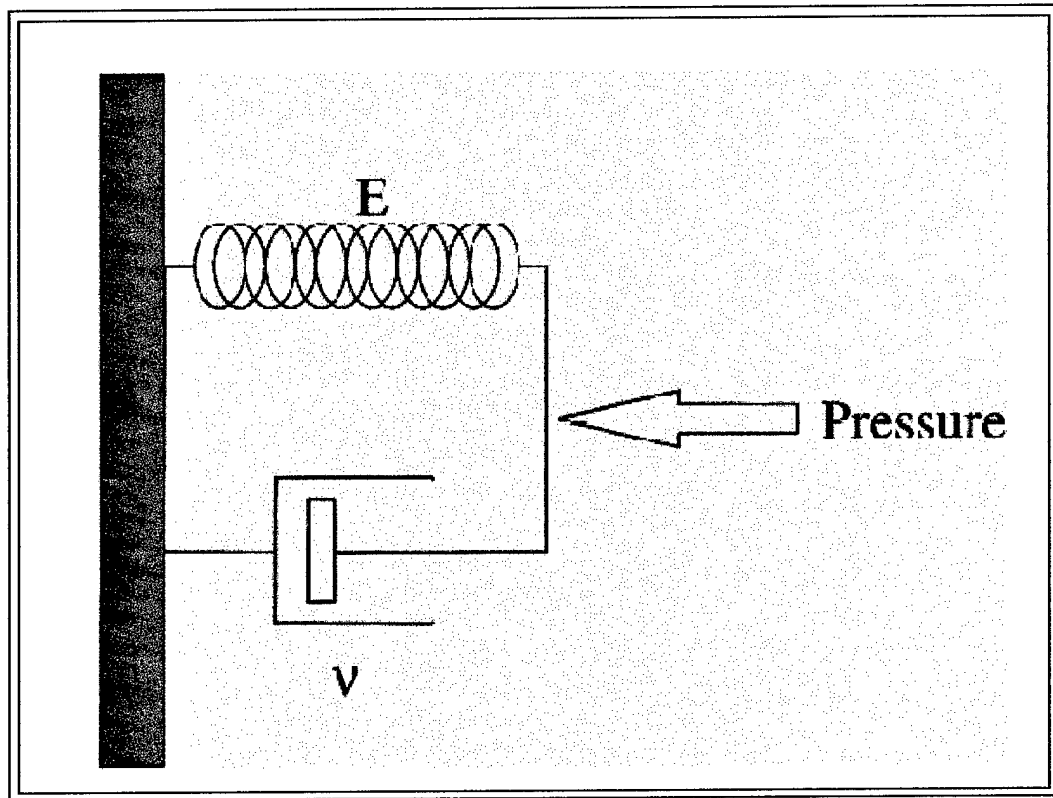


Figure 5.3 Voigt viscoelastic model. This basic viscoelastic model consists of an elastic spring arranged in parallel to a viscous dashpot. As indicated, E is the elastic modulus, and v is the viscosity.

CHAPTER 6

ARTICULAR CARTILAGE FLUID PERMEABILITY DURING COMPRESSION

6.1 Introduction

Second to bulk modulus, the most fundamental parameter that describes the deformation characteristics of cartilage is permeability. The ease with which fluid is able to travel through the cartilage matrix dictates how quickly or slowly cartilage deforms in response to an applied load. A first approximation of the way that cartilage permeability affects the cartilage deformation rate is described in the previous chapter by equation 6.3. Cartilage permeability can be derived from the cartilage deformation creep curves of chapter 6. This chapter describes the method for doing so, and also provides an example calculation that corresponds to the creep curves of figure 6.2.

6.2 Permeability Calculation

The data from the deformation creep experiment permits us to calculate the permeability of the cartilage assuming that the deformations are within the elastic limit. The most direct approach to calculating permeability within this experimental context is to use Darcy's Law which states that the velocity of the fluid in a permeable solid matrix is linearly proportional to the pressure gradient (Mansour et al. 1976). The permeability of the matrix, k , is defined as the constant of proportionality. This relationship is expressed symbolically in equation 6.1.

$$\mathbf{v} = k\nabla p \quad [6.1]$$

where v is the velocity, and p is the pressure. All three variables in this relationship are assumed to be functions of both space and time.

Since our experimental setup is designed to study the deformation of cartilage in one dimension (i.e. the cartilage is confined such that it cannot expand laterally), we can treat equation 6.1 in a one dimensional fashion where x is position. Since our experiment collects data at discrete time points, it is useful to explicitly include time in a discrete fashion as indicated by equation 6.2 where the subscript, i , indicates a particular point in time.

$$k_i = \frac{v_i}{\left(\frac{dp}{dx}\right)_i} \quad [6.2]$$

It will be useful to express equation 6.2 completely in terms of parameters derived directly from a deformation creep experiment, namely: L_0 , the original thickness of the cartilage; P , the constant pressure applied to the cartilage; L_f , the equilibrium thickness of the cartilage under pressure P ; Δt , the time step between each data acquisition; and e_i , the strain at time step i .

Since the fluid can be considered incompressible for our purposes, for the sake of simplicity, we make the approximation that the velocity of the fluid at all points within the cartilage is uniform and can be expressed as

$$v_i = \frac{\Delta L_i}{\Delta t}, \quad [6.3]$$

where

$$\Delta L_i = L_i - L_{i-1} \quad [6.4]$$

and L_i is the thickness of the cartilage at time i . Furthermore, since our working definition of strain is

$$e_i = \frac{L_i - L_0}{L_0}, \quad [6.5]$$

a substitution of equation 6.5 into equation 6.3 yields an explicit expression for v_i

$$v_i = \frac{L_0 \Delta e_i}{\Delta t}, \quad [6.6]$$

where

$$\Delta e_i = e_i - e_{i-1}. \quad [6.7]$$

Let us assume for simplicity that the elastic properties of the cartilage specimen are homogeneous. With this assumption, and since there are no pressure sources or sinks within the cartilage volume, the pressure gradient throughout the cartilage volume is constant. Thus, the pressure can be expressed as a linear function of space

$$p = Ax + B \quad [6.8]$$

where A and B are defined by the boundary conditions. Not all of this pressure, however, affects the velocity of the interstitial fluid, since a portion, p_e , is absorbed by the elastic resistance of the cartilage

$$p_e = Ee \quad [6.9]$$

where E is the elastic modulus of the cartilage. The change in pressure across the thickness of the cartilage is thus

$$\Delta p = P - p_e = P - Ee \quad [6.10]$$

where P is the constant applied pressure. The elastic modulus, E , of the cartilage can be defined by the equilibrium strain for a given pressure

$$E = \frac{P}{(L_f - L_0)/L_0} \quad [6.11]$$

Substituting equation [6.11] into [6.10] and dividing by the thickness of the cartilage at time i leads to the uniform pressure gradient given by

$$\left(\frac{dp}{dx} \right)_i = (P/L_i) \left(1 - \frac{e_i L_0}{(L_f - L_0)} \right) \quad [6.12]$$

Substituting equation 6.12 and 6.6 into equation 6.2 we obtain an explicit expression for permeability in experimentally derived terms

$$k_i = \frac{L_0 \Delta e_i}{\left(\frac{P \Delta t}{L_i} \right) \left(1 - \frac{e_i L_0}{(L_f - L_0)} \right)} \quad [6.13]$$

The biexponential fits to the deformation creep data, when substituted into equation 6.13 provide plots of permeability as a function of strain given in figure 6.1. The figure indicates that, in the uncompressed state, the trypsin degraded specimen is approximately twice as permeable to the normal specimen, and that the increase in permeability with respect to strain is sharper than that of the normal specimen. The permeability of the specimen in the region of high strain (greater than 0.3) is unlikely to be accurately represented by this method since the fluid velocity in this range becomes small. Additionally, in the region of high strain, our experimental conditions exceed the elastic limit for articular cartilage as reported by (Mow et al. 1980). Figure 6.2 shows the permeability, calculated in the same manner, as a function of time for the deformation of both the normal and degraded specimen. This figure shows that during the course of deformation, the degraded specimen is initially more permeable than the normal specimen, but after approximately 5 minutes of sustained compression, the degraded specimen loses its per-

meability with respect to the normal specimen. This phenomenon is most likely the result of the degraded specimen's increased strain.

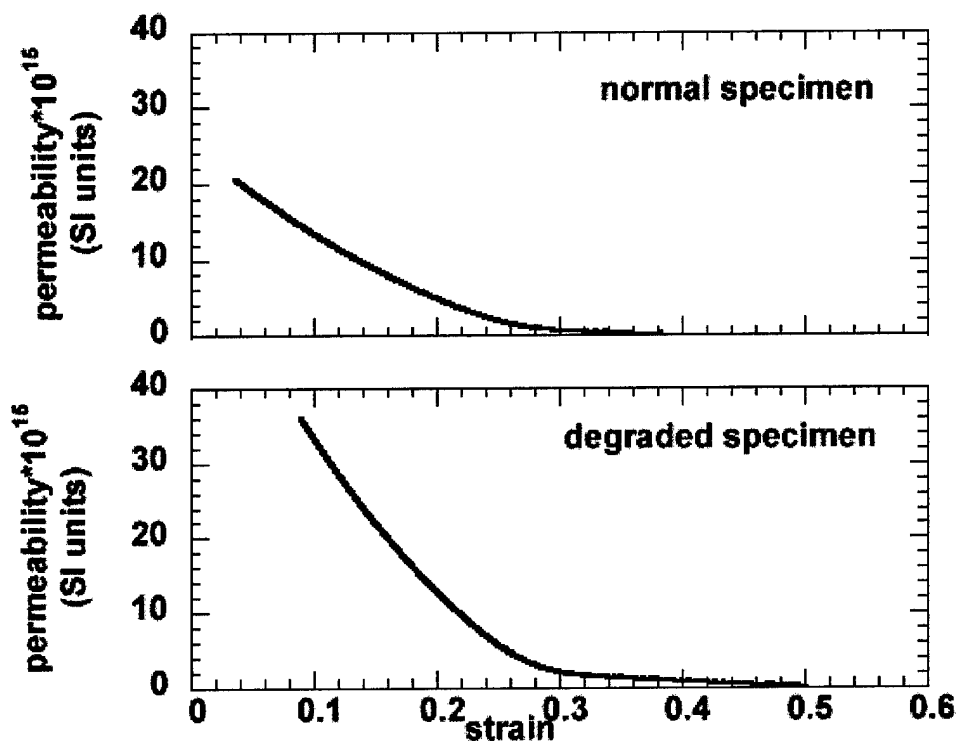


Figure 6.1 Permeability of the normal and degraded cartilage specimens as a function of strain, defined as the absolute value of the fractional change in cartilage thickness during compression.

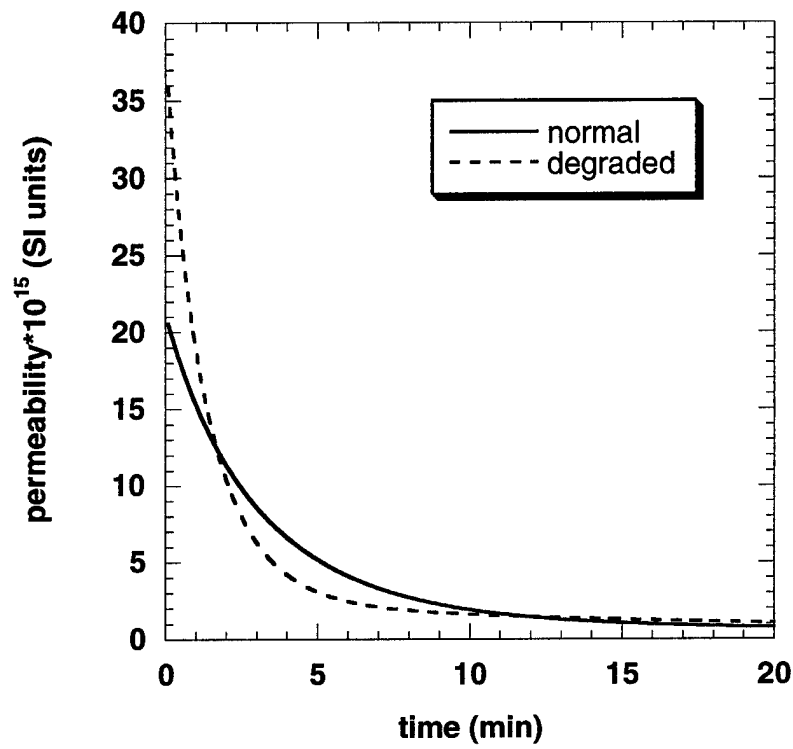


Figure 6.2 Permeability of the normal and degraded cartilage specimens as a function of time

CHAPTER 7

MULTI-NUCLEAR STUDY OF THE CARTILAGE OSMOTIC MODEL

7.1 A Theory of Cartilage Hydrostatic Pressure

The compressive resistance of articular cartilage is provided, in part, by an osmotic effect associated with the increased sodium content as described in chapter 2. The hydrostatic pressure of a dilute solution bounded by a semi-permeable membrane is described by the ideal gas law (Fermi 1936)

$$P = \mu RT, \quad [7.1]$$

where P is pressure, μ is the difference in dissolved particle concentration between the inside and outside of the membrane, R is the ideal gas constant, and T is absolute temperature.

The variable μ in equation 7.1 can be expressed in term of Donnan equilibria using the derivations provided in chapter 2. Specifically μ can be approximated by,

$$\mu = n^* - n + c^* - c, \quad [7.2]$$

where n^* and n are the sodium ion concentrations inside and outside of the cartilage specimen respectively; and c^* and c are the chloride ion concentrations inside and outside of the cartilage specimen. Recall that the normalization convention of chapter 2 (that the bathing sodium chloride concentration is one unit) indicates

$$n = c = 1, \quad [7.3]$$

thus

$$\mu = n^* + c^* - 2. \quad [7.4]$$

Equations 2.4, 2.5, and 2.9, when combined, indicate that

$$\mu = \frac{x^2 + 1}{x} - 2, \quad [7.5]$$

with

$$x = -\frac{f}{2(1-s)} + \sqrt{1 + \left(\frac{f}{2(1-s)}\right)^2}, \quad [7.6]$$

where f is the cartilage fixed charge density, and s is the excluded volume fraction. Figure 7.1 illustrates a numerical graph of equations 7.5 and 7.6.

The cartilage mechanical response to pressure can be derived as the osmotic consequence of the increase in fixed charge density associated with a cartilage fluid volume reduction. A cartilage specimen in the uncompressed state has an initial fixed charge density f in a fluid volume of $1-s$. As the cartilage specimen is longitudinally compressed by e , expressed as a fractional amount of the uncompressed thickness, the cartilage specimen fluid volume becomes $1-s-e$. Thus, modifying equation 7.6 to take into account confined compression yields

$$x = -\frac{f}{2(1-s-e)} + \sqrt{1 + \left(\frac{f}{2(1-s-e)}\right)^2} \quad [7.7]$$

A graphical illustration of equations 7.5 and 7.7 is given in figure 7.2. Equation 7.7 illustrates the sodium and chloride ion balance of cartilage specimens during the confined compression experiment as a function of pressure. This balance provides a framework for testing the cartilage ionic model via interleaved sodium and proton MRI.

7.2 Methods

7.2.1 Overall Protocol

Cartilage specimens were compressed *in-vitro* with a constant 0.69 MPa pressure as in chapters 3 through 6. However, in the present case, both sodium and proton MR projection images were acquired in an interleaved fashion. MR relaxation time constants of the two nuclei were measured prior to and post compression.

7.2.2 Hardware Modifications

The same MR compatible pressure cell, described in detail in chapter 3, was employed for the interleaved sodium/proton acquisition experiments. However, the rf coil was modified. A double tuned solenoid rf coil was incorporated into the pressure cell. The transmit/receive solenoidal RF coil was double tuned to the Larmor frequencies of ^1H (86.1 MHz) and ^{23}Na (22.7 MHz) as described by Schnall et al. 1985.

7.2.3 Proton and Sodium Relaxation Time Measurements

The standard inversion recovery technique was employed to obtain proton T_1 measurements. For normal cartilage specimens, the inversion time was varied with step times of 200 msec before compression and 100 msec during compression. For the proteoglycan depleted cartilage specimens, the inversion time varied with step times of 250 msec before compression and 125 msec during compression. In each case 30 free induction decays, (FIDs) were acquired. Each FID contained 1024 data points at a sampling rate of 0.1 msec.

To measure proton T_2 , the standard Hahn spin-echo technique (Hahn 1950) was employed. For normal cartilage, the echo time (τ) was varied by 25 msec before com-

pression and 10 msec during compression. For the proteoglycan-depleted cartilage, τ was varied by 20 msec before compression and 8 msec during compression. Spectra at 30 time points were acquired for each T_2 measurement. For each time point, 200 FIDs were averaged to obtain a spectrum.

Although sodium exhibits bi-exponential T_1 in biological tissues, due to the small difference between the two T_1 s, it is difficult to measure each independently. Therefore, measurements of sodium spin lattice relaxation time constants, T_1 , were carried out using the same standard inversion-recovery methods used for proton. However, since the T_1 of sodium is several orders of magnitude shorter than that of proton, the inversion time was varied with a step time of 6 msec before compression and 3 msec during compression for both normal and proteoglycan-depleted cartilage specimens. Thirty inversion time points were acquired for each T_1 measurement; 200 FIDs were acquired and averaged for each inversion time. Each FID contained 1024 data points with sampling rate of 0.1msec.

The transverse relaxation of sodium is bi-exponential, and thus has two time constants: T_{2f} and T_{2s} . It has been shown, using triple quantum filtered spectra, that only the slow component, T_{2s} , is sensitive to compression (Reddy et al. 1996). Therefore we used the same standard Hahn spin-echo technique for the measurement of sodium transverse relaxation times as was used as in the case for proton transverse relaxation times. For normal cartilage, τ was varied by 4 msec before compression and 2 msec during compression. For proteoglycan-depleted cartilage, τ was varied by 3 msec before compression and 1 msec during compression. Spectra at 30 time points were acquired for each T_2 measurement. For each time point, 200 FIDs were averaged to obtain a spectrum.

7.2.4 Projection Image Acquisition

One-dimensional proton and sodium projection images, in a direction perpendicular to the articular surface, were acquired with the pulsed gradient spin echo pulse sequence (PGSE). The proton imaging parameters were TR = 1 sec, TE = 20 msec, NEX = 1. For sodium projections, the imaging parameters were TR = 100 msec, and TE = 3 msec, NEX = 800. The acquisitions of proton and sodium projection images were interleaved. The total acquisition time for one set of interleaved proton and sodium projection images was 81 seconds (one second for the proton projection image and 80 seconds for the sodium projection image). 100 interleaved projection images were collected for a total duration of approximately 135 minutes during cartilage compression.

7.3 Cartilage Sodium Content Mapping

7.3.1 Effects of Compression on MR Relaxation Times

Table 7.1 presents a summary of the data obtained regarding the effects of compression and PG depletion on cartilage proton (from chapter 4) and sodium MR relaxation times. The four inherent parameters: proton T_1 , proton T_2 , sodium T_1 , and sodium T_2 are delineated for the four physio-mechanical cartilage states: normal-uncompressed, normal-compressed, PG-depleted-uncompressed, and PG-depleted-compressed.

Each of the four parameters was evaluated, using a two-tailed t-test, to determine if PG depletion had a significant effect on any of the MR time constants. The resulting P-values are given in the last column of table 7.1. In the uncompressed state, the sodium MR time constants show a much stronger PG-depletion induced distinction than do the proton MR time constants. There is no evidence that proton- T_1 changes with PG-depletion, and

scarce evidence, if any, that proton- T_2 changes. On the other hand, both sodium- T_1 and sodium- T_2 increase with PG-depletion to a statistically significant extent.

Compressing cartilage provides a means for introducing a PG-depletion induced change in proton- T_2 . In the compressed state (using the same pressure), the proton- T_2 of the PG-depleted cartilage is shorter than that of normal cartilage. Furthermore, the change in proton- T_2 associated with compression is substantially more pronounced for PG-depleted cartilage than it is for normal cartilage.

The contribution of compression in distinguishing the effects of PG-depletion on sodium MR relaxation parameters is less pronounced; the change in sodium- T_2 , associated with compression, is similar for the normal and PG-depleted specimens.

The data also affords an evaluation of the changes in proton and sodium relaxation time constants associated with compression. To compliment the values displayed in table 7.1, the statistical significance of the compression associated changes in relaxation time are reported in table 7.2.

7.3.2 Effects of Compression on Sodium Concentration

Several one-dimensional sodium and proton projection images are shown in figures 7.3 and 7.4. The intensity of the images can be made approximately proportional to sodium ion and water volumetric concentrations by correcting for the effects of compression on MR relaxation times. This approximation is conducted by interpolating the MR relaxation characteristics during compression from the beginning and end of compression by considering relaxation times to be proportional to cartilage strain. This assumption has been validated to a reasonable extent in appendix B for proton MR relaxation times, and re-

mains speculative for the sodium ions. The image intensities are thus corrected for compression-induced relaxation using equation 7.8.

$$I' = \frac{I}{(1 - e^{-R_1 T_R}) e^{-R_2 TE}} \quad [7.8]$$

where I' is the corrected image intensity, I is the original image intensity, R_1 is the spin-lattice relaxation rate, R_2 is the spin-spin relaxation rate, T_R is the repetition time, and TE is the echo time.

Integrating the proton and sodium one-dimensional image projection data (corrected via equation 7.8) for each projection image (examples of which are given in figures 7.3 and 7.4) provides a calculation of sodium ion concentration in the cartilage fluid component. The result of this calculation is illustrated in figure 7.5.

Although figure 7.5 does not provide absolute sodium ion concentrations, the relative increase in sodium ion concentration for a given strain can be evaluated in terms of the theoretical predictions described in section 7.1. The information necessary for this evaluation is the initial cartilage fixed charge density. Spectrophotometric assays of cartilage fixed charge density, as described in the methods section of chapter 2, indicate that the cartilage specimens typically have fixed charge densities of approximately 200 mM. The expected sodium concentration can thus be derived from the multiplicative inverse of equation 7.7, which indicates that, for a fixed charge density of 200 mM, the initial cartilage sodium concentration within the fluid compartment is 291 mM. This sodium ion concentration is consistent with bovine patellar cartilage sodium concentration reported in the literature (Shapiro et al. 2000). The multiplicative inverse of equation 7.7 (which

provides the cartilage sodium interior/exterior sodium partition) under such conditions is illustrated in figure 7.5. The equilibrium predictions in figure 7.5 systematically deviate from the experimental results in that the experimental cartilage sodium concentration measurements are lower than the equilibrium condition during cartilage compression.

7.4 Discussion

7.4.1 *Multinuclear MR Relaxation Characteristics of Cartilage Compression*

As discussed in chapter 4, standard clinical proton imaging that employs basic T_1 and T_2 contrast mechanisms is unlikely to distinguish proteoglycan depletion in articular cartilage.

The results presented in this chapter support the notion that sodium imaging could have a substantial impact on cartilage evaluation in a clinical setting. We have demonstrated that both sodium T_1 and T_2 change significantly as a function of proteoglycan depletion whether or not the cartilage is in a compressed state. One caveat to this result is that sodium T_1 and T_2 both increase with proteoglycan depletion, and thus each may offset the effect of the other depending on the specifics of an imaging pulse sequence. The sodium relaxation parameters that we report can aid in the development of an optimal sodium pulse sequence for imaging cartilage proteoglycan loss.

Using sodium MR, one can indirectly infer changes in PG content, without resorting to compression. Two limitations of using sodium MRI are that it has a lower signal to noise ratio and that it requires stronger imaging gradients to resolve thin objects such as cartilage. However, the shorter T_1 of sodium can be exploited in signal averaging to improve the signal to noise ratio. High quality sodium images of articular cartilage have

been acquired in vivo in a research setting (Reddy et al. 1998), which lends promise that the technology can be moved toward clinical applications. This inference can then be related to cartilage softening and in turn to a non-compressive assessment of cartilage functionality.

7.4.2 Evaluation of the Osmotic Model's Mechanical Prediction

The strain vs. time curve for the cartilage specimen used to generate figure 7.5 is shown in figure 7.6. This plot was generated in the same manner as was done in chapter 5. The equilibrium strain, in response to the constant applied 0.69 MPa pressure, is approximately 0.35. According to the osmotic model developed here and illustrated in figure 7.2, a cartilage strain of 0.35 corresponds to a pressure of 0.64 MPa (assuming a 200 mM initial fixed charge density and 298 °K). In this case, the theoretical prediction of Donnan equilibria is consistent with the experimental data within 8%. This result indicates that the osmotic contribution is a dominant contributing factor to cartilage resistance to mechanical compression.

7.4.3 Evaluation of the Osmotic Model's Ionic Prediction

Figure 7.5 indicates a systematic error between predictions of the cartilage ionic equilibrium model and experimental results. The most likely reason for this deviation is that rate of ion diffusion is slower than the flow of ions associated with compressive extrusion. This explanation implies that without the diffusion of ions between the extruded fluid and the cartilage interior, the ion concentration of the extruded fluid would be identical to the ion concentration of fluid remaining within the cartilage volume. However,

substantial ion diffusion does occur; the effects of this diffusion are what give rise to the positive slope of the experimental data plotted in figure 7.5.

This hypothesis can be tested in several ways. The experiment can be conducted as a function of temperature. An increase or decrease in temperature would have a predictable effect on the rate of ion diffusion. The experimental equipment can be modified to increase the diffusive communication between the cartilage and the extruded fluid. It is plausible that the onset of inconsistency between the theoretical prediction and experimental results that occurs at a strain of 0.15, results from the onset of a lack of interaction between the cartilage specimen and its extruded fluid. Also, the experiment can be extended in time to observe whether, over an extended time period, the sodium concentration within the cartilage increases for a period of time after mechanical equilibrium is reached.

7.4.4 Cartilage Dynamics During Compression

The ionic model, as presented here, addresses mechanical equilibrium, but not dynamics. Cartilage mechanical dynamics are empirically presented in chapters 5 and 6. In chapter 6, where cartilage compressive dynamics are converted into cartilage permeability, a linear relationship between stress and strain was assumed. However, in the present chapter, the cartilage stress strain relationship is slightly non-linear.

The results of chapter 5 indicate that a selective reduction in fixed charge density substantially reduces compression time. Given that the cartilage collagen matrix remained mostly intact, it is likely that fixed charge density dominates permeability as a determinant of cartilage mechanical dynamics.

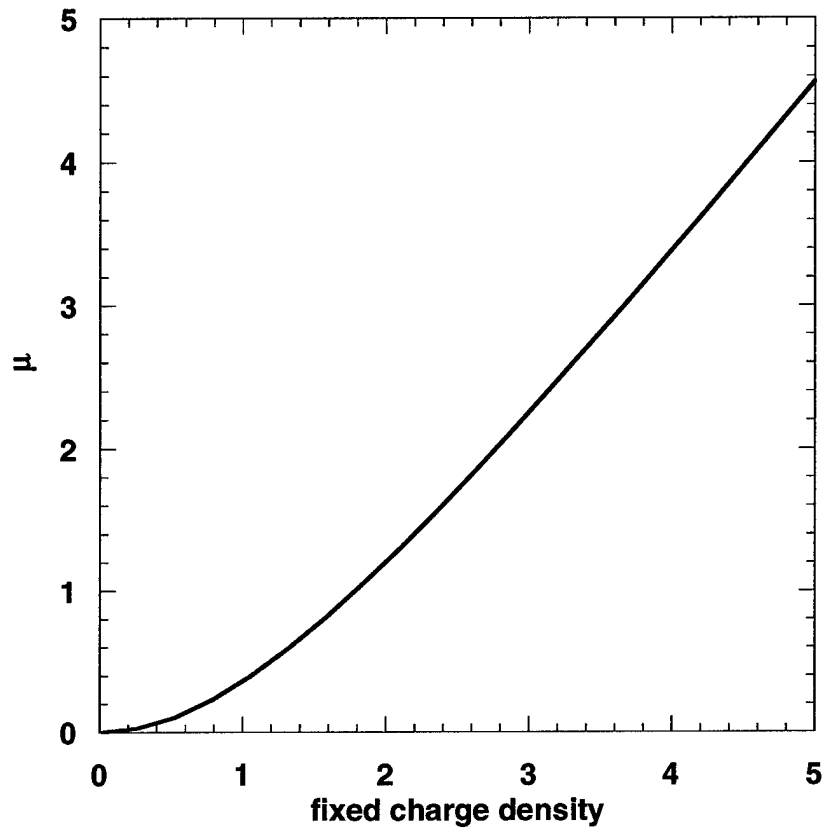


Figure 7.1 Cartilage osmotic strength as a function of cartilage fixed charge density. Cartilage osmotic strength, μ , is defined as the difference between the cartilage interior and exterior total solute concentrations. As with the convention described in chapter 2, μ and fixed charge density are normalized to the bathing sodium chloride concentration for algebraic simplicity. Using equation 7.1, and a bathing sodium chloride concentration of 137 mM at 298 °K, one unit of μ corresponds to a pressure of 0.34 MPa.

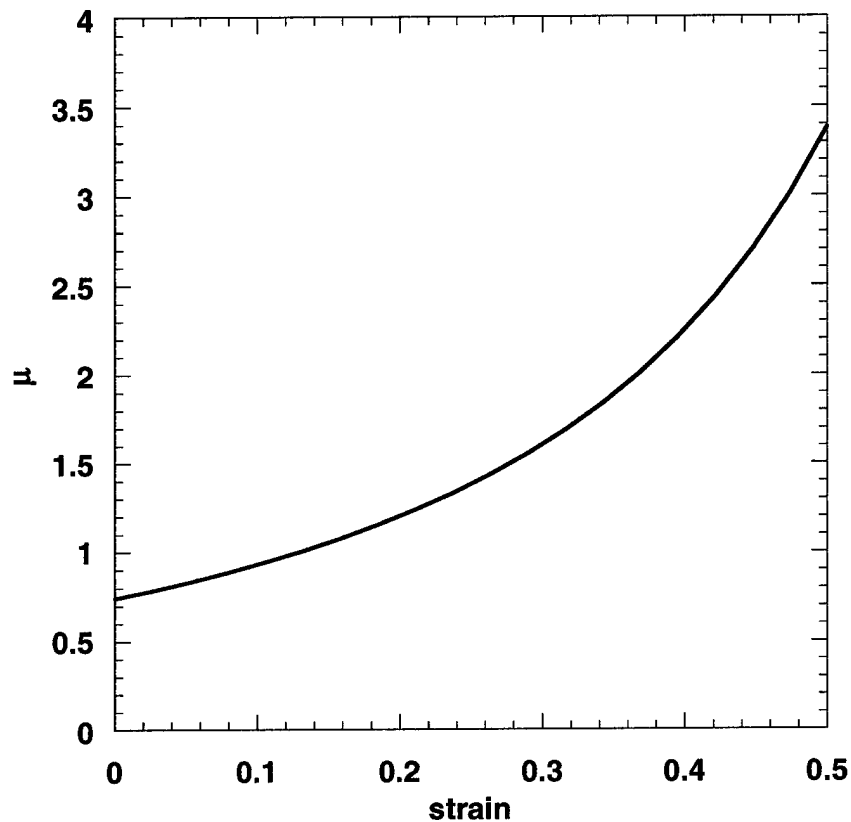


Figure 7.2 Cartilage osmotic strength as a function of compressive strain. The osmotic strength of cartilage, μ , as defined in the caption of figure 7.1, is plotted as a function of compressive strain. This example calculation employs a typical cartilage uncompressed fixed charge density of 200 mM. As described in the caption to figure 7.1, μ is normalized to the bathing sodium chloride concentration, and one μ unit corresponds to 0.34 MPa when the bathing sodium chloride concentration is 137 mM and the bathing temperature is 298°K.

| | <i>Full compression</i> | <i>Normal</i> | <i>SD</i> | <i>PG depleted</i> | <i>SD</i> | <i>P value</i> |
|------------------|-----------------------------|---------------|-----------|------------------------|-----------|--------------------|
| proton T1 (sec) | N | 1.54 | 0.06 | 1.52 | 0.09 | 0.658 |
| proton T1 (sec) | Y | 0.99 | 0.10 | 1.07 | 0.09 | 0.217 |
| (%change) | | -35.6 | 0.9 | -29.5 | 5.8 | 0.205 |
| proton T2 (msec) | N | 82.4 | 2.7 | 90.6 | 10.6 | 0.155 |
| proton T2 (msec) | Y | 38.8 | 2.6 | 29.6 | 6.2 | 0.028 |
| (%change) | | -52.9 | 2.5 | -67.1 | 6.8 | 0.007 |
| sodium T1 (msec) | N | 24.0 | 1.6 | 30.6 | 2.7 | 0.003 |
| sodium T1 (msec) | Y | 14.8 | 1.9 | 24.8 | 3.4 | 0.001 |
| (%change) | | -38.2 | 8.2 | -19.1 | 7.0 | 0.004 |
| sodium T2 (msec) | N | 18.0 | 3.2 | 25.7 | 3.8 | 0.008 |
| sodium T2 (msec) | Y | 11.2 | 0.8 | 15.5 | 2.1 | 0.009 |
| (%change) | | -36.6 | 8.6 | -39.3 | 4.1 | 0.548 |

Table 7.1 Sodium and proton relaxation parameters. Relaxation times are given for proton T₁, proton T₂, sodium T₁, and sodium T₂ for cartilage in the normal and mechanically compressed state. A comparison is drawn between these parameters for normal cartilage and cartilage that has been enzymatically treated to induce proteoglycan depletion. Standard deviations of all relaxation times are given in the adjacent columns labeled "SD" In each case, five cartilage specimens were used. The relaxation times reported are the corresponding means. In addition to relaxation times, the per-cent change between the normal and compressed state is given. For each normal vs. PG-depleted comparison, the results of a two-tailed t-test is given in the rightmost column labeled "P"; the value in this column represents the probability that the normal and PG-depleted values could have arisen from sampling a single population.

| <i>Nuclei</i> | <i>Normal/degraded</i> | <i>Relaxation time constant</i> | <i>P value</i> |
|---------------|------------------------|-------------------------------------|----------------|
| Proton | Normal | T ₁ | 1.60E-05 |
| | Normal | T ₂ | 5.00E-09 |
| | Degraded | T ₁ | 4.00E-05 |
| | Degraded | T ₂ | 3.20E-05 |
| Sodium | Normal | T ₁ | 3.50E-05 |
| | Normal | T ₂ | 0.0056 |
| | Degraded | T ₁ | 0.018 |
| | Degraded | T ₂ | 0.002 |

Table 7.2. The statistical significance of the change in relaxation time constants associated with compression.

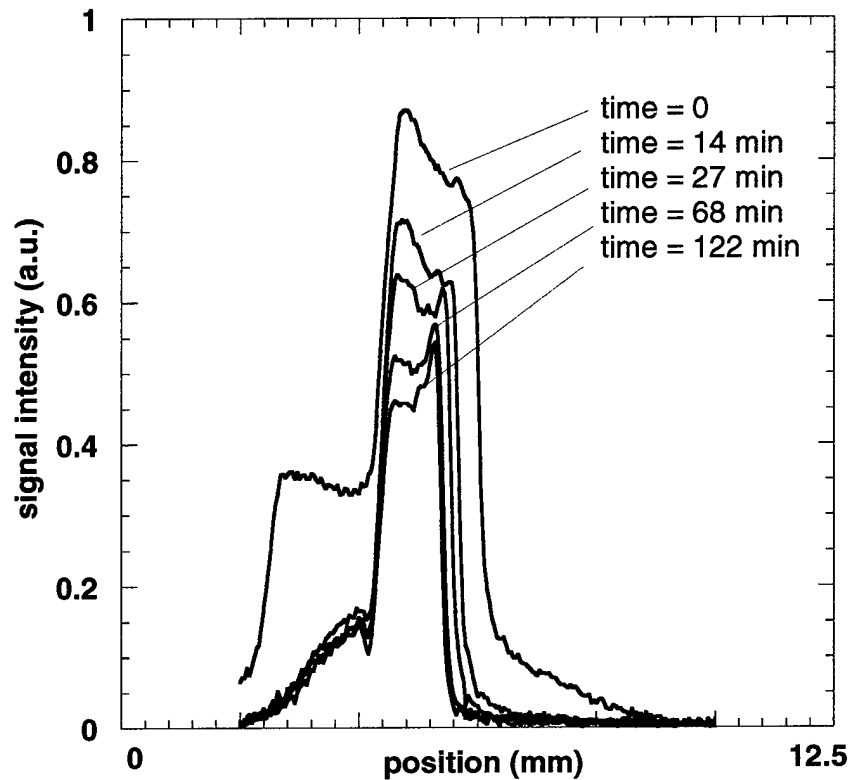


Figure 7.3. One-dimensional 90° - 180° spin echo proton projection images of a cartilage specimen. Five projections are shown at various times after onset of pressure application. The compressive force is from right to left against the stationary glass filter. The left-hand slope of the projection corresponds to the articular surface of the cartilage specimen. The right hand slope of the projection corresponds to the cartilage-bone boundary.

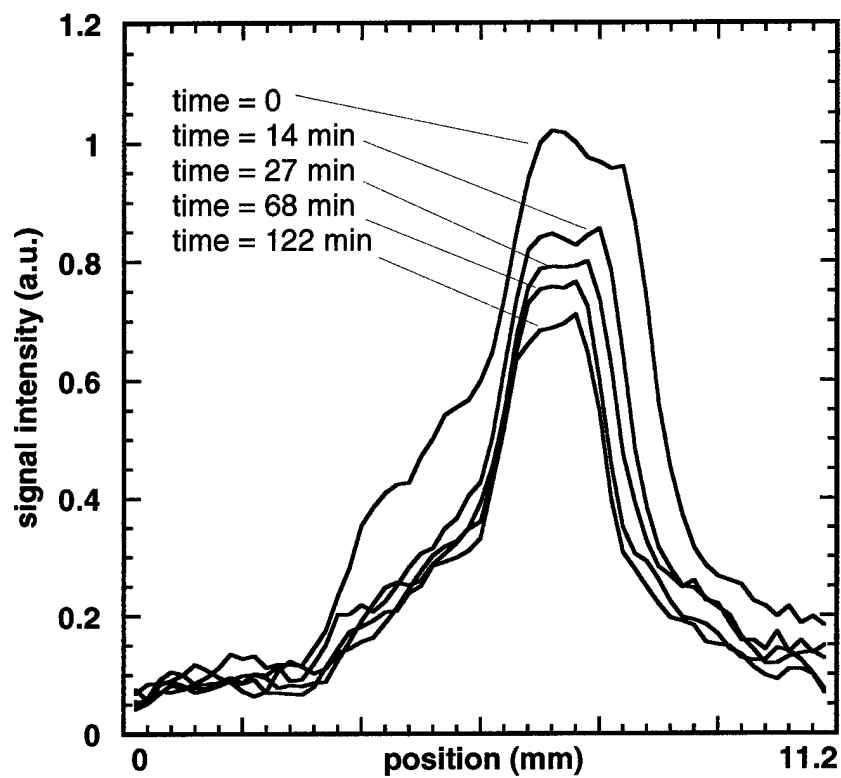


Figure 7.4. One-dimensional spin-echo sodium projection images of a cartilage specimen. Five projections are shown at indicated times after the onset of pressure application. The specimen orientation is identical to that of figure 7.3.

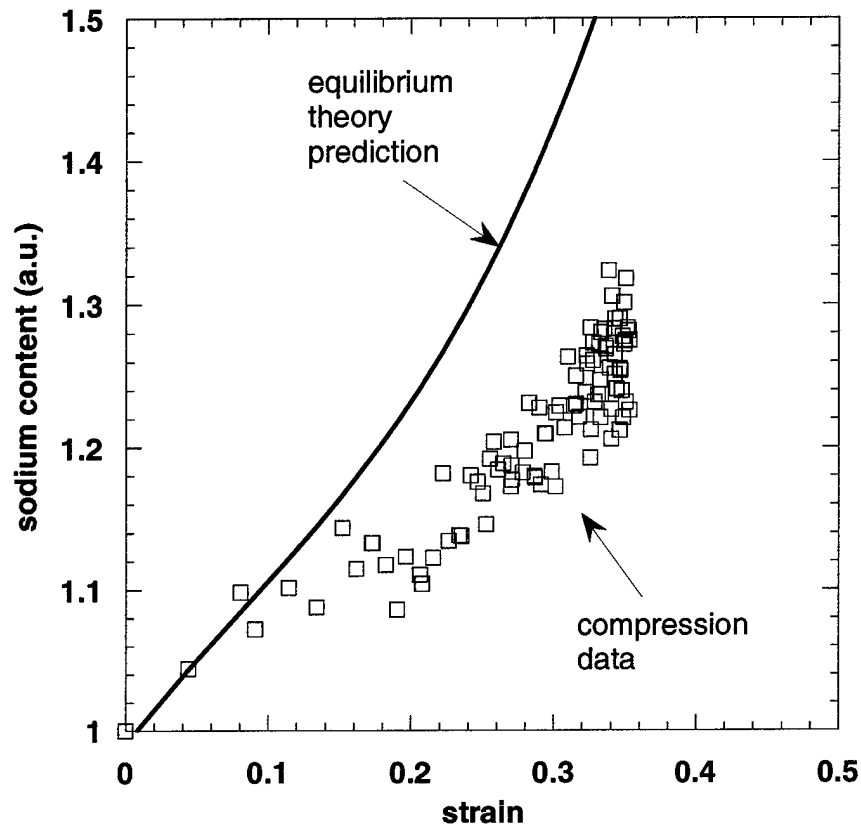


Figure 7.5. Theoretical prediction and experimental measurements of cartilage sodium content in the fluid compartment as a function of mechanical compression. The solid line indicates the theoretical prediction described by equation 7.7. The squares represent experimental data acquired during the interleaved sodium/proton projection images. Sodium content is normalized to the initial cartilage sodium concentration in the fluid compartment. Note that this normalization convention is different than that used for figures 7.1 and 7.2.

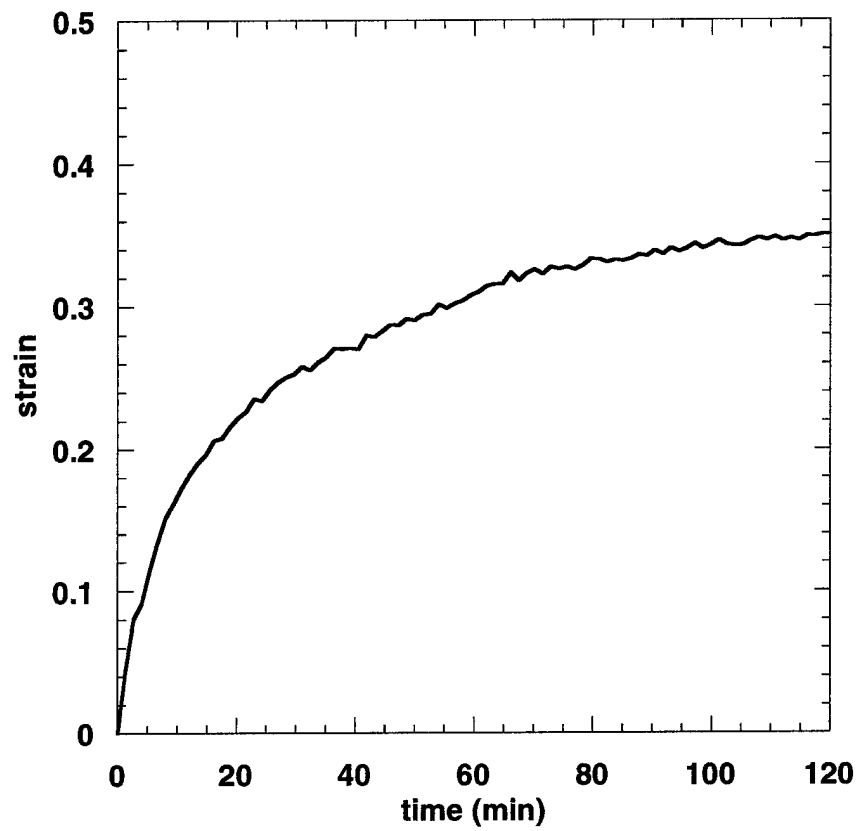


Figure 7.6. Time dependant strain of cartilage compression during a constant compressive force.

APPENDIX A

MAGNETIC RESONANCE IMAGING OF UNCONFINED CARTILAGE COMPRESSION

A.1 Introduction

The compression experiments of the earlier chapters describe cartilage compression as a unidirectional event. In these in-vitro experiments, the cartilage specimens were confined laterally such that no cartilage expansion could occur during compression. This experimental constraint was introduced to simplify the deformation analysis by restricting stress and strain to one dimension. However, physiological cartilage deformations are not likely to behave in this manner. It is therefore also useful to study cartilage compression during scenarios where cartilage specimens are not laterally constrained.

A.2 Methods

Bovine articular cartilage specimens were obtained from bovine patella as described in section 2.4.2. These cartilage disks were cut with a diameter of 5 mm. Cartilage compression was performed as a step function in time, with a pressure of 0.69 MPa. The pressure cell was the same, and thus, the diameter of each cartilage specimens was smaller than the inner diameter of the pressure cell.

Images were obtained in a 4 Tesla field, using a commercially available clinical spectrometer (GE Signa). The cartilage specimens were oriented in the cartilage compression device such that the cartilage articular surface was parallel to the main magnetic field. Body gradients were employed for imaging; the field of view was 4.0 cm. Slice selective two-dimensional 90° - 180° spin echo images were acquired along a plane perpen-

dicular to the axis of the main magnetic field. Slice thickness was 2.0 mm and oriented along a diameter of the cartilage disk. Images were collected with a 192 by 256 acquisition matrix. Slice selective images were acquired prior to cartilage specimen compression, and at the following time points after compression was applied: 1 min, 2 min, 3 min, 4 min, 5 min, 6 min, 7 min, 8 min, 9 min, 10 min, 11 min, 12 min, 13 min, 18 min, 23 min, 28 min, 33 min, 38 min, and 43 min. Frequency encoding was in the direction perpendicular to the cartilage specimen articular surface. The spin echo images employed an echo time of 20 msec, and a repetition time of 300 msec.

The experimental protocol was repeated for a proteoglycan depleted articular cartilage specimen. This specimen was obtained in the same manner as discussed above, except that it was incubated with 1.0 mg/mL bovine pancreatic trypsin for three hours on ice then for one hour at 37°C. The imaging protocol was the same as above, except that the acquisition matrix was 256 by 256 and images were obtained at the following time points: 0.0 min, 1.4 min, 2.8 min, 4.5 min, 5.9 min, 7.4 min, 8.9 min, 10.3 min, 11.8 min, 13.2 min, 14.5 min, 16.0 min, 17.5 min, 18.9 min, 20.4 min, 21.8 min, 23.1 min, 24.5 min, 26.0 min, 27.4 min, 28.9 min, 30.3 min, 31.7 min, 33.0 min, and 34.5 min.

A.3 Results

Figure A.1 shows the two-dimensional slice selective images of a representative cartilage specimen prior to and during compression. Cartilage compression over time is demonstrated. The serial images indicate that the cartilage specimen bulges out slightly in the radial direction during compression.

The simplest analysis of this compressive event is two dimensional, represented by the direction perpendicular to the cartilage articular surface (*longitudinal*) and the direction radial to the cylindrical cartilage disk (*radial*). Longitudinal strain as a function of time was calculated by computing the linear interpolated full width at half maxima of serial one-dimensional profile images generated by summing the image arrays along the horizontal direction. The result of this analysis, for the present case, is illustrated in figure A.2. As in chapter 6 (figure 6.2), the longitudinal strain data did not fit a single time constant exponential decay well, but did adequately fit a two time constant exponential decay. The longitudinal strain in the *unconfined* compression experiment for a normal cartilage specimen was similar that of a proteoglycan depleted cartilage specimen in a *confined* compression. This is apparent by a comparison of figures 6.2 and A.2.

Radial strain as a function of time was calculated in the same manner as longitudinal strain with the distinction that the image arrays were summed along the vertical direction. The result of this calculation is illustrated in figure A.3 where radial strain is plotted as a function of compression duration. Also shown in figure A.3 is the least squares best fit of a single time constant exponential decay. By comparison of figure A.3 with A.2, the relative rates of radial expansion is demonstrably higher than that of longitudinal compression. Cartilage softening as a result of proteoglycan depletion is demonstrated in figure A.4. Figure A.5 indicates an equilibrium strain of approximately 0.7, which is substantially higher than the equilibrium strain reached for cartilage specimens when compressed with the same pressure but in a confined geometry (see chapter 6). In addition, by inspection of figures 6.2 and A.5, the compressive time constant is demonstrated to be relatively shorter. Figure A.6 shows radial strain as a function of time during

compression. The radial expansion shown in figure A.6 is not significantly different than that shown for the normal cartilage specimen shown in figure A.3.

A.4 Discussion

It has been previously hypothesized that, during unconfined compression, an articular cartilage specimen will quickly expand in a radial direction while slowly compress in the longitudinal direction (Armstrong et al. 1984). Our experiments confirm this hypothesis while quantifying the phenomenon. It is worth noting that the description of radial expansion exhibited by figure A.3 is merely a first approximation of the compressive event. The description makes the assumption that the radial expansion of an articular cartilage disk during compression is uniform with regard to depth from the articular surface. However, inspection of the images in figure A.3 indicates that this is not the case. The cartilage specimen tends to bulge out non-uniformly.

Neither confined or unconfined compression of articular cartilage specimens accurately mimic normal cartilage physiology. We have encountered evidence that intact articular cartilage exists in a state of substantial residual lateral strain. This evidence is that when a cylindrical articular cartilage specimen is removed from bone, the resulting cylindrical specimen has a diameter approximately 5% larger than that of the core drill. Articular cartilage thus has a natural propensity to rapidly expand upon removal from bone. Since there is no water lost during this expansion, the cartilage volume must remain constant and thus the cartilage specimens must contract in the longitudinal direction upon removal from bone. This aspect of cartilage physiology likely provides an additional source of stiffness in-vivo.

A comparison of the unconfined compression of normal and proteoglycan depleted cartilage specimens indicates that the longitudinal compressive modulus of articular cartilage is compromised by proteoglycan depletion while the associated radial expansion is relatively independent of proteoglycan depletion. This contrast indicates that the initial radial expansion of articular cartilage when undergoing a longitudinal compressive pressure is not mediated by an osmotic resistance. It is likely that the early radial expansion (and associated early longitudinal contraction) results from a quick rearrangement of the cartilage matrix and does not involve substantial fluid extrusion.

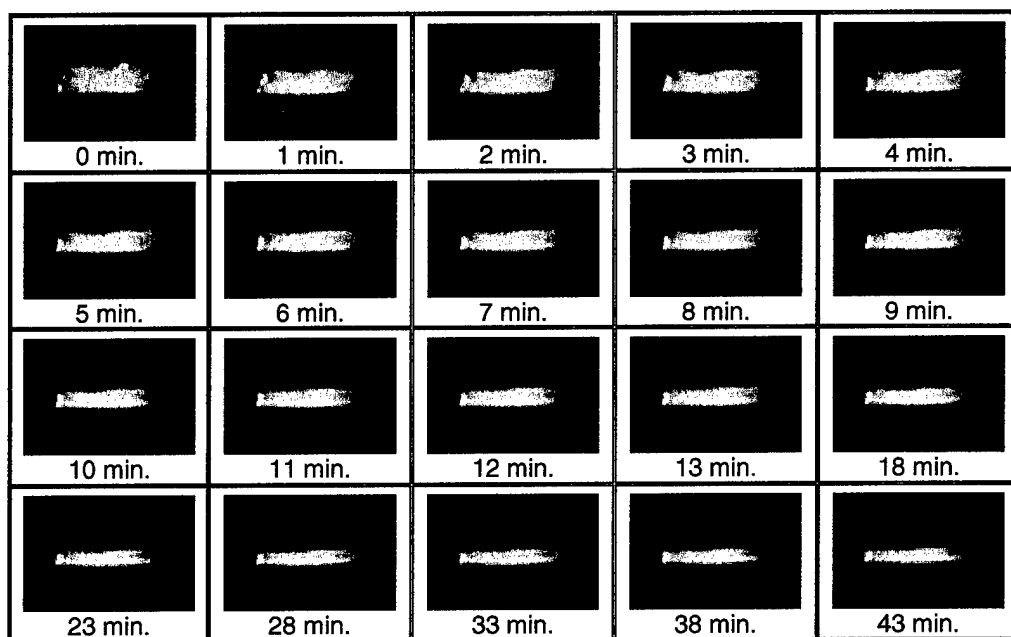


Figure A.1 Serial slice selective spin echo images of a cartilage specimen during compression. Compression duration progresses from the top left image across the rows to the bottom right image. Final compression duration is 43 minutes. The cartilage specimen is oriented in the MR compatible compression device such that the cartilage articular surface is in contact with the porous glass filter. Cartilage compression is imparted by a ceramic piston acting from the top of each image pushing down. The porous glass filter is present in each image as diffuse region of increased signal intensity beneath each cartilage image. Notice that the glass filter has a larger diameter than the cartilage specimen, which indicates that the cartilage specimen had room to expand radially during compression.

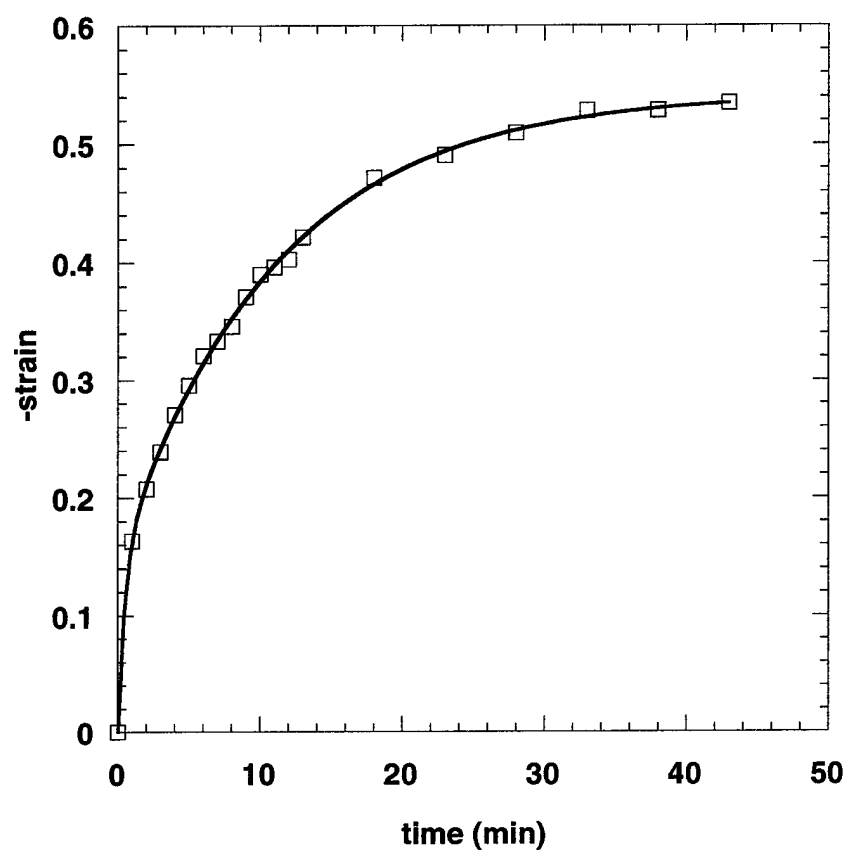


Figure A.2 Longitudinal strain of normal cartilage specimen during unconfined compression. The solid line represents a two time constant fit to the experimental data.

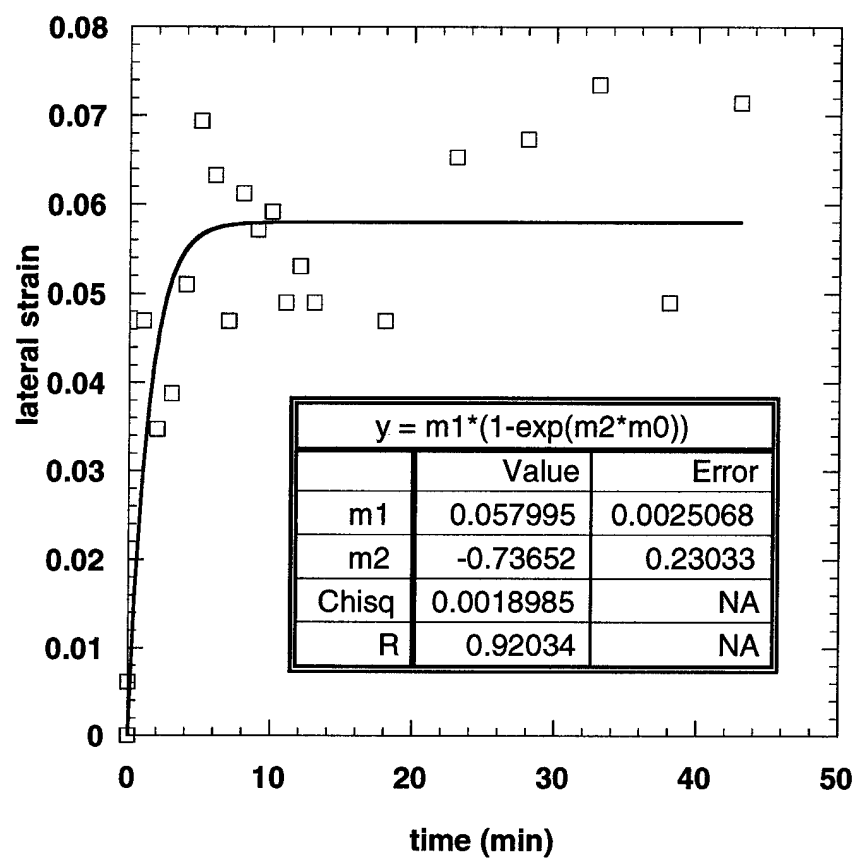


Figure A.3 Radial strain of the normal cartilage specimen during unconfined compression. The solid line represents a single time constant fit to the experimental data. The fit parameters are indicated in the figure.

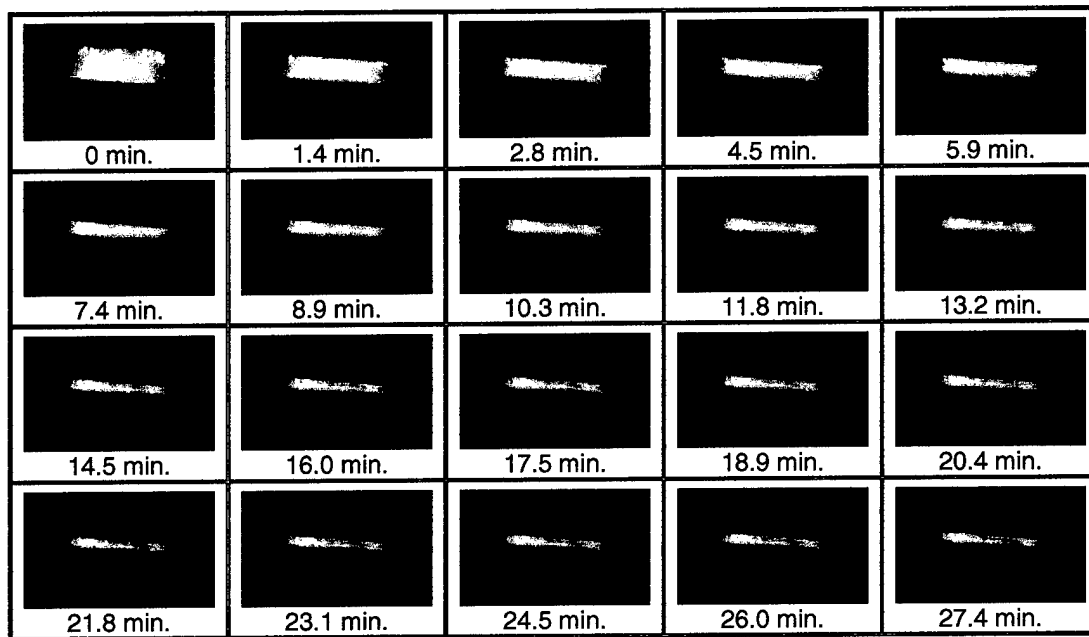


Figure A.4 Serial slice selective spin echo images of a cartilage specimen during compression. Images sequence is similar to that of figure 8.1.

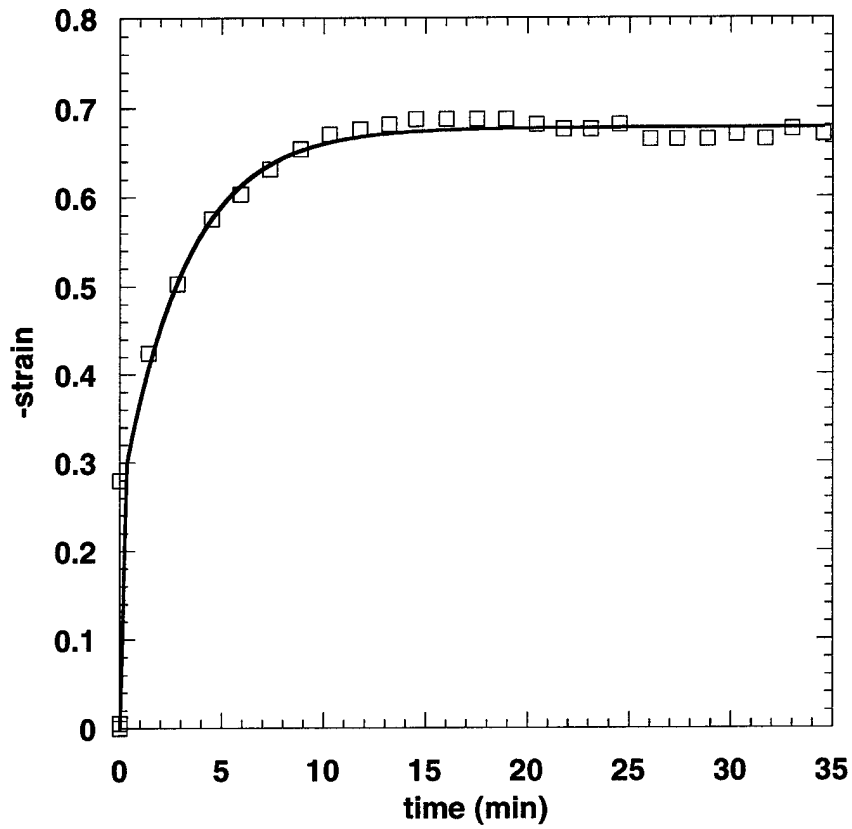


Figure A.5 Longitudinal cartilage strain of the proteoglycan depleted cartilage specimen during unconfined compression. The solid line represents a two time constant fit to the experimental data.

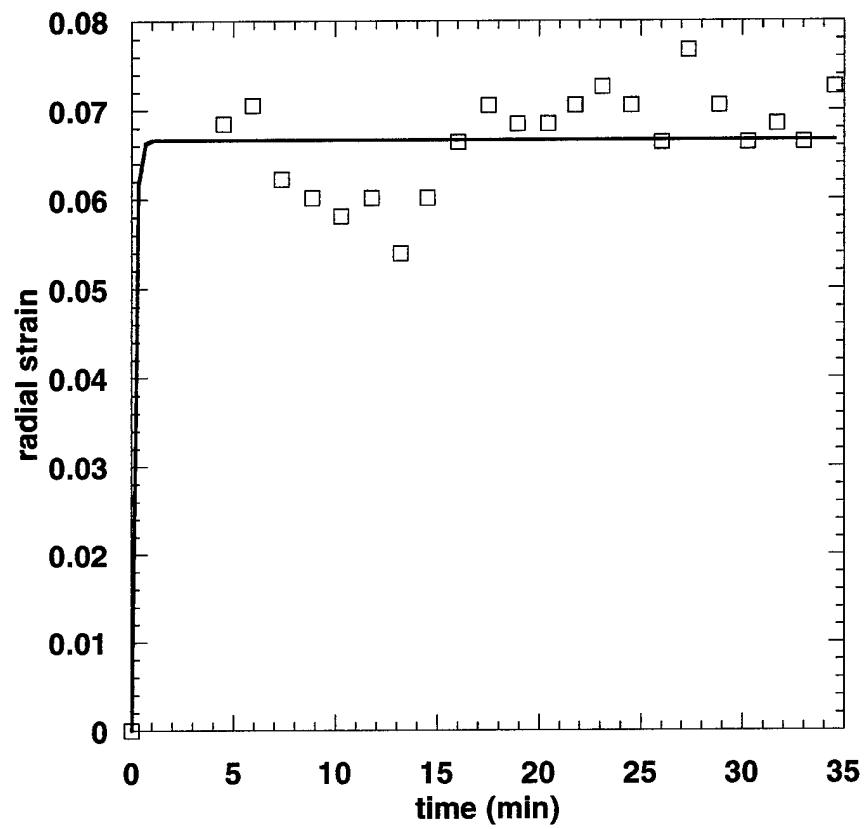


Figure A.6 Radial strain of the proteoglycan depleted cartilage specimen during unconfined compression.

APPENDIX B

CARTILAGE MRI STRAIN MAPPING DURING COMPRESSION

B.1 Introduction

Purely mechanical studies of articular cartilage compression typically involve describing articular cartilage as a relatively homogeneous medium. During a compressive event, a description is usually given for the strain of the entire specimen without an explicit description of which regions (or layers) exhibit the bulk of the compression. The reason for this lack of spatial specificity is that it is difficult to isolate which regions of a cartilage specimen are experiencing strain. One method for overcoming this challenge is to shave an articular cartilage specimen in a direction parallel to the cartilage articular surface, then perform mechanical experiments on each layer individually. This approach has been realized experimentally in permeability studies (Maroudas et al. 1976). There are two inherent limitations to this approach: articular cartilage is a thin material that can only be practically shaved into a limited finite number of layers, and articular cartilage is rarely (if ever) flat and thus presents a challenge to physically slicing it into parallel layers.

The experiment presented in this chapter is a novel way to quantitatively to approach cartilage compression with a depth resolved analysis. The technique employs magnetic resonance imaging to collect depth dependant one-dimensional images of articular cartilage during compression (much in the same fashion as was described in chapter 6). However, in the present protocol, spin echo images were repeated collected with a

range of echo times. This data collection permitted a depth dependant calculation of the cartilage spin-spin relaxation time (T_2). A knowledge of T_2 with depth dependant resolution is then employed to describe the relative depth dependant cartilage solid content distribution at each time point during compression. This solid content distribution, in combination with the notion that only fluid leaves cartilage during compression, can then provide a mapping of solid content redistribution.

B.2 Methods

B.2.1 Overall Protocol

Cylindrical cartilage discs were acquired from the flat surface of juvenile bovine patellea. Each disc was placed into the MR compatible nonmagnetic pressure cell (presented in chapter 3) that compresses cartilage specimens in one dimension against a porous glass filter. Each disc was then compressed with a 0.69 MPa pressure for a period of one hour. During the compression, spin-spin relaxation time constant (T_2) maps of the cartilage specimens were generated at a frequency of one map per minute. The T_2 maps were one dimensional along an axis perpendicular to the cartilage articular surface. This protocol provided cartilage T_2 measurements as a function of depth from the articular surface with a one minute temporal resolution during compression.

B.2.2 Cartilage Specimen Preparation

Cartilage specimens were obtained from juvenile bovine patellae obtained within six hours post mortem then stored on ice. 8.0 mm cartilage disks were removed from the flat region of the bone and stored in phosphate buffered saline (PBS) at 0 °C.

B.2.3 T₂ Projection Mapping

One-dimensional T₂ projection mapping was conducted by acquiring one-dimensional 90°-180° spin-echo image projections along a direction perpendicular to the articular surface, then fitting these projection images to equation B.1,

$$I = Ae^{-kT_E} + C \quad [B.1]$$

where I is the image intensity of a given pixel, k is $1/T_2$, T_E is the echo time, and C is an arbitrary constant. Imaging was conducted in a 2 Tesla field. The cartilage specimen was oriented such that the articular surface was parallel to main magnetic field. A solenoid rf coil was used. The rf pulses were not slice selective; thus the projection images represented the entire cartilage specimen collapsed onto a line perpendicular to the surface. No phase encoding was employed. Frequency encoding was perpendicular to the articular surface. The magnetic field gradient was supplied by a custom built gradient set capable of providing 8 gauss/cm.

One T₂ projection map was acquired each minute. Each T₂ projection was calculated from seven projection images having the following echo times: 20 msec, 40 msec, 60 msec, 80 msec, 100 msec, 120 msec, 140 msec, 160 msec, and 180 msec. A five second delay existed between each projection image acquisition.

B.2.4 Cartilage Compression

Cartilage compression was conducted with the non-magnetic pressure cell described in chapter 3. The pressure cell employed a pneumatic method for pressing a ceramic piston onto the cartilage which was positioned against a porous glass filter. The filter was connected to a drain which permitted cartilage extruded cartilage fluid to exit

the cell during compression. A continuous pressure of 100 psi (0.69 MPa) was employed for a duration of 120 min. During each compressive event, T_2 projection maps were acquired at a frequency of one projection map per minute.

B.3 Results

B.3.1 T_2 map calculations

Onedimensional apparent T_2 maps were calculated from the one dimensional 90°-180° spin-echo projection images. The projection images, acquired with several echo times, were fit to equation B.2

$$I = Ae^{\frac{TE}{T_2}} + B, \quad [B.2]$$

where I is image intensity, A is a parameter proportional to the MR visible proton content (in addition to being related to the particular imaging conditions), T_E is the echo time, and B is an offset associated with image noise. Figure B.1 shows an example series of projection images; figure B.2 illustrates the associated T_2 map. Figure B.3 illustrates articular cartilage T_2 projections for the same cartilage specimen at two different times during compression. Sixty similar T_2 projections per specimen were available for analysis temporally separated by one-minute intervals.

B.3.2 Cartilage Water Content Calculations

Since the elapsed time between projection image acquisitions was approximately five times that of previously measured values of cartilage spin-lattice relaxation times (T_1) (Kaufman et. al., 1999), it is assumed that T_1 effects on signal intensity are negligible. The major specimen dependant contributions to signal intensity are thus proton den-

sity and apparent spin-spin relaxation time (T_2) effects. It is assumed that the major proton signal is associated with cartilage water content since the protons associated with the major cartilage biopolymers will likely have short relaxation times which inhibit visibility under the imaging protocol used. Water content within a multiplicative factor was thus obtained by rearrangement of equation B.2. Figure B.4 illustrates the results of an example water content calculation associated with the data from figures B.1 and B.2. Relative water content before and after one hour of a continuous mechanical pressure of 0.69 MPa is illustrated in figure B.5.

B.3.3 Cartilage Longitudinal Strain Calculations

Cartilage thickness was determined as the full width at half maximum of the one-dimensional cartilage projection images as validated previously (Kaufman et. al., 1999). Linear interpolation between adjacent pixels was used routinely since the position of intensity at half maximum often occurred between pixel boundaries in the one-dimensional images. Cartilage longitudinal strain was calculated as the change in thickness of the cartilage specimen divided by the cartilage specimen's original thickness. A typical cartilage specimen strain vs. time curve for a constant compressive force of 0.69 MPa is shown in figure B.6. The cartilage specimen used to generate figure B.6 was the same as in figures B.1-B.5.

The boundaries generated while determining cartilage longitudinal strain were employed when calculating the total water volume of a cartilage specimen during compression. The total cartilage specimen water volume was calculated as the integral of cartilage water volume over the area bound by the cartilage specimen thickness boundaries.

Linear interpolation was used when calculating the water volume contributions of the signal portions associated with the cartilage specimen edges, which, in general, did not correspond exactly to pixel boundaries. Figure B.7 illustrated relative total cartilage water content as a function of time during compression. Figure B.8 illustrates relative total cartilage water content as a function of longitudinal strain.

The boundaries used to calculate longitudinal strain, and relative total water content were also used to calculate aggregate cartilage T_2 ; the aggregate value of T_2 is defined here as simply the average of the T_2 values at each pixel within the cartilage boundaries. Figure B.9 illustrates aggregate T_2 as a function of time. Figure B.10 illustrates the relationship between aggregate T_2 and cartilage longitudinal strain. Figure B.11 illustrates the relationship between aggregate T_2 and cartilage volume. Figure B.12 illustrates the relationship between aggregate T_2 and relative cartilage water content.

B.3.4 Lateral expansion of Articular Cartilage

During the compressive event, the cartilage specimen experiences a reduction in volume by the extrusion of a portion of its fluid content as indicated by figure B.7. The cartilage specimen also exhibits a radial expansion perpendicular to the direction of compression. Figure B.12 exhibits a framework of terms useful for describing the compressive event. In this figure, r is the original radius of the cartilage specimen, Δr is the radial increase associated with lateral expansion, and e is the strain in the longitudinal direction as defined as the fractional change in cartilage thickness. For algebraic simplicity, all dimensions are normalized to the original thickness of the cartilage specimen. The original cartilage volume, V_0 , is thus

$$V_0 = \pi r^2, \quad [\text{B.3}]$$

and the volume occupied by the cartilage solid component, V_s , is thus

$$V_s = s\pi r^2. \quad [\text{B.4}]$$

The total cartilage volume, V_T , as a function of longitudinal (e) and lateral (Δr) strain is defined geometrically as

$$V_T(e, \Delta r) = (1-e)\pi(r + \Delta r)^2, \quad [\text{B.5}]$$

and thus water content, W , is described by

$$W = (1-e)\pi(r + \Delta r)^2 - s\pi r^2. \quad [\text{B.6}]$$

Since our experimental protocol indirectly measured water content and longitudinal strain as a function of time, it is useful to rearrange equation B.5 and express lateral strain as the dependant variable

$$\Delta r = \sqrt{\frac{W + s\pi r^2}{(1-e)\pi}} - r. \quad [\text{B.7}]$$

The calculations employed in figures B.6 and B.7 can be substituted in the right side of equation B.7 to generate a prediction of the radial expansion function of a cartilage specimen during a constant compressive event. With the measured 20% volume fraction of the cartilage solid component, cartilage radial expansion is calculated as a function of compression time and is illustrated in figure B.13. Radial expansion was measured directly during separate cartilage compression experiments at 4 Tesla, where two-dimensional images were acquired at a one-minute resolution. A comparison of the cartilage radial expansion prediction from the one-dimensional projection images to the radial expansion measurements via two-dimensional imaging is shown in figure B.14.

The theoretical prediction is comparable to the experimental results, however, the prediction has a temporally broad depression centered at 35 minutes after pressure onset, which is not seen experimentally.

B.3.5 Cartilage Strain Mapping During Compression

The results for longitudinal compression and radial expansion as a function of time provide a temporal description of cartilage compression in terms of overall specimen morphology. This description combined with the water content estimations described in figures B.4, B.5, and B.7 can provide estimates of the cartilage compressive behavior as a function of distance from the cartilage articular surface. The water content normalization of figures B.4, B.5, B.7, and B.8 is based on equation B.5, where the initial cartilage water content must be consistent with the conditions of zero initial strain

$$W(e = 0, \Delta r = 0) = (1 - s)\pi r^2. \quad [\text{B.8}]$$

The initial cartilage measurements for the example shown are that the initial cartilage solid volume content was 20% ($s=0.2$) and that the initial cartilage diameter was 4.67 times larger than its thickness ($r=2.335$). Given that the cartilage geometry predicts total cartilage volume as a function of time, the water content calculations can be converted into a description of cartilage solid content flow. The solid content flow can then be used to describe longitudinal strain mapping of the cartilage specimen during compression. Each pixel in the one-dimensional projection description of water content corresponds to a virtual cylindrical slice of the cartilage specimen. If the cartilage thickness is initially divided into N pixels, the volume associated with a given pixel is

$$v_T = \frac{\pi(r + \Delta r)^2}{N}, \quad [\text{B.9}]$$

where v_T is the total volume represented by a given pixel. Substitution of equation B.7 into equation B.9 yields an explicit expression for pixel volume as a function of longitudinal strain and total cartilage water content

$$v_T = \frac{W + s\pi r^2}{N(1 - e)}. \quad [\text{B.10}]$$

The corresponding water content for each slice can be calculated from the water content maps, given that the composite water content map containing all time points is normalized to be consistent with equation B.6 and B.8. The water content maps, thus normalized, when subtracted from the total volume maps predicted by equation B.10 on an individual pixel basis provide maps of solid content for each time point. The solid content map for the same example specimen is shown in figure B.14.

An understanding of the movement of solid content provides a way to determine the compressive behavior of individual cartilage regions. Computational demarcations were determined in a direction perpendicular to the cartilage articular surface. The solid content corresponding to the initial cartilage one-dimensional projection image was divided into ten contiguous evenly distributed regions. Total solid content corresponding to each individual region was calculated by integrating the initial ($t = 0$) solid content map individually over the demarcated spatial regions. Thus, the discrete total solid content per region function was determined. This process can be expressed symbolically by figure B.15 and equations B.11-B.14.

$$\Phi(x) = \sum_{i=a}^b \phi(i) \quad [\text{B.11}]$$

$$a = (x-1) \frac{N}{10} \quad [\text{B.12}]$$

$$b = x \frac{N}{10} - 1 \quad [\text{B.13}]$$

$$x \in \{1, 2, \dots, 10\} \quad [\text{B.14}]$$

where $\Phi(x)$ is total solid content for each demarcated unit, x is the demarcated unit index, ϕ is the solid content for each image pixel, a and b are the pixel limits for each demarcated unit, and N is the total number of pixels across the cartilage specimen.

The discrete function $\Phi(x)$ provides a means for strain mapping given the following three assumptions: cartilage volume is primarily decreased during compression by a loss of fluid content, cartilage retains a constant total solid content during compression, the longitudinal ordering of cartilage solid content remains constant during compression. In other words, it is assumed that temporal transformations of cartilage solid content functions are homeomorphic. This assumption indicates the algorithm for mapping cartilage longitudinal strain shown in figure B.16, where $P(x)$ is the pixel position function of the cartilage computational demarcations. This algorithm, when applied to all time points during compression, provides $P(x,t)$, a description of cartilage position movements as a function of time.

$P(x,t)$ can, in turn, be converted into a spatial mapping of cartilage longitudinal strain during compression

$$e_x(t) = \frac{P(x,t) - P(x-1,t)}{P(x,0) - P(x-1,0)}, \quad [\text{B.15}]$$

where $e_x(t)$ indicates the longitudinal strain of the x^{th} computational demarcation (region x) at time t . A representative $e_x(t)$ is shown in figure B.17. Each function approximates an exponential decay. Longitudinal compressive modulus and compressive time constant can be obtained by fitting each $e_x(t)$ to equation B.16

$$e_x(t) = E_x \left(1 - \exp\left(\frac{-t}{\tau_x}\right) \right) \quad [\text{B.16}]$$

where E_x is the compressive modulus of region x , and τ_x is the compressive time constant of region x . The results of fitting the experimental results to each $e_x(t)$ are illustrated in figures B.18 and B.19.

B.4 Discussion

In this experiment, the compressive properties of an articular cartilage specimen have been deduced as a function of distance from the articular surface. The results indicate that a relatively soft and compliant region of cartilage exists between the highly calcified region of cartilage adjacent to bone and the cartilage central region. That a soft region of cartilage lies between the bone interface and the main cartilage body makes sense in retrospect, but was an unexpected result.

Traditionally, the softness distribution of cartilage has been described as a gradual increase in compressive modulus in a direction from the articular surface to the cartilage bone interface. This description has been supported by an experiment where microscopic imaging of chondrocyte nuclei was conducted during compression (Schinagl et al. 1996).

The primary distinction between the experiment conducted by Schinagl et al. and the experiment presented in this chapter is that of lateral expansion. If an experimental protocol does not permit fluid extrusion in a radial direction, then all cartilage fluid must exit the cartilage via the articular surface. In other words, if cartilage fluid is retained laterally, for fluid to leave the cartilage region near the bone interface, it must push its way through the entire cartilage depth. In this way, the cartilage specimen as a whole can be no more permeable to fluid than the permeability of the articular surface.

The experimental protocol of this chapter permits cartilage fluid to exit the cartilage specimen at the lateral surface as well as permits cartilage radial expansion during longitudinal compression. The results thus indicate that, during unconfined compression, cartilage fluid preferentially leaves the specimen laterally. It is difficult to interpret the implications of this behavior since, as discussed in chapter 8, cartilage is likely to exist in-vivo with a substantial negative radial residual strain. Furthermore, in a in-vivo situation, cartilage fluid ultimately must exit some portion of the articular surface during a compressive event that incurs a total cartilage volume reduction.

The strength of the technique presented here is that the present study can be extended to an in-vivo setting. Novel methods for fast three-dimensional T_2 mapping in conjunction with exercise induced in-vivo cartilage compression/expansion experiments can be combined with the present analysis to obtain a true three-dimension continuum description of cartilage compression in-vivo.

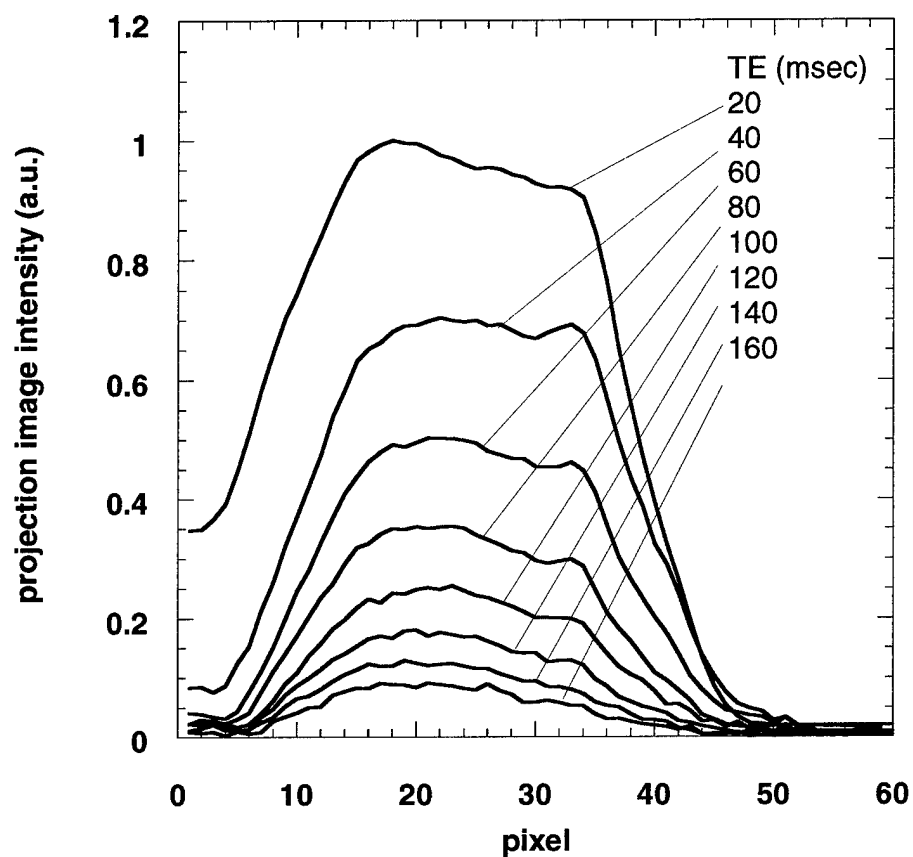


Figure B.1. One-dimensional example projection images. The direction of the projection images is such that pixel 0 corresponds to the direction of the cartilage articular surface and pixel 60 corresponds to the direction of the cartilage bone interface. These projection images correspond to the cartilage specimen several minutes after compression onset. Each projection is of a 90° - 180° spin-echo pulse sequence with a range of echo times as indicated in the figure.

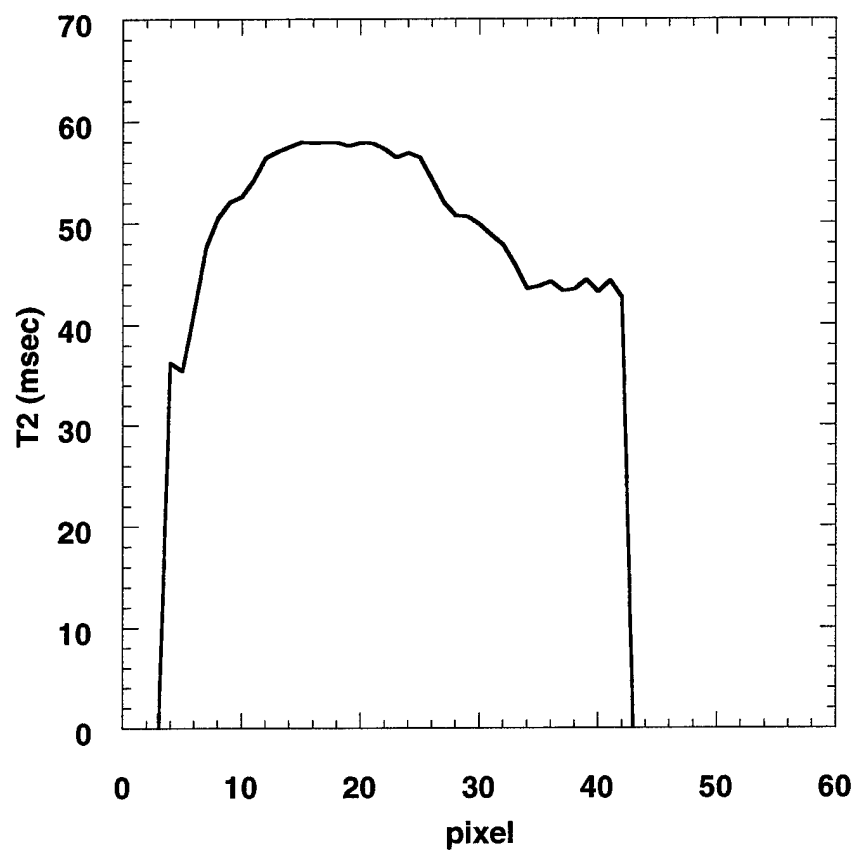


Figure B.2. One dimensional T_2 projection map. This T_2 projection map was calculated from the projection images shown in figure B.1. At each pixel, Image data a best numerical fit was obtained to equation B.1.

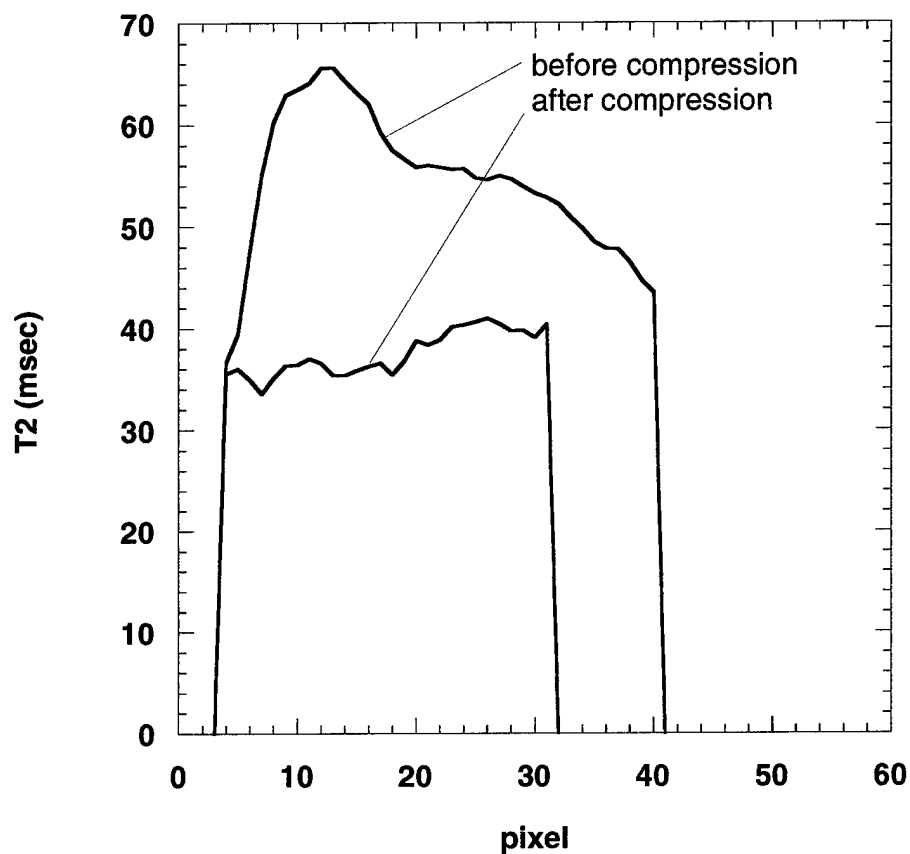


Figure B.3. T_2 before and after compression. Shown are two one-dimensional T_2 projections. The projections represent two limiting position of the cartilage during compression: the cartilage T_2 projection prior to compression, and the cartilage T_2 projection after one hour of continuously applied pressure of 0.69 MPa.

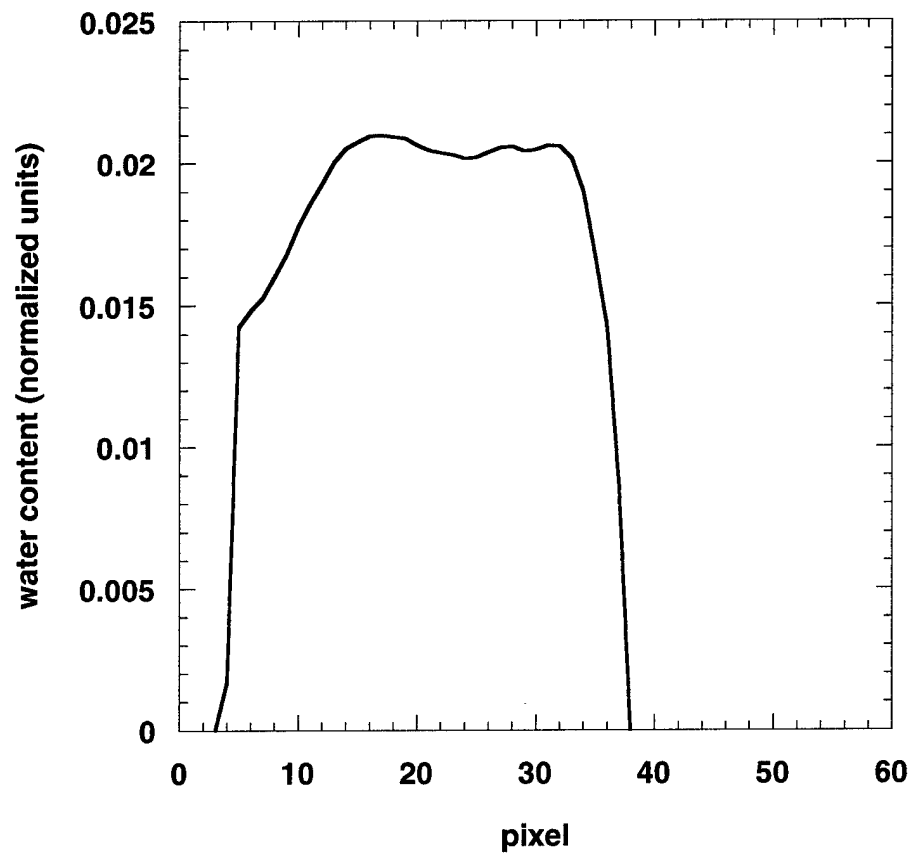


Figure B.4. One dimensional water content map of the cartilage specimen after several minutes of compression. The articular surface is the left portion of the map; the calcified cartilage region is the right portion of the map. the cartilage specimen is being compressed against a porous Pyrex filter from left to right.

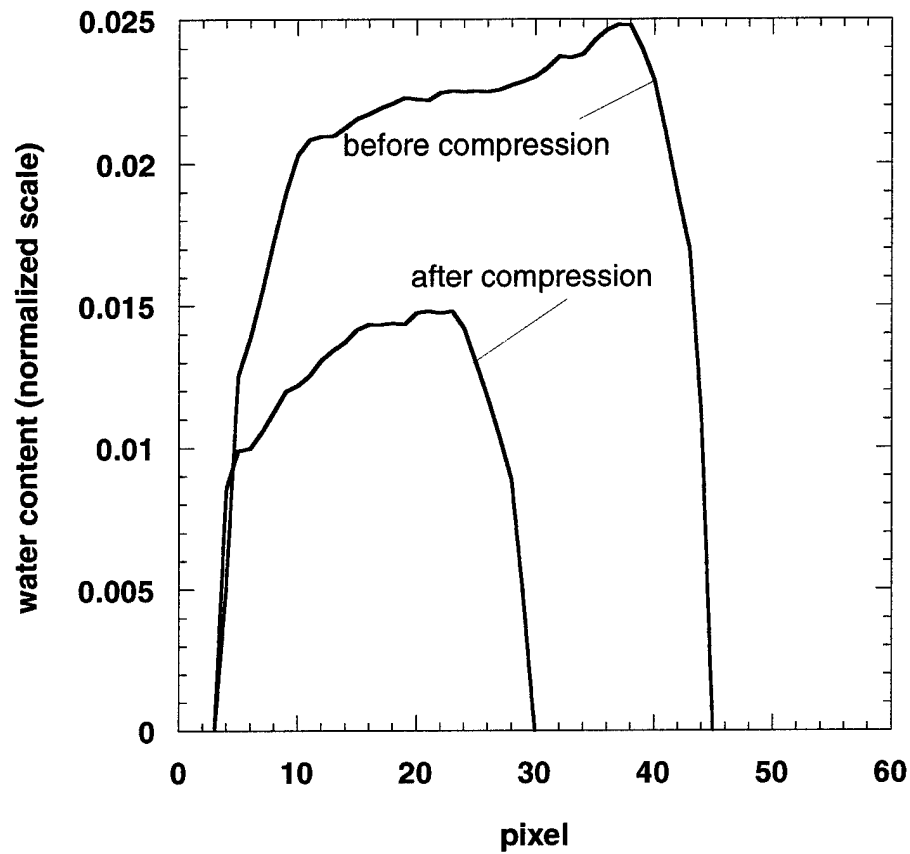


Figure B.5. Water content before and after compression. The water content projections shown here are similar to the water content projection shown in figure B.4. These projections, however, illustrate the water content states before and after one hour of a continuous 0.69 MPa longitudinal pressure. The time points presented are the same as those illustrated in figure B.3.

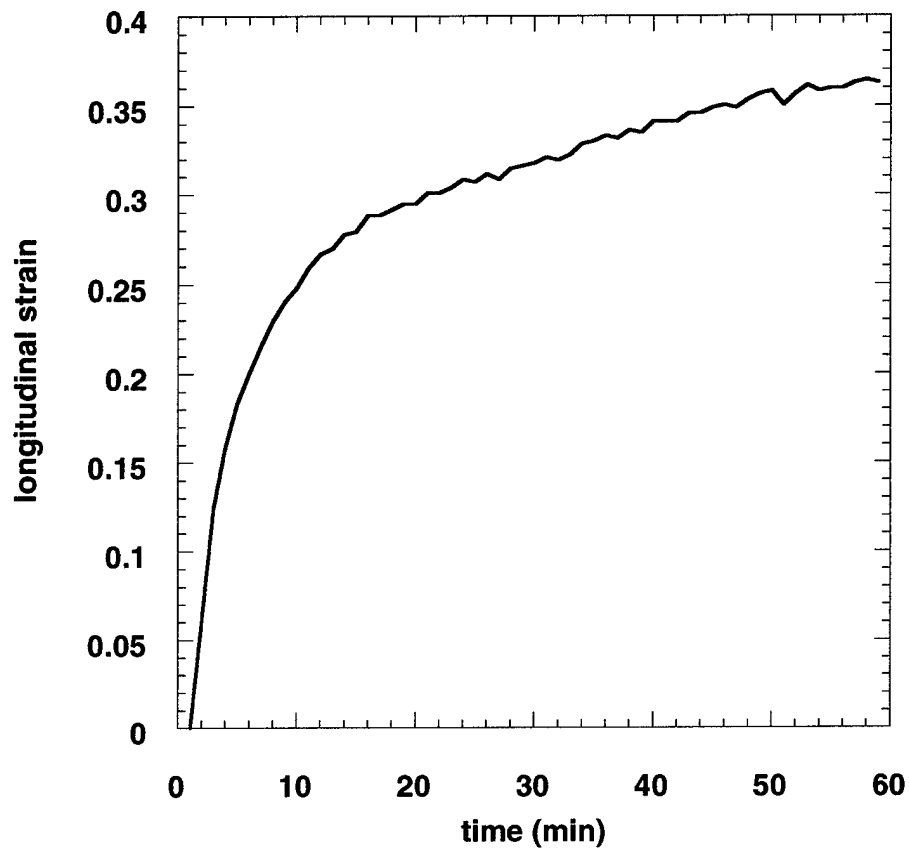


Figure B.6. Longitudinal strain as a function of time. Longitudinal strain of the cartilage specimen is presented as a function of duration after a continuous 0.69 MPa longitudinal pressure. The temporal resolution is one-minute intervals. Strain was calculated from the one-dimensional projection images and is defined here as the change in cartilage longitudinal thickness divided by the original cartilage longitudinal thickness.

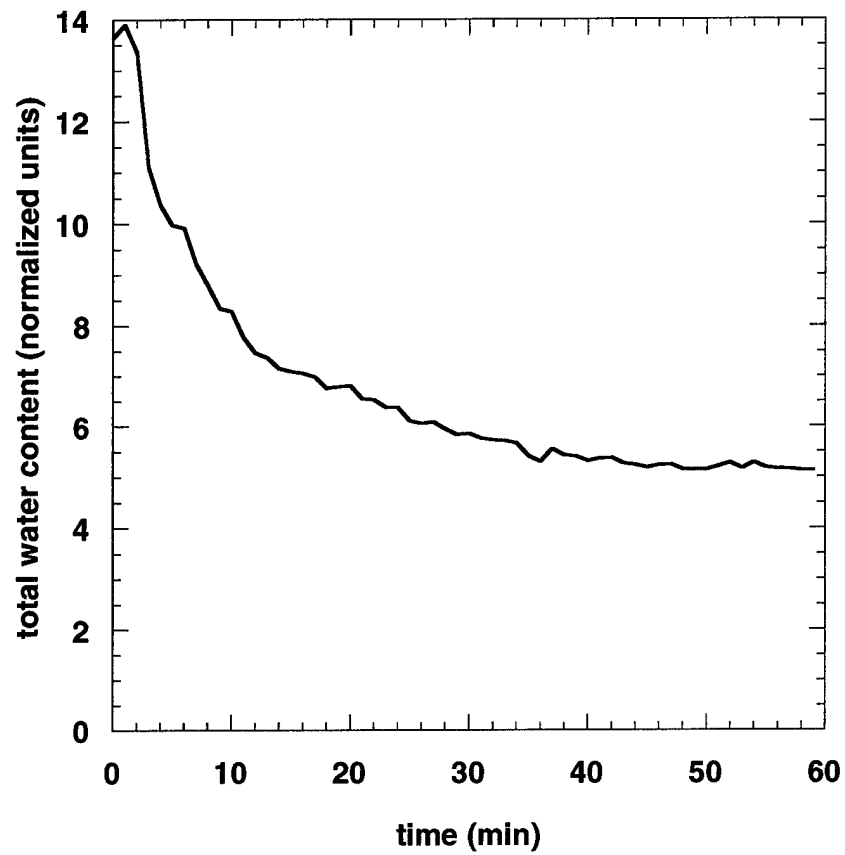


Figure B.7. Relative total water content as a function of time. Water content calculations shown were calculated as integrations of the one dimensional water content maps over the cartilage thickness. The integrations were normalized to maintain consistency with equation 7.

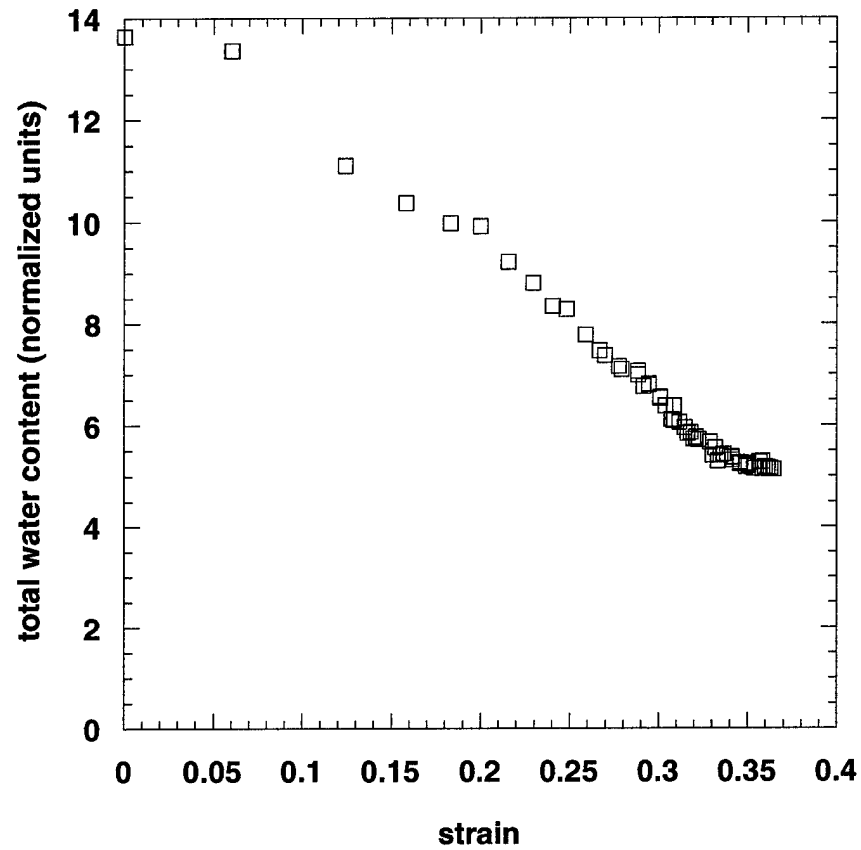


Figure B.8. Total water content as a function of longitudinal strain. Water was calculated as in figure B.7, and is presented as a function of cartilage longitudinal strain calculated as described in the legend of figure B.6.

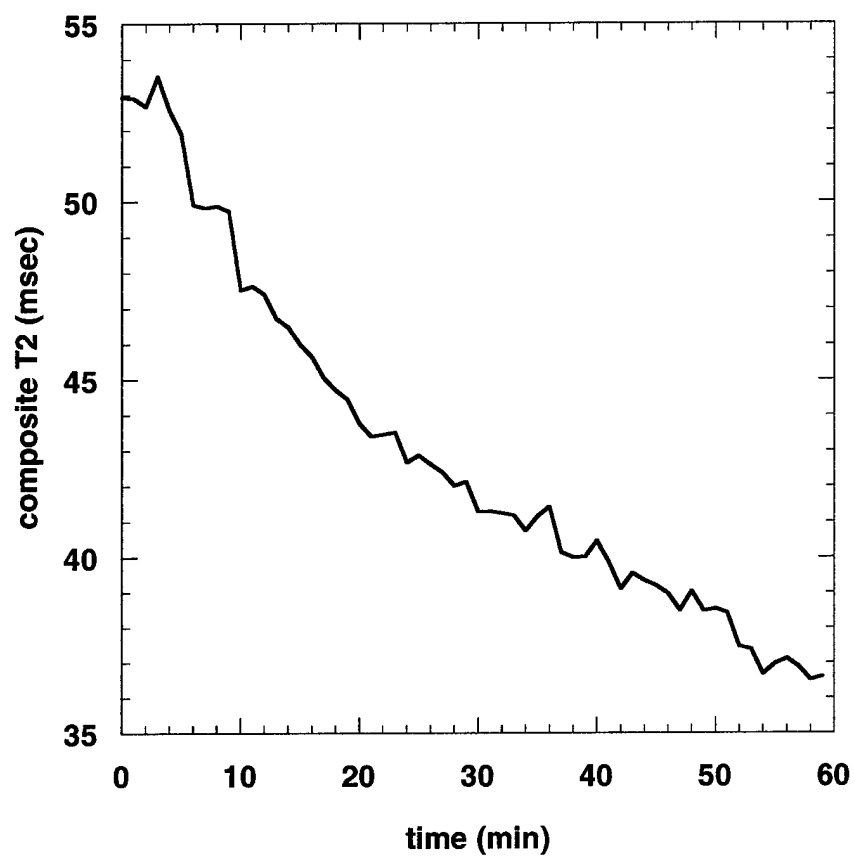


Figure B.9. Composite T_2 as a function of time. T_2 of the cartilage specimen presented as the average of T_2 pixel values of the one-dimensional T_2 projections illustrated in figure B.3.

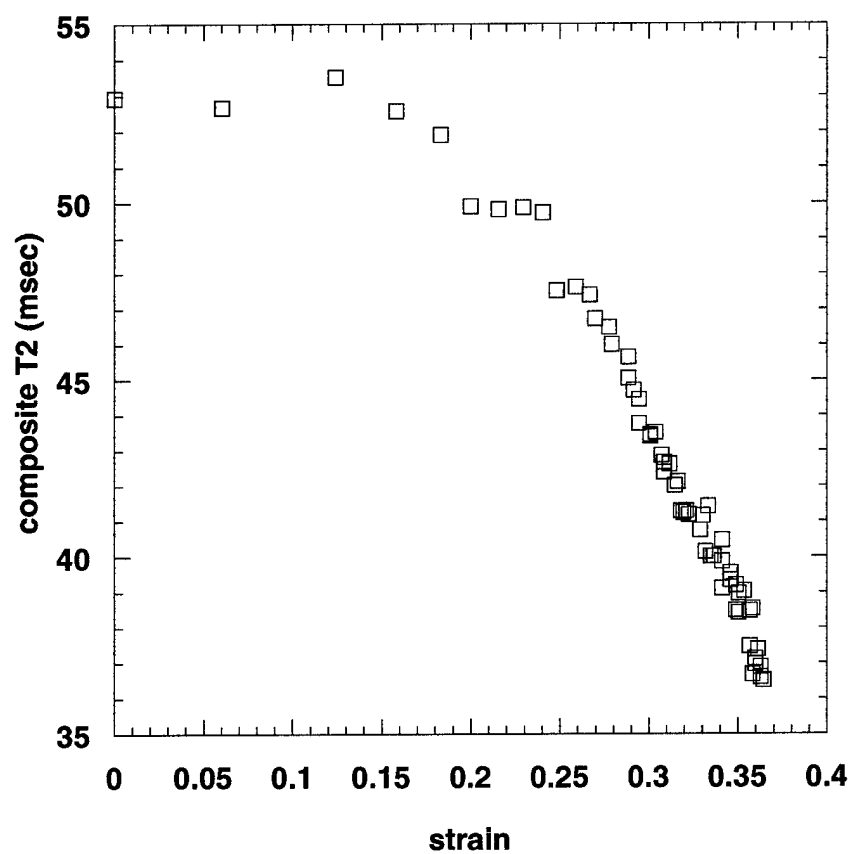


Figure B.10. Composite T_2 as a function of longitudinal strain. Composite T_2 was calculated as described in the legend of figure B.9; longitudinal strain was calculated as described in the legend of figure B.6.

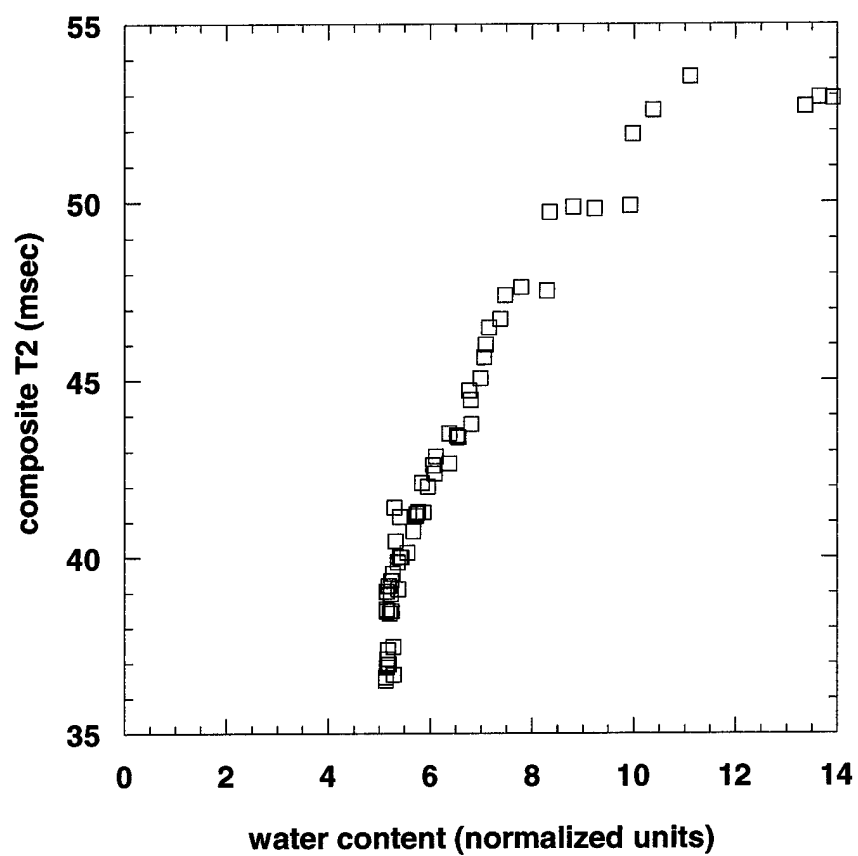


Figure B.11. Composite T_2 as a function of relative total water content. Composite T_2 was calculated as described in the legend of figure B.9; relative total water content was calculated as described in the legend of figure B.7.

Side View of Cartilage Disk

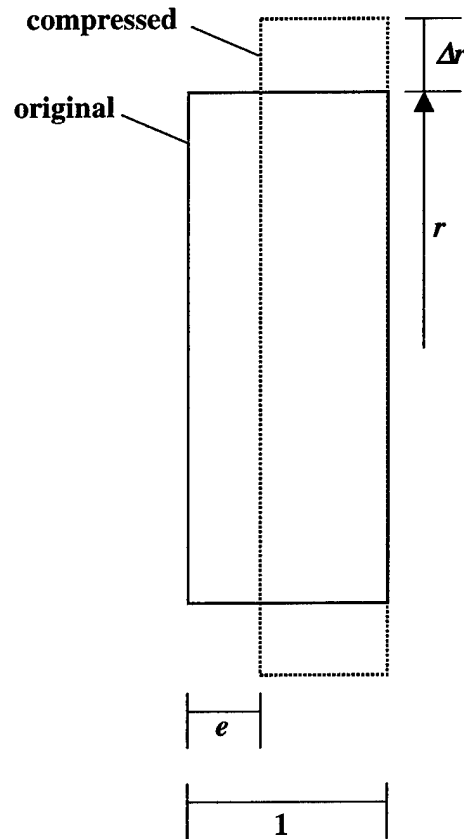


Figure B.12. Side view of articular cartilage disk before and during compression. The solid line denotes the original position of the cartilage disk; the dashed line denotes the compressed state. For algebraic simplicity, the physical dimensions of the cartilage disk are normalized to the original thickness. The original radius of the cartilage disk is r . During compression, lateral (radial) expansion occurs by Δr . The longitudinal compression is e , which as a result of the normalization convention, is also the longitudinal strain.

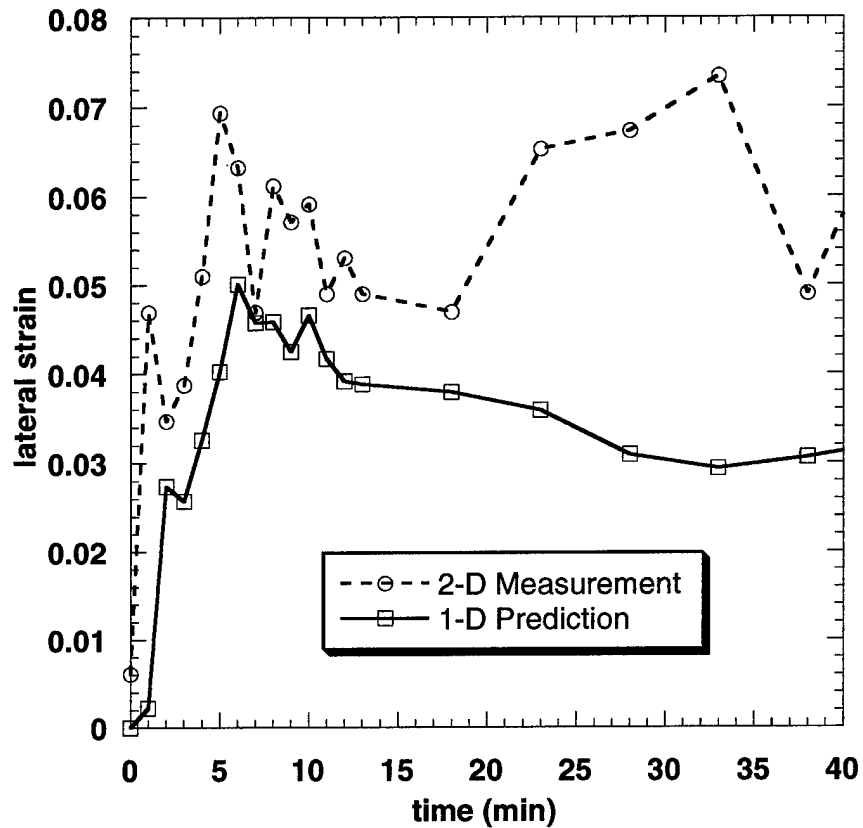


Figure B.13. Cartilage specimen radial expansion. The solid line with square markers represents the prediction of the one dimension compression results using equation B.6. For comparison, the results of a separate compression experiments are shown (dashed line) where cartilage lateral expansion was directly measure via two dimensional imaging.

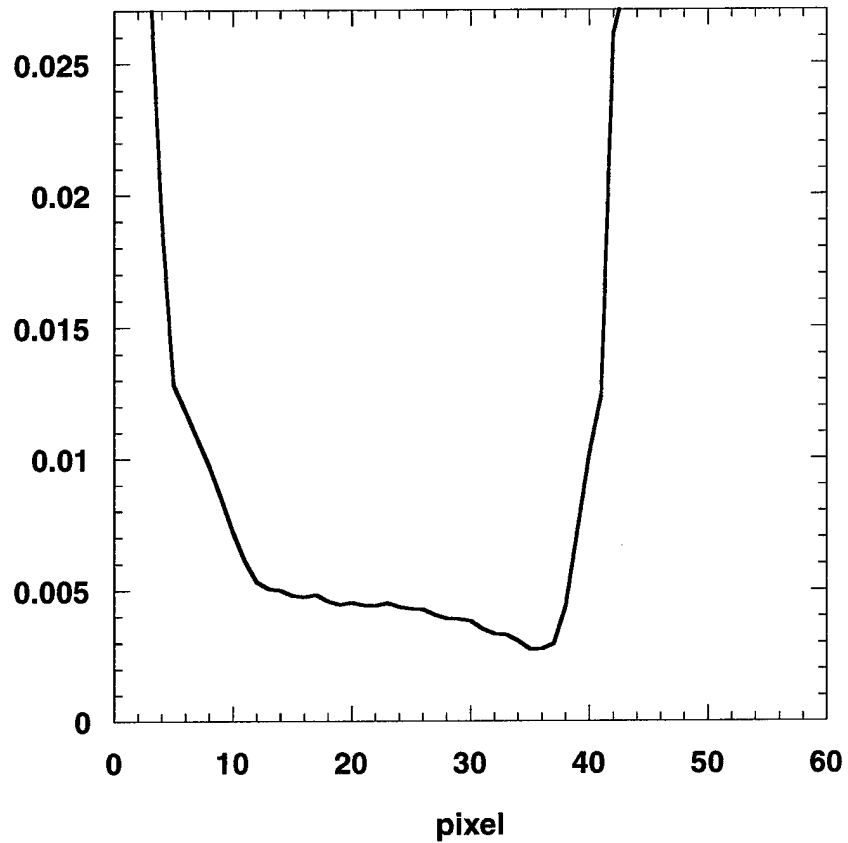


Figure B.14. Volumetric solid content of the cartilage specimen. The solid content was calculated from the relationship (expressed in equation B.9) between derivations of cartilage volume and water content. Normalized was conducted to maintain consistency with equation B.7.

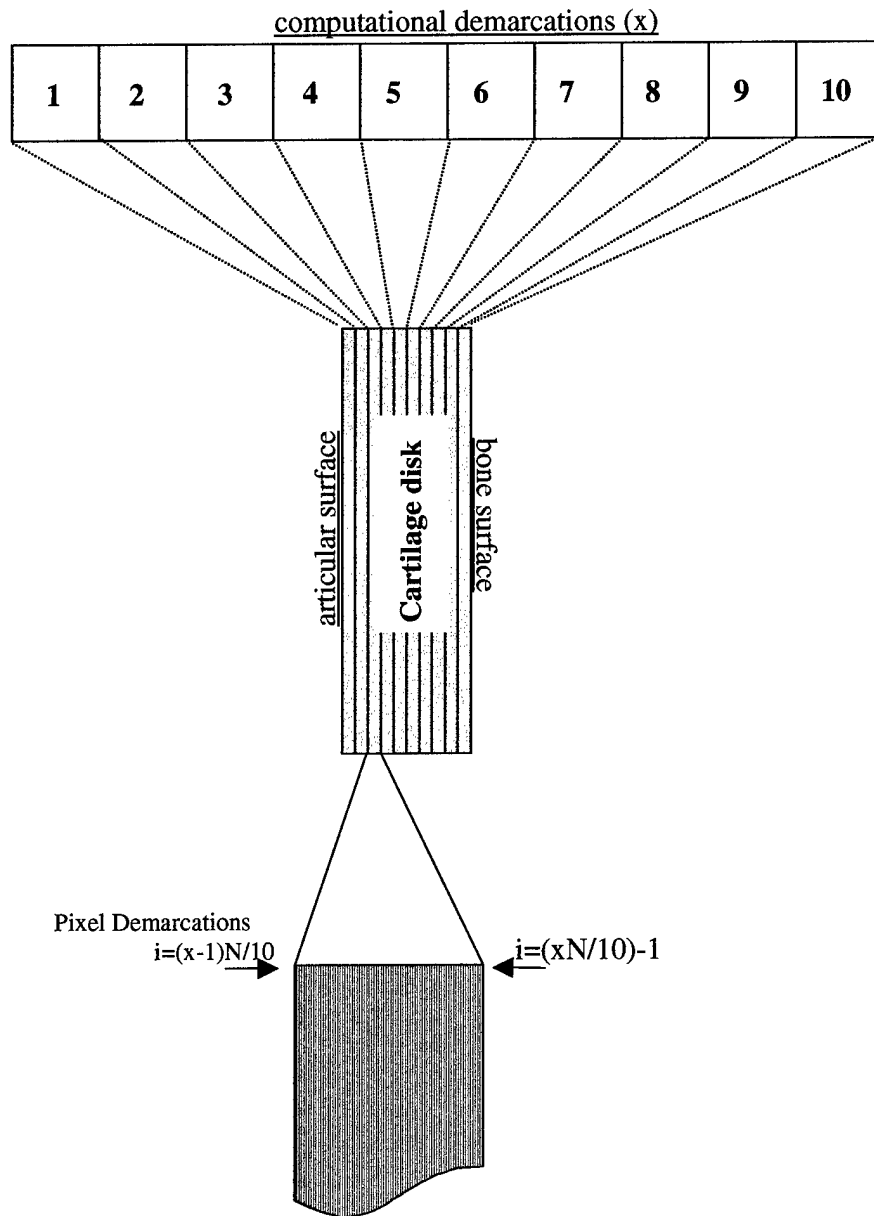


Figure B.15. Illustration of the computational demarcation scheme. The thickness of the cartilage specimen is divided into ten bins labeled $\{1,2,\dots,10\}$. The longitudinal pixel density is $N/10$ pixels per bin.

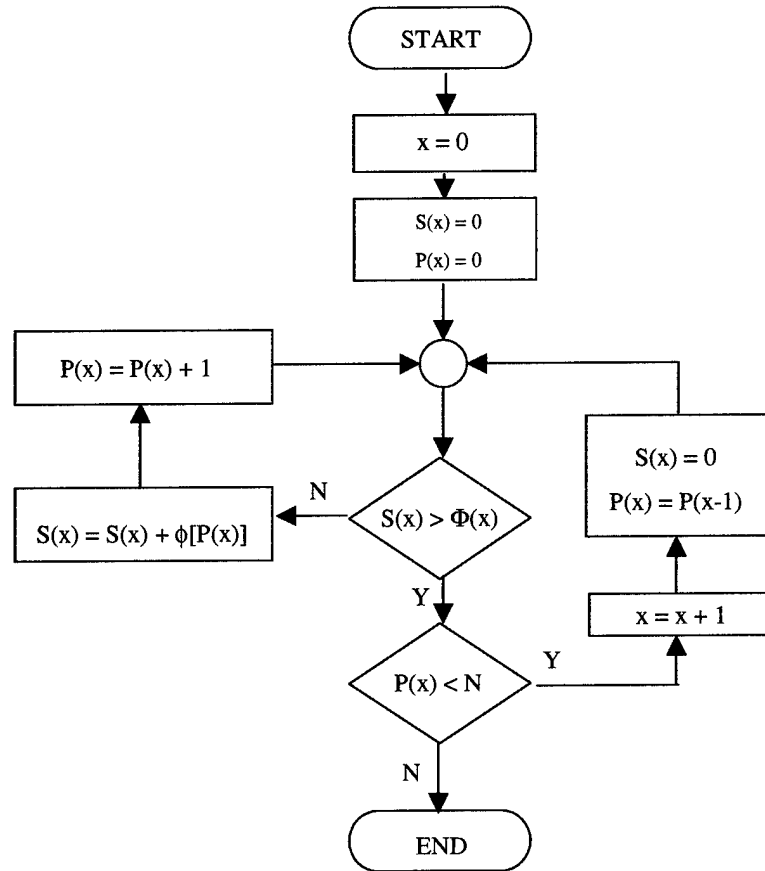


Figure B.16. Flow chart of the algorithm used to calculate the locations of the original computational demarcations at any given point in time. $P(x)$ is the pixel position of demarcation x . $S(x)$ is a temporary holding bin for comparing collected solid content to the original solid content demarcation array, $\Phi(x)$, introduced in equation B.10.

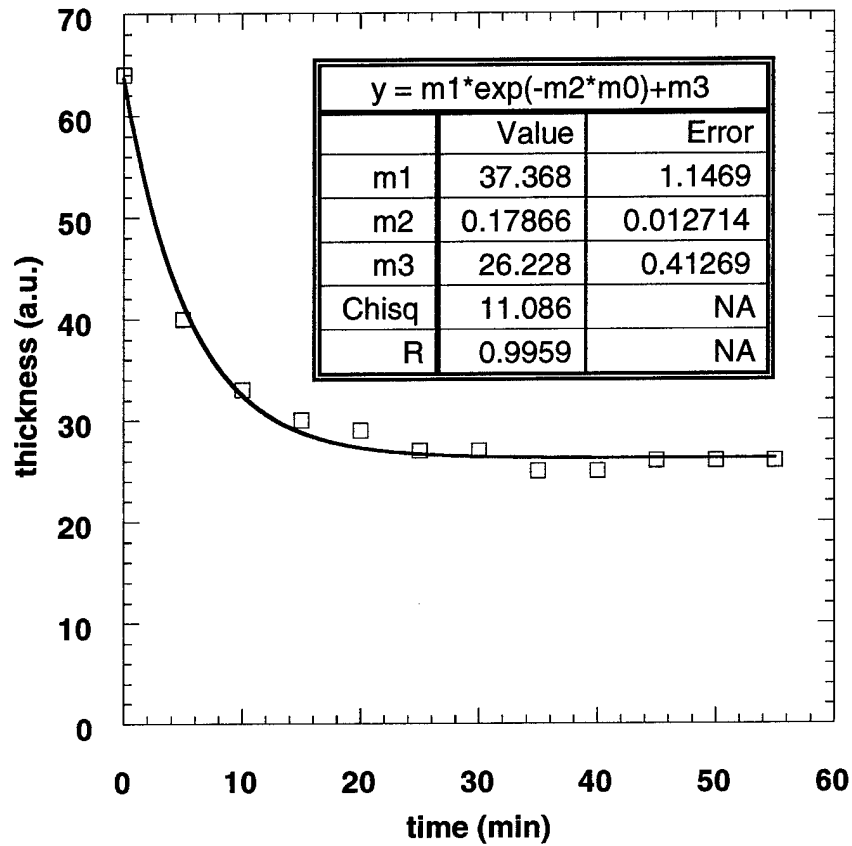


Figure B.17 Time dependant longitudinal strain of cartilage section. The longitudinal strain of a representative cartilage section ($x = 1$ as in figure B.10) is presented as a function of time under a constant compressive pressure of 0.69 MPa. This plot corresponds to $e_1(t)$ as defined in equation B.14. The solid line is a least squares best fit of the derived experimental results (represented as square) to equation B.15. The result of the best-fit algorithm is indicated in the figure. A similar analysis was conducted for all sections $x=\{1,...,10\}$, the results of which are displayed in figures B.18 and B.19.

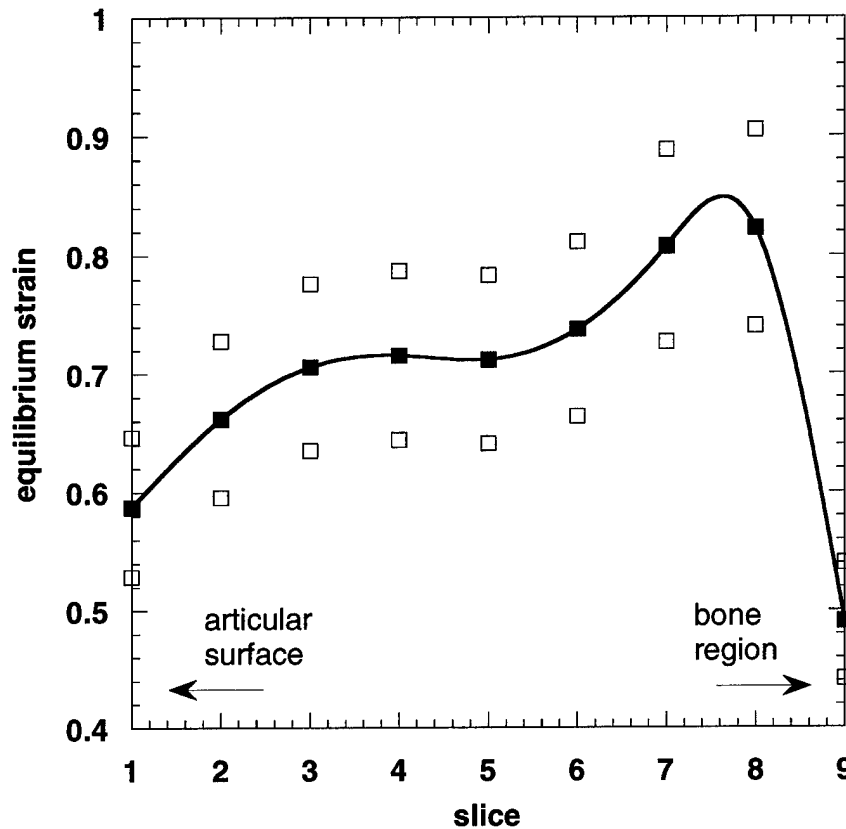


Figure B.18. Equilibrium strain of cartilage sections. Equilibrium compressive strain is plotted as a function of cartilage section as demarcated in figure B.15. The magnitude of strain is proportional to compressive modulus. The constant applied pressure is 0.69 MPa. The strain of each section was obtained as a best fit to equation B.15. Since strain is assumed to be a continuous function of cartilage space, the calculated points are connected by a cubic spline. Open squares indicate distribution of specimens.

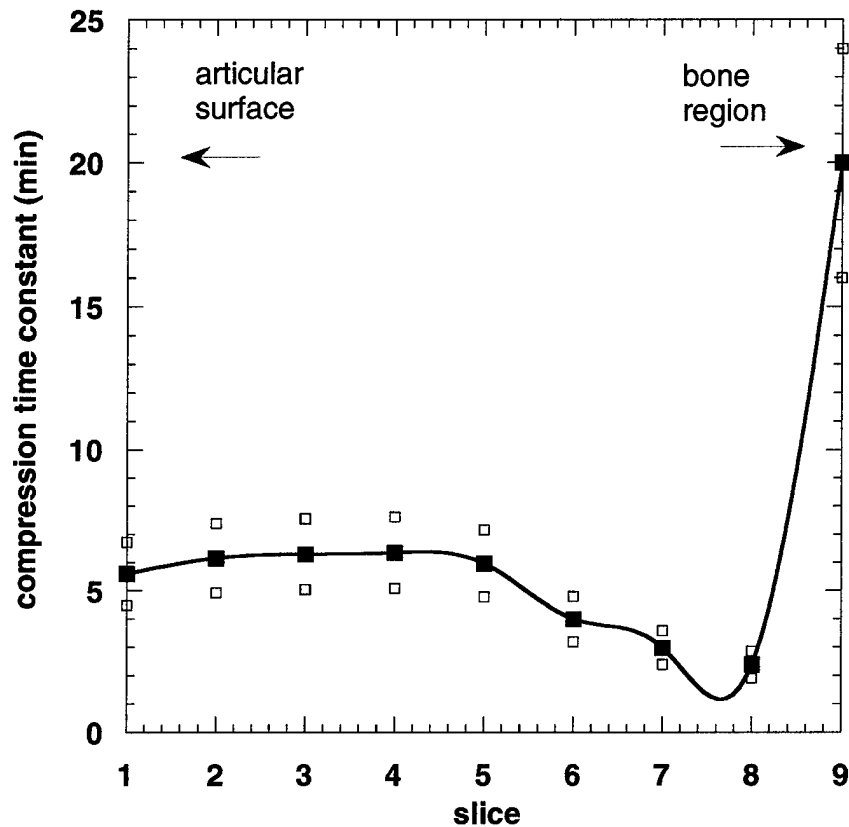


Figure B.19 Compression time constant of cartilage sections. Compression time constant is plotted as a function of cartilage section as demarcated in figure B.15. The constant applied pressure is 0.69 MPa. The time constant of each section was obtain as a best fit to equation B.15. Since compression time constant is assumed to be a continuous function of cartilage space, the calculated points are connected by a cubic spline. Open squares indicate distribution of specimens.

BIBLIOGRAPHY

1. Amendola A, Rorabeck CH, Bourne RB, and Apyan, PM, Total knee arthroplasty following high tibial osteotomy for osteoarthritis. *Journal of Arthroplasty*. 1989;4 (Supplement):S11-7.
2. Armstrong CG, Lai WM, Mow VC. An analysis of the unconfined compression of articular cartilage. *Journal of Biomechanical Engineering*. 1984, 106(2):165-73.
3. Athanasiou KA, Agarwal A, Dzida FJ, Comparative study of the intrinsic mechanical properties of the human acetabular and femoral head cartilage. *Journal of Orthopaedic Research*. 1994;12:340-9.
4. Basic G, Liu KJ, Fuminori G, Hoopes PJ, Rosen GM, Swartz SM. MRI contrast enhanced study of cartilage proteoglycan degradation in the rabbit knee. *Magnetic Resonance in Medicine*. 1997;37:764-768.
5. Bader DL, Kempson GE, The short-term compressive properties of adult human articular cartilage, *Bio-Medical Materials & Engineering* 1994; 4:245-56.
6. Bashir A, Gray ML, Boutin RD, Burstein D. Glycosaminoglycan in articular cartilage: in-vivo assessment with delayed Gd(DTPA)-enhanced MR imaging. *Radiology*. 1997;205:551-558.

7. Bashir A, Gray ML, Burstein D. Gd(DTPA) as a measure of cartilage degradation. *Magnetic Resonance in Medicine*. 1996;36:665-673.
8. Brandl M., Haase A., Molecular diffusion in NMR microscopy, *Journal of Magnetic Resonance, Series B* 1994; 103:162-167.
9. Buschmann MD, Grodzinsky AJ, A molecular model of proteoglycan-associated electrostatic forces in cartilage mechanics. *Journal of Biomechanical Engineering* 1995; 117:179-92.
10. Carr HY, and Purcell EM, Effects of diffusion on free precession in nuclear magnetic resonance experiments, *Physical Review* 1954; 94:630-635.
11. Davis GC, Cortez C, Rubin BR. Pain management in the older adult with rheumatoid arthritis or osteoarthritis. *Arthritis Care Res*. 1993; 3: 127- 31.
12. Donahue KM, Burstein D, Manning WJ, Gray ML, Studies of Gd-DTPA relaxivity and proton exchange rates in tissue, *Magnetic Resonance in Medicine*. 1994;32:66-76.
13. Donnan FG, The theory of membrane equilibria. *Chemical Review* 1924; 1:73-90.
14. Durham EJ, and Ryskiewich DP, The acid dissociation constants of diethylenetriaminepentaacetic acid and the stability constants of some of its metal chelates. *Journal of the American Chemical Society* 1958; 80:4812-7.

15. Duvvuri U, Reddy R, Patel SD, Kaufman JH, Kneeland JB, Leigh JS. T1rho-relaxation in articular cartilage: effects of enzymatic degradation. *Magnetic Resonance in Medicine*. 1997;38:863-7.
16. Duvvuri U, Kaufman JH, Patel SD, Bolinger L, Kneeland JB, Leigh JS, Reddy R, Sodium multiple quantum spectroscopy of articular cartilage: effects of mechanical compression. *Magnetic Resonance in Medicine*. 1998;40:370-5.
17. Eckstein F, Tieschky M, Faber SC. Effect of physical exercise on cartilage volume and thickness in-vivo: MR imaging study. *Radiology* 1998;207:243-8
18. Farndale RW, Sayers CA, Barret AJ. A direct spectrophotometric microassay for sulfated glycosaminoglycans in cartilage cultures. *Connective Tissue Research*. 1982;9:247-248.
19. Fermi EF. *Thermodynamics*. New York: Dover; 1936.
20. Frost AE, Polyaminopolycarboxylic acids derived from polyethyleneamines. *Nature* 1956; 178:322.
21. Fung YC, *The Foundations of Solid Mechanics*, Prentice Hall, NJ p.22 1965
22. Ghosh P, Brooks P. Chondroprotection- exploring the concept. *J Rheumatol*. 1991; 18: 161- 6.

23. Gu WY, Lai WM, Mow VC, Transport of fluid and ions through a porous-permeable charged-hydrated tissue, and streaming potential data on normal bovine articular cartilage. *Journal of Biomechanics* 1993; 26:709-23.
24. Hahn EL. Spin echoes. *Physical Review* 1950;80:580.
25. Hale JE, Rudert JM, Brown TD, Indentation assessment of biphasic mechanical property deficits in size-dependent osteochondral defect repair. *Journal of Biomechanics*. 1993;26:1319-25.
26. Hall AC, Horwitz ER, Wilkins RJ, The cellular physiology of articular cartilage. *Experimental Physiology* 1996; 81:535-45
27. Hamerman D, The biology of osteoarthritis. *New England Journal of Medicine* 1989; 320:1322-30.
28. Hardingham T, Bayliss M, Proteoglycans of articular cartilage: changes in aging and in joint disease, *Seminars in Arthritis and Rheumatism*. 1990;20(3, suppl. 1):12-33.
29. Haut RC, Ide TM, De Camp CE, Mechanical responses of the rabbit patello-femoral joint to blunt impact. *Journal of Biomechanical Engineering*. 1995;117:402-8.
30. Harris ED, Parker HG, Radin EL, Krane SM, Effects of proteolytic enzymes on structural and mechanical properties of cartilage. *Arthritis and Rheumatism* 1972;15:497-503.

31. Helfferich F. *Ion Exchange*. New York: Dover; 1962.
32. Hutton C W, Viennart W. Osteoarthritis and magnetic resonance imaging: potential and problems. *Ann Rheum Dis* 1995; 54: 237- 43.
33. Jan MH, Lai JS. The effects of physiotherapy on osteoarthritic knees of females. *J Formos Med Assoc*. 1993; 90: 1008- 13.
34. Jurvelin J, Kivarananta I, Saamanen AM, Tammi M, Helminen, Indentation stiffness of young canine knee articular cartilage - influence of strenuous joint loading. *Journal of Biomechanics*. 1990;23:1239-46.
35. Kaufman JH, Reddy R, Kneeland JB, Leigh JS, Mapping water migration in articular cartilage during compression in "Proceedings of the International Society of Magnetic Resonance in Medicine 1995 Annual Meeting" Nice, France.
36. Kaufman JH, Regatte RR, Bolinger L, Kneeland JB, Reddy R, Leigh JS, A novel approach to observing articular cartilage in vitro via magnetic resonance imaging. *Journal of Magnetic Resonance Imaging*. 1999;9:653-62.
37. Khalsa PS, Eisenberg SR, Compressive behavior of articular cartilage is not completely explained by proteoglycan osmotic pressure. *Journal of Biomechanics* 1997; 30:589-94.
38. Kovach IS, A molecular theory of cartilage viscoelasticity, *Biophysical Chemistry* 1996; 59:61-73.

39. Kovar PA, Allegrante JP, MacKenzie CR, Peterson MG, Gutin B, Charlson ME.
Supervised fitness walking in patients with osteoarthritis of the knee. A
randomized, controlled trial. *Ann Intern Med.* 1992; 116: 529- 34.
40. Lawrence RC, Hochberg MC, Kelsey JL, McDuffie FC, Medsger TA Jr, et al.
Estimates of the prevalence of selected arthritic and musculoskeletal diseases in
the United States. *J Rheumatol.* 1989; 16: 427- 41.
41. Lehner KB, Rechl HP, Gmeinwieser JK, Heuck AF, Lukas HP, Kohl HP,
Structure, function, and degeneration of bovine hyaline cartilage: assessment with
MR imaging in vitro. *Radiology* 1989; 170:495-9.
42. Lesperance LM, Gray ML, Burstein D. Determination of fixed charge density in
cartilage using nuclear magnetic resonance. *Journal of Orthopaedic Research.*
1992;10:1-13.
43. Lusse S, Knauss R, Werner A, Grunder W, Arnold K. Action of compression and
cations on the proton and deuterium relaxation in cartilage. *Magnetic Resonance
in Medicine* 1995;33:483-9.
44. Mak AF, The apparent viscoelastic behavior of articular cartilage - the
contributions from the intrinsic matrix viscoelasticity and interstitial fluid flows.
Journal of Biomechanical Engineering. 1986;108:123-30.

45. Mankin H, Mow V, Buckwalter J, Iannotti J, Ratcliffe J: Form and function of articular cartilage. In: *Orthopaedic Basic Science*. Ed: Simon S, American Academy of Orthopaedic Surgeons, Rosemont, IL. 1994.
46. Mansour JM, Mow VC, The permeability of articular cartilage under compressive strain and at high pressures. *The Journal of Bone and Joint Surgery* 1976; 58A:505-16.
47. March, L. M.; Brooks, P. M. Clinical trials in osteoarthritis. *Annals of the Rheumatic Diseases*. 1996; 55(8):491-3.
48. Maroudas A, Bayliss MT, Uchitel-Kaushansky N, Schneiderman R, Aggreacan turnover in human articular cartilage: use of aspartic acid racemization as a marker of molecular age. *Archives of Biochemistry & Biophysics* 1998; 350:61-71.
49. Maroudas A, Evans H. A study of ionic equilibria in cartilage. *Connective Tissue Research*. 1972;1:69-77.
50. Maroudas A. Muir H. Wingham J. The correlation of fixed negative charge with glycosaminoglycan content of human articular cartilage. *Biochimica et Biophysica Acta*. 177(3): 492- 500, 1969.
51. Maroudas A, Transport of solutes through cartilage: permeability to large molecules. *Journal of Anatomy* 1976; 122(2):335-47.

52. Maroudas A. Physicochemical properties of articular cartilage in the light of ion exchange theory. *Biophysical Journal*. 1968;8:575-595.
53. McCutchen CW, Cartilage is poroelastic, not viscoelastic (including an exact theorem about strain energy and viscous loss, and an order of magnitude relation for equilibration time), *Journal of Biomechanics* 1982; 15:325-7, 1982.
54. McCutchin CW, The frictional properties of animal joints. *Wear* 1972; 5:1-17.
55. Mow VC, Holmes MH, Lai WM, Fluid transport and mechanical properties of articular cartilage: a review, *Journal of Biomechanics* 1984; 17:377-94.
56. Mow VC, Gibbs MC, Lai WM, Zhu WB, Athanasiou KA, Biphasic indentation of articular cartilage - II. a numerical algorithm and an experimental study. *Journal of Biomechanics* 1989;22:853-61.
57. Mow VC, Hou JS, Owens JM, Ratcliffe A, Biphasic and quasilinear viscoelastic theories for hydrated soft tissues. In: Mow VC, Ratcliffe A, Woo SL, eds. *Biomechanics of Diarthrodial Joints Volume One*. New York: Springer Verlag, 1990;
58. Mow VC, Kuei SC, Armstrong CG, Biphasic creep and stress relaxation of articular cartilage in compression: theory and experiments. *Journal of Biomechanical Engineering* 1980; 102:73-84.

59. Neeman M., Freyer J.P., Sillerud L.O., Pulsed-gradient spin-echo diffusion studies in NMR imaging. Effects of the imaging gradients on the determination of diffusion coefficients, *Journal of Magnetic Resonance* 1990; 90,:303-312.
60. Obeid EMH, Adams MA, Newman JH, Mechanical properties of articular cartilage in knees with unicompartmental osteoarthritis. *Journal of Bone and Joint Surgery (British)*. 1994;76-B:315-9.
61. Oloyede A, Flachsmann R, Broom N, The dramatic influence of loading vlocity of the compressive response of articular cartilage, *Connective Tissue Research*. 1992; 27,211-24.
62. Parsons JR, Black J, The viscolastic shear behavior of normal rabbit articular cartilage. *Journal of Biomechanics*. 1977;10:21-9.
63. Paul PK, Jasani MK, Sebok D, Rakhit A, Dunton AW, Douglas FL, Variation in MR signal intensity across normal human knee cartilage. *Journal of Magnetic Resonance Imaging* 1993; 3:569-74.
64. Platt D, Bird JL, Bayliss MT, Ageing of equine articular cartilage: structure and composition of aggrecan and decorin. *Equine Veterinary Journal* 1998; 30:43-52.
65. Recht MP, Resnick D, MR imaging of articular cartilage: current status and future directions. *American Journal of Roentgenology* 1994; 103:283-90.

66. Reddy R, Insko EK, Noyszewski EA, Dandora R, Kneeland JB, Leigh JS. Sodium MRI of human articular cartilage in vivo. *Magnetic Resonance in Medicine*. 1998;39:697-701.
67. Reddy R, Kaufman JH, Insko EK, Kneeland JB, Leigh JS. Sodium spectroscopy of articular cartilage during compression. In: *Proceedings of the ISMRM 4th Annual Meeting*, New York, 1996. p 1097.
68. Rubenstein JD, Kim JK, Henkelman RM, Effects of compression and recovery on bovine articular cartilage: appearance on MR images. *Radiology* 1996; 201:843-50.
69. Schinagl RM, Ting MK, Price JH, Sah RL. Video microscopy to quantitate the inhomogeneous equilibrium strain within articular cartilage during confined compression. *Annals of Biomedical Engineering* 1996; 24(4):500-12.
70. Schnall MD, Subramanian VH, Leigh JS, Chance B. A new double-tuned probe for concurrent H1 and P31 NMR. *Journal of Magnetic Resonance* 1985;65:122-9.
71. Schwartz MH, Leo PH, Lewis JL, A microstructural model for the elastic response of articular cartilage. *Journal of Biomechanics* 1994; 27:865-73.
72. Setton LA, Mow VC, Muller FJ, Pita JC, Howell DS, Mechanical properties of canine articular cartilage are significantly altered following transection of the anterior cruciate ligament. *Journal of Orthopaedic Research* 1994; 12:451-63.

73. Shapiro EM, Borthakur A, Dandora R, Kriss A, Leigh JS, Reddy R. Sodium Visibility and Quantitation in Intact Bovine Articular Cartilage Using High Field ^{23}Na MRI and MRS. *Journal of Magnetic Resonance*. 2000;12:24-31.
74. Spilker RL, Suh JK, Mow VC. Effects of friction on the unconfined compressive response of articular cartilage: a finite element analysis. *Journal of Biomechanical Engineering* 1990 112(2):138-46.
75. Spirt AA, Mak AF, Wassell RP, Nonlinear viscoelastic properties of articular cartilage in shear. *Journal of Orthopaedic Research*. 1989;7:43-8.
76. Suh JK, Zhengfang L, Woo S, Dynamic behavior of a biphasic cartilage model under cyclic compressive loading. *Journal of Biomechanics*. 1995;28:357-64.
77. Suh JK, Dynamic unconfined compression of articular cartilage under a cyclic compressive load. *Biorheology* 1996;33:289-304.
78. Todd PA, Clissold SP. Naproxen. A reappraisal of its pharmacology and therapeutic use in rheumatic diseases and pain states. *Drugs*. 1990; 40: 91- 137.
79. Torzilli PA, Dethmers DA, Rose DE, Movement of interstitial water through loaded articular cartilage. *Journal of Biomechanics*. 1983;16:169-79.
80. Torzilli PA , Water content and equilibrium water partition in immature cartilage. *Journal of Orthopaedic Research* 1988; 6:766-9.

81. Trattnig S, Mlynarik V, Breitenseher M, Huber M, Zembsh A, Rand T, and Imhof H. MRI visualization of proteoglycan depletion in articular cartilage via intravenous administration of Gd(DTPA). *Magnetic Resonance Imaging*. 1999;17:577-583.
82. Wei L, Svensson O, Hjerpe A, Correlation of morphologic and biochemical changes in the natural history of spontaneous osteoarthritis in guinea pigs. *Arthritis & Rheumatism* 1997; 40:2075-83.
83. Werner A, Grunder W, Calcium-induced structural changes of cartilage proteoglycans studied by ^1H NMR relaxometry and diffusion measurements. *Magnetic Resonance in Medicine* 1999;41:43-50.
84. Xia Y, Relaxation anisotropy in cartilage by NMR microscopy (μMRI) at $14\mu\text{M}$ Resolution, *Magnetic Resonance in Medicine* 1998; 39: 941-9.
85. Zahler MDP *Analysis of nonlinear viscoelastic deformation of biological tissue* (Ph.D. dissertation, Department of Mathematics, Rensselaer Polytechnic Institute) 1999.
86. Zhu W, Mow VC, Koob TJ, Eyre DR, Viscoelastic shear properties of articular cartilage and the effects of glycosidase treatments. *Journal of Orthopaedic Research*. 1993;11:771-81.